Characterizing the Structural and Physiological Effects of IMPDH2 Mutations Associated with Neurodevelopmental Disorders

Audrey O’Neill

A dissertation
submitted in partial fulfillment of the
requirements for the degree of

Doctor of Philosophy

University of Washington
2025

Reading Committee:
Justin M. Kollman, Chair
Susan E. Brockerhoff
Chip Asbury

Program Authorized to Offer Degree:
Biochemistry

University of Washington

Abstract

Characterizing the Structural and Physiological Effects of IMPDH2 Mutations Associated with Neurodevelopmental Disorders

Audrey O’Neill

Chair of the Supervisory Committee:
Justin M. Kollman
Department of Biochemistry

Inosine-5’-monophosphate dehydrogenase (IMPDH) catalyzes the first committed step of *de novo* guanine nucleotide biosynthesis, converting IMP to XMP. To control this important metabolic branch point between adenine and guanine nucleotide synthesis, IMPDH is highly regulated, including through assembly into filaments. There are two isoforms of IMPDH in humans, but IMPDH2 is specifically essential for development and is upregulated during proliferation. Mutations in IMPDH2 have been identified in patients with neurodevelopmental disorders exhibiting a range of neurological symptoms, including dystonia. Here, we show with *in vitro* enzyme assays, negative stain electron microscopy, and high-resolution structures determined by cryo-EM, how each mutation affects the structure, activity, and allosteric regulation of IMPDH2 filaments and octamers. We also develop *Xenopus tropicalis* as a model to study the effects of one variant, the in-frame deletion of serine 160, on metabolism, neuromuscular development, and IMPDH filament formation in a vertebrate system. This work establishes a model for studying the mechanisms of disease that arise from IMPDH2 dysregulation.

Acknowledgements

First and foremost, I would like to acknowledge the patients who presented with the IMPDH2 variants characterized here. It is my most sincere hope that these results will be useful in future efforts developing therapies for these patients. And thank you to our collaborators for reaching out to share new cases of IMPDH2 mutation with us, especially Dr. Michael Zech, Dr. Orly Elpeleg, Alyssa Rippert, Dr. Jorge Granadillo, Dr. Rami Abou Jamra, Dr. Angela Peron, and Dr. Evgenia Sklirou.

I next want to thank my advisor, Dr. Justin Kollman, for allowing me to study what genuinely fascinated me about this endlessly complicated and frustrating enzyme. I would also like to thank Dr. Andrea Wills for the additional guidance and new perspectives during my thesis work.

I have so many great scientists to thank for their support along the way. Thank you to my first advisor, Dr. Dali Liu, for introducing me to structural biology and for being a huge source of encouragement for me since my first year in college. Thank you to my good friend Dr. Elana Baltrusaitis for mentoring me back when we were undergrads. Thank you to Dr. Anika Burrell for introducing me to IMPDH and mentoring me as a rotation student. Thank you to my mentee and friend, Gardenia Sanchez-Ramirez, for really engaging with this work and for teaching me how to be a better mentor every day. Thank you to my labmates and friends–especially Dr. John Calise for sharing a bay with me and for setting an example for me as a scientist, Dr. Daniel Asarnow, Dr. Sasha Dickinson, and Joel Quispe for answering my naive questions about EM, Dr. Kelli Hvorecny and Dr. Eric Lynch for being scientists and people that I look up to, Dr. Lauren Salay and Jojo Molfino for your friendship and positivity, and Dr. Jeet Patel, Morgan McCartney, and Gavin Wheeler for teaching me about your cool frogs and for your contributions to the experiments in Chapter 4, specifically microinjections, immunostaining, and light microscopy. And thank you to the team at the Northwest Metabolomics Research Center for running our samples.

Outside of science, I want to thank my beautiful ballet friends, especially Laura and Renzo, for dancing with me when I needed to work the other side of my brain. Thank you to the PAWS Wildlife Center for giving me an outlet to give back to my community. I would also like to acknowledge friends who kept me grounded, especially Bel, Joey, Caroline, Maggi, Mary Grace, and Roz.

Lastly, and most importantly, I'd like to thank my partner Nathaniel for your constant support throughout. Absolutely none of this would have been possible without you.

Dedication

For my Babcia.

Table of Contents

List of Figures

List of Tables

Chapter 1. Introduction

Adapted from:

O’Neill, A. G., Burrell, A. L., Zech, M., Elpeleg, O., Harel, T., Edvardson, S., ... & Kollman, J. M. (2023). Neurodevelopmental disorder mutations in the purine biosynthetic enzyme IMPDH2 disrupt its allosteric regulation. Journal of Biological Chemistry, 299(8).

O’Neill, A. G., McCartney, M. E., Wheeler, G. M., Patel, J. H., Sanchez-Ramirez, G., Kollman, J. M., & Wills, A. E. (2025). An IMPDH2 variant associated with neurodevelopmental disorder disrupts purine biosynthesis and somitogenesis. bioRxiv, 2025-05.

1.1 Overview of purine nucleotide biosynthesis.

Purine nucleotides are essential components of cells, where they serve as signaling molecules, energy sources, and precursors of RNA and DNA. Their synthesis begins with the ribose 5-phosphate produced from the pentose phosphate pathway, which is converted to phosphoribosyl pyrophosphate (PRPP) by the conserved enzyme phosphoribosyl pyrophosphate synthetase (PRPS). PRPP can then feed into two possible pathways to make purine nucleotides–the *de novo* pathway, or the salvage pathway. The *de novo* pathway converts PRPP to inosine 5’-monophosphate (IMP) in ten enzyme-catalyzed steps. This IMP can then be committed to the synthesis of guanine nucleotides by the enzyme IMP dehydrogenase (IMPDH), or it can be used by the enzyme adenylosuccinate synthetase (ADSS) to generate adenylosuccinate (S-AMP) in the first committed step to make adenine nucleotides. Alternatively, PRPP can feed into the salvage pathway to make purine nucleotides from the existing precursors guanine, adenine, or hypoxanthine. The enzyme hypoxanthine-guanine phosphoribosyltransferase (HPRT) transfers the phosphoribosyl group from PRPP to either hypoxanthine or guanine to make IMP or GMP, respectively. The enzyme adenine phosphoribosyltransferase (APRT) catalyzes the same type of reaction, transferring the phosphoribosyl group of PRPP to adenine to make AMP. The salvage pathway is utilized alongside the *de novo* synthesis pathway to maintain purine pools during steady state, but during cell proliferation, *de novo* biosynthesis is specifically upregulated to meet the increased demand for purine nucleotides (1, 2).

1.2 IMP dehydrogenase in growth and development.

IMPDH catalyzes the rate-limiting step of *de novo* guanine nucleotide biosynthesis–the conversion of inosine 5’-monophosphate (IMP) to xanthosine 5’-monophosphate (XMP) (3, 4). IMP is also a precursor in the *de novo* synthesis of adenine nucleotides, IMPDH sits at a key metabolic branchpoint that controls flux between adenine and guanine nucleotide production (5–7).

There are two human isoforms of IMPDH with 84% sequence identity (8). IMPDH1 is constitutively expressed in most tissues at low levels, while expression levels of

IMPDH2 are generally higher and specifically elevated in proliferative states and developing tissues (9–12). While IMPDH1 expression is higher than IMPDH2 in the developed retina, IMPDH2 is predominantly expressed in early retinal development (11, 13). IMPDH2 expression is also selectively enhanced in cancer, such as in human brain tumors, sarcoma cells, and leukemic cells, making it an appealing cancer target (10, 14–16).

There are few studies on IMPDH2 in the development of vertebrates, though its expression is critical for embryonic development. The deletion of IMPDH2, but not IMPDH1, is embryonic lethal in mice (17). IMPDH2 expression in the neural crest is required for proper development of the enteric nervous system and other derivatives of the neural crest such as the craniofacial skeleton (18). In the central nervous system, reliance on the *de novo* purine biosynthetic pathway is higher in embryonic stages than postnatal adult mice, with early embryonic neocortical development being especially reliant on the *de novo* pathway and impaired by the inhibition of IMPDH (19). In zebrafish embryos, inhibition of IMPDH impairs angiogenesis and the sprouting of intersegmental blood vessels between somites, where IMPDH2 is the predominant isoform (20). Tight control of purine pools is therefore essential for development and cellular homeostasis, requiring precise regulation of IMPDH2 activity.

1.3 Structure and mechanism of IMPDH allosteric regulation.

To control the branch point of adenine and guanine nucleotide biosynthesis, IMPDH is precisely regulated at multiple levels including through allosteric regulation by purine nucleotide binding and reversible assembly into filaments (21–27). One IMPDH protomer is composed of a catalytic domain and a regulatory Bateman domain (Fig. 1.1A). Both domains are involved in the oligomerization that is key to the enzyme’s catalytic activity and regulation. IMPDH constitutively assembles tetramers through catalytic domain interactions (Fig. 1.1A), and tetramers reversibly dimerize into octamers through interactions of the Bateman domains in response to binding of adenine or guanine nucleotides to three allosteric sites (Fig. 1.1B). Binding of ATP in sites 1 and 2 promotes Bateman domain interactions in an extended, active conformation. Binding of GTP in sites 2 and 3 promotes similar Bateman domain interactions but stabilizes different interdomain contacts within each monomer that result in a compressed, inactive conformation. According to the current model of IMPDH inhibition, GTP-induced compression of canonical octamers forces the interaction of opposing finger domains. This finger domain interaction inhibits enzyme function by impeding the dynamics of the active site during the catalytic cycle (12, 21, 24, 28). In *Mycobacterium smegmatis* IMPDH, compression of the octamer induced by GTP binding causes the finger domain and catalytic flap to adopt a conformation which prevents IMP binding (29). While GTP acts as an allosteric inhibitor by controlling transition from extended to compressed conformations (21, 30), IMPDH2 specifically is further regulated by assembly of octamers into filaments of stacked octamers (Fig. 1.1C), which have the effect of reducing affinity for GTP by disfavoring the compressed conformation (25, 26, 30).

1.4 IMPDH filaments.

Assembly of enzymes into filaments is a commonly observed mechanism that cells leverage to regulate metabolic processes (26, 27, 31–35). Both isoforms of human IMPDH assemble into filaments, but for IMPDH2 specifically, incorporation into filaments reduces sensitivity of the enzyme to GTP inhibition by preventing complete compression of the octamer (26, 27). These filaments are physiologically relevant, as supramolecular assemblies (referred to as "rods and rings" or "cytoophidia") of IMPDH have been observed *in vivo* and assemble under conditions of high demand for guanine nucleotides (13, 36–40). These assemblies are not observed in cells when the filament assembly interface is disrupted, supporting the hypothesis that they are composed of filaments (25). Of note, IMPDH rods have been observed in the nuclei of human gliomas, suggesting IMPDH filaments play a functional role in the nervous system (41). IMPDH2 punctae have also been observed at the branching sites and distal ends of astrocyte stem processes in mouse hippocampus tissue and primary cultures of astrocytes from the cerebral cortex, suggesting that subcellular localization of IMPDH2 could be involved in astrocyte branching (42). Immunogold labeling of fixed tissue sections suggests that IMPDH supramolecular assemblies are made up of shorter filaments that laterally interact to form bundles (41, 43). Bundles of IMPDH filaments have been reconstituted *in vitro* and are catalytically active (30).

1.5 IMPDH2 mutation in disease.

Mutations in *IMPDH2* have been identified in several unrelated patients with developmental disorders. Five *de novo* missense mutations (G113E, G113R, G207R [x2], Q243H) and one *de novo* in-frame deletion (S160del) in *IMPDH2* were previously identified in heterozygous patients with early-onset neurodevelopmental disorders and variably expressed dystonia, a neurological movement disorder characterized by involuntary muscle contractions which often presents comorbid with other neurological disorders (44). Since then, two more *de novo* missense mutations (L245P, K238R) were later discovered and published (45), and an additional five were most recently identified by clinicians–N198S (Dr. Jorge Granadillo, Washington University School of Medicine, personal communication), K229del and K205E (Dr. Rami Abou Jamra, University Hospital Leipzig, personal communication), R341Q (Dr. Evgenia Sklirou, UPMC Children's Hospital of Pittsburgh, personal communication), F114V (Dr. Angela Peron, Meyer Children's Hospital Florence, personal communication)–and are described further in our study. The symptoms of these patients vary widely, but commonly include hypotonia, developmental delay, intellectual disability, abnormal posturing, hyperkinetic movements, seizure activity, and speech disorders (Table 1.1). Interestingly, all but one of these mutations are located either in the regulatory domain or near the hinge region that connects the regulatory and catalytic domains (Fig. 1.2). A series of similar mutations in IMPDH1 have been associated with retinal degeneration (46–50), and a subset of these were shown to disrupt GTP feedback inhibition, classifying them as gain-of-function mutants (27, 30). We hypothesized that mutations in or around the regulatory domain of IMPDH2 would affect GTP inhibition in a similar manner. Prior to our work described here, it was unknown whether these mutations to IMPDH2 would affect its allosteric regulation, as hypothesized, or to what extent they might alter structural elements of the protein and its oligomeric assembly.

Though not investigated in our study, other rare variants of *IMPDH2* continue to be discovered, including two co-segregating variants recently linked to adult-onset isolated dystonia in a cohort of Chinese patients (51). Additionally, a heterozygous early termination in exon 1 of *IMPDH2,* classified as loss-of-function, was identified in an adult with later-onset dystonia and determined to be co-segregating with dystonia-tremor disease in a Finnish family (52), suggesting that both gain-of-function and loss-of-function mutations in *IMPDH2* may result in dystonic symptoms with varying disease onset and severity.

Before our present study, it was also unknown how expression of IMPDH2 variants in a model organism would affect vertebrate development. Dysregulation of IMPDH2 activity in the nervous system would likely disrupt the purine pools that are essential for nervous system function. While purines are utilized in all cells for essential biochemical processes, the maintenance of purine pools is particularly important in the nervous system, where purine-based nucleotides and nucleosides have additional functions as second messengers, neurotransmitters, neuromodulators, and trophic agents (53). To maintain the purine nucleotide and nucleoside pools required for these functions, either the salvage pathway or the *de novo* pathway can be used. In the salvage pathway of purine nucleotide synthesis, hypoxanthine-guanine phosphoribosyltransferase (HPRT) uses PRPP as a substrate to convert hypoxanthine to IMP or guanine to GMP. In the body, HPRT activity is highest in developed brain tissue, suggesting that the brain relies heavily on HPRT-dependent salvage pathways over *de novo* biosynthetic pathways (54). Deficiency of HPRT activity due to mutation results in accumulation of PRPP and increased activity in the *de novo* pathway, causing a neurodevelopmental disorder called Lesch-Nyhan syndrome (55–58). The phenotype of this syndrome, including variably expressed generalized dystonia, motor disability, and cognitive disability, partially overlaps with phenotypes in cases of IMPDH2 variants (44), suggesting that increased activity in the *de novo* purine biosynthetic pathway and subsequent perturbation of purine pools may lead to neurodevelopmental phenotypes.

Figure 1.1: IMPDH oligomeric assembly.

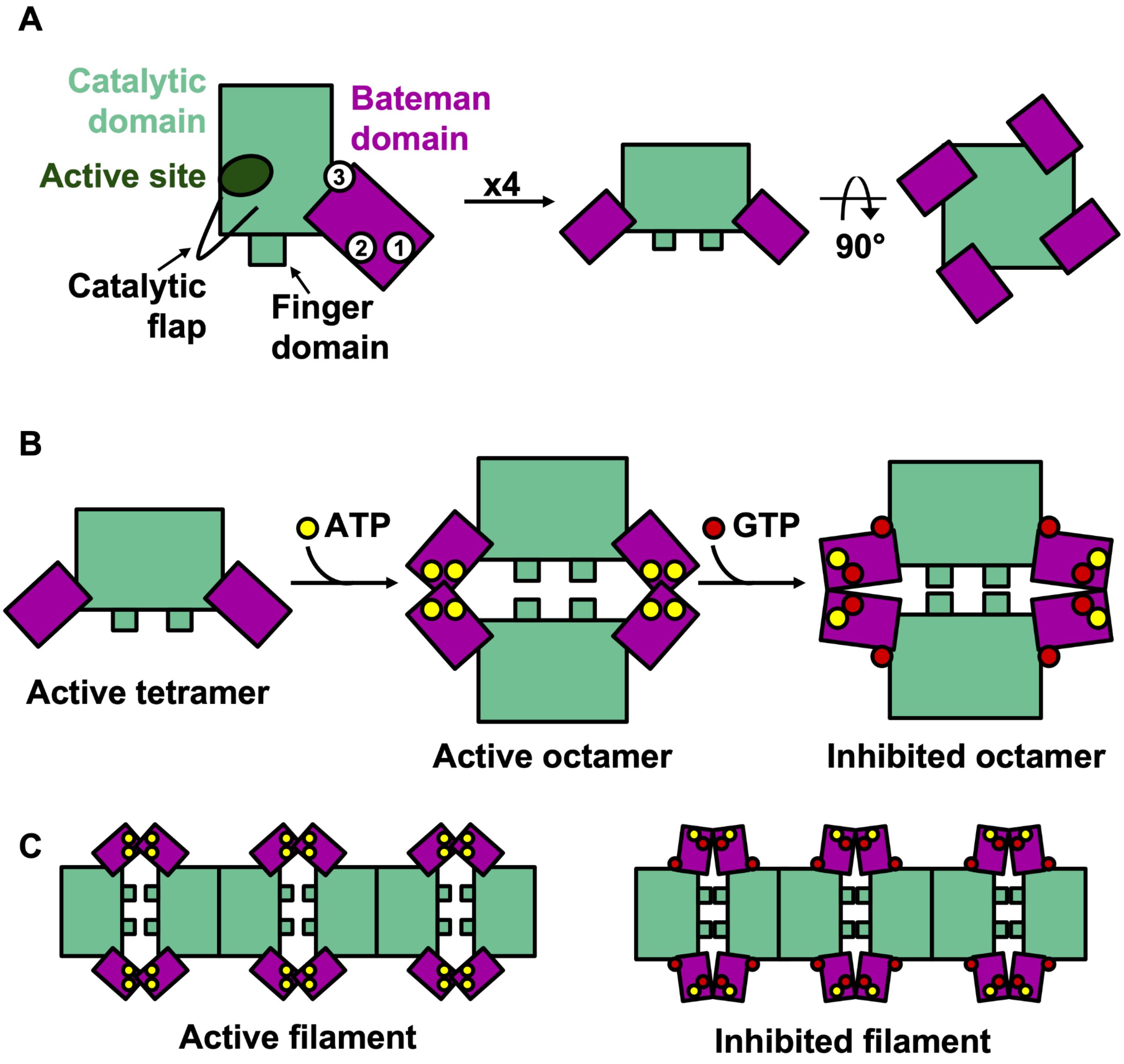

A. A cartoon representation of an IMPDH protomer, with notable regions labeled. Protomers assemble into tetramers through catalytic domain interactions (green).

B. ATP (or ADP) can bind allosteric sites 1 and 2 to stabilize extended octamers. GTP (or GDP) can bind allosteric sites 2 and 3 to stabilize compressed octamers, bringing finger domains of opposing tetramers together.

C. Extended and compressed octamers can both form filaments.

Figure 1.2: Mutation sites mapped to IMPDH2 structure.

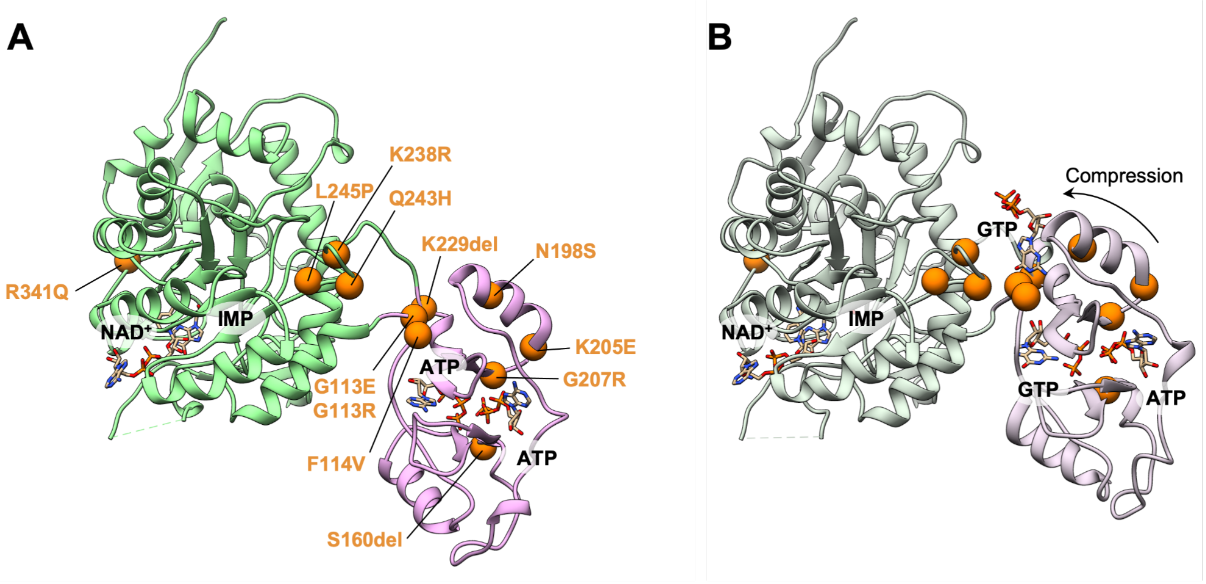

A. The model of one protomer from the previously published extended WT hIMPDH2 filament structure (PDB: 6U8N). The alpha-carbon at each patient mutation site is displayed as an orange sphere. The catalytic domain is colored in green, and the Bateman domain is colored in pink.

B. The structure of one protomer from the previously published compressed WT hIMPDH2 filament structure (PDB: 6U9O).

Table 1.1: Genotypes and patient phenotypes of the IMPDH2 variants investigated here.

Source	cDNA Variant	Protein Mutation	Zygosity	Variant inheritance	Dystonia/ Abnormal posturing	DD/ Hypotonia	ID	Speech	Seizure Activity	Other
Zech et al. (44)	c.338G>A	**p.Gly113Glu (G113E)**	Heterozygous	de novo	YES (generalized)	YES	YES	IMPAIRED	–	Gait instability
Zech et al. (44)	c.337G>A	**p.Gly113Arg (G113R)**	Heterozygous	de novo	NO	YES	YES	IMPAIRED	NO	Gait instability, Sleep disturbances, Autism
Zech et al. (44)	c.619G>C	**p.Gly207Arg (G207R)**	Heterozygous	de novo	–	YES	YES	IMPAIRED	YES	Gait instability, Dysmorphic facial features, Rectal prolapse
Zech et al. (44)	c.619G>A	**p.Gly207Arg (G207R)**	Heterozygous	de novo	–	YES	YES	IMPAIRED	YES	Cortical heterotopia
Zech et al. (44)	c.729G>C	**p.Gln243His (Q243H)**	Heterozygous	de novo	–	YES	YES	IMPAIRED	YES	Infant apnea, Gait instability, Ptosis, Rectal prolapse, Hypothyroidism, Polymicrogyria
Zech et al. (44)	c.478_480del	**p.Ser160del (S160del)**	Heterozygous	de novo	YES (focal limb)	YES	YES	IMPAIRED	–	Gait instability, Auditory hypersensitivity, Autism, Astigmatism, Cryptorchidism, Dysmorphic facial features, Cleft of the mitral valve, Isolated cerebral varix
O'Neill et al. (45)	c.734T>C	**p.Leu245Pro (L245P)**	Heterozygous	de novo	YES (cervical)	YES	YES	IMPAIRED	–	Motor delay, Pulmonic stenosis, Congenital dysplasia of the hip, Atrial septal defect, Mild dilation of left ventricle, Bilateral type B tympanograms, Dysmorphic facial features, Sparse/thin hair, Systolic murmur
O'Neill et al. (45)	c.713A>G	**p.Lys238Arg (K238R)**	Heterozygous	de novo	YES (cervical dystonia and abnormal limb/trunk posturing)	YES	–	DELAYED	–	Motor delay, Autism, Plagiocephaly, Improvement of some symptoms with L-DOPA treatment
This work	c.593A>G	**p.Asn198Ser (N198S)**	Heterozygous	de novo	–	YES	–	–	–	Cortical visual impairment, Diffuse atrophy of the brain parenchyma

A dashed line (-) indicates that the phenotype was not mentioned in the clinical summary of the patient.

DD: Developmental disorder

ID: Intellectual disorder

(Table 1.1 continued)

Source	cDNA Variant	Protein Mutation	Zygosity	Variant inheritance	Dystonia/ Abnormal posturing	DD/ Hypotonia	ID	Speech	Seizures	Other
This work	c.687_689del	**p.Lys229del (K229del)**	Heterozygous	de novo	–	–	–	–	–	Microcephaly, Webbed neck, Cutis laxa, Dandy-Walker malformation, Joint laxity, Intrauterine growth retardation, Premature birth, Ventricular septal defect, Dextrocardia, Hypoplasia of the corpus callosum, Scoliosis, Reduced subcutaneous adipose tissue, Persistent patent ductus venosus, Abnormality of the scalp hair, Palpebral edema, Long fingers
This work	c.613A>G	**p.Lys205Glu (K205E)**	Heterozygous	de novo	–	YES	–	IMPAIRED	–	Small hands, Small feet
This work	c.1022G>A	**p.Arg341Gln (R341Q)**	Heterozygous	UNKNOWN	–	–	YES	–	YES	Autism, Macrocephaly
This work	c.340T>G	**p.Phe114Val (F114V)**	Heterozygous	de novo	–	YES	–	–	–	Pulmonic stenosis, Dysmorphic facial features

A dashed line (-) indicates that the phenotype was not mentioned in the clinical summary of the patient.
DD: Developmental disorder
ID: Intellectual disorder

Chapter 2. *In vitro* characterization of IMPDH2 mutants

Adapted from:

O'Neill, A. G., Burrell, A. L., Zech, M., Elpeleg, O., Harel, T., Edvardson, S., ... & Kollman, J. M. (2023). Neurodevelopmental disorder mutations in the purine biosynthetic enzyme IMPDH2 disrupt its allosteric regulation. Journal of Biological Chemistry, 299(8).

O'Neill, A. G., McCartney, M. E., Wheeler, G. M., Patel, J. H., Sanchez-Ramirez, G., Kollman, J. M., & Wills, A. E. (2025). An IMPDH2 variant associated with neurodevelopmental disorder disrupts purine biosynthesis and somitogenesis. bioRxiv, 2025-05.

2.1 IMPDH2 mutations disrupt GTP inhibition.

To determine whether disease-associated IMPDH2 mutations have a direct effect on enzyme activity or regulation, we assayed purified recombinant enzymes *in vitro*. For all but one variant, we observed modest variation in the apparent V_{max} of the enzymes and $K_{0.5}$ values for IMP and NAD+ relative to WT enzyme, suggesting that basal activity is not severely affected by these mutations (Table 2.1). Interestingly, for the R341Q variant, the $K_{0.5}$ for IMP was almost one order of magnitude higher, and the $K_{0.5}$ for NAD+ was doubled, with both Hill coefficients at 1, indicating that cooperativity is abolished by this mutation (Table 2.1).

We next tested whether the disease mutations affect GTP inhibition. WT IMPDH2 filaments are inhibited by GTP with an IC50 of 577 µM under our assay conditions (Fig. 2.1); as previously reported, we found that IMPDH2 retains a basal level of activity even in the presence of saturating GTP (25, 26). All but one mutant we tested retained significant activity up to 5 mM GTP (Fig. 2.1). The R341Q mutant was highly sensitive to GTP, with an IC50 of 80 µM (Fig. 2.1). Additionally, the L245P mutant could be inhibited at much higher GTP concentrations, with an estimated IC50 of 7 mM (Fig. 2.2). However this value is far above the usual physiological concentration range of GTP in human cells (59). Thus, each neurodevelopmental mutation dramatically compromises feedback inhibition by GTP, either increasing or decreasing the sensitivity of IMPDH2 to GTP.

2.2 Structural phenotypes of mutants vary.

Most of the IMPDH2 neurodevelopmental mutations characterized here are in or near the regulatory domain, which controls the extended-compressed structural transition. This led us to hypothesize that the loss of GTP regulation we observed arises from an inability to transition into the compressed, inhibited conformation. To assess changes to the structure and conformation in IMPDH2 mutants, we used negative stain electron microscopy. Under activating and inhibiting conditions for the WT enzyme, we have previously assessed whether the enzyme is extended or compressed by directly observing the helical rise of filaments (25–27). Because these mutants have normal basal activity, we anticipated that in the absence of GTP, the mutants should resemble the WT in the extended, active conformation. In the presence of GTP, which causes compression of WT filaments, we predicted we would not observe compression in the mutants that were insensitive to GTP inhibition. However, negative stain EM analysis of IMPDH2 revealed surprising large-scale structural differences among the mutants.

First, we examined IMPDH2 mutant structures in the absence of GTP, where all mutants retain WT activity (Fig. 2.3A). Under this condition, G207R, Q243H, L245P, K238R, N198S, K229del, and F114V closely resembled WT in the canonical extended and active conformation. However, S160del, R341Q, and K205E did not assemble filaments at all. S160del formed mostly tetramers in the presence of ATP, R341Q formed a mix of tetramers and octamers, and K205E formed only octamers. Surprisingly, both G113E and G113R were uniformly compressed, which has not previously been observed for IMPDH2 in the absence of GTP (21, 23–26). More surprising still, in the presence of GTP, all of the filament-competent disease mutants were able to assemble filaments in the compressed conformation, again excluding S160del and R341Q which formed only octamers, although it is not feasible to accurately measure whether these octamers are in the extended or compressed conformation from this data (Fig. 2.3B).

R341Q stands alone from the other disease mutations investigated here in both its heightened sensitivity to GTP (Fig. 2.1) and its mutation site being located on the opposite side of the catalytic domain, far from the regulatory domain (Fig. 1.2). Though R341 is not located within the filament assembly interface, it forms a salt bridge with D16 of a neighboring chain in the tetramer, positioning the N-terminus (Fig. 2.4). This interaction likely stabilizes both the formation of the tetramer and the filament assembly interface, allowing for polymerization. We hypothesize that mutating this arginine to a glutamine would break this key interaction, thus destabilizing filament formation as well as tetramer assembly. Because GTP binding induces bowing to the flat filament assembly interface of IMPDH2 (26), we conclude that the weakened tetramer contacts in R341Q would render this mutant to be highly sensitive to GTP-induced strain.

2.3 Filament assembly reduces sensitivity of IMPDH2 mutants to GTP.

We next investigated the effect of perturbing the filament assembly interface on the variants' sensitivity to GTP. The engineered mutation Y12A at the filament assembly interface of IMPDH2 disrupts polymerization, and increases sensitivity of IMPDH2 to GTP inhibition compared to the WT (25, 26). We introduced the Y12A mutation into each of the IMPDH2 mutants except for the R341Q mutant, which already has a disrupted filament assembly interface. We confirmed with negative stain that these double mutants do not form filaments (Fig. 2.5). Next, we performed GTP inhibition assays on the double mutants (Fig. 2.6). Because the S160del mutant does not form filaments at all, we anticipated that the Y12A mutation would not affect enzyme activity (Fig. 2.3). The S160del+Y12A mutant displayed no significant decrease in activity in the presence of GTP, as expected (Fig. 2.6). The other double mutants could be inhibited at higher GTP concentrations, with L245P+Y12A being the most sensitive (IC50 = 1.3 mM), followed by K238R+Y12A (IC50 = 1.9 mM). None of the double mutants were as sensitive to GTP inhibition as the non-assembly Y12A mutant alone (IC50 = 200 µM). This suggests that the mutations affect the octameric form of the enzyme as well, and assembly of the variants into filaments would further exacerbate downstream regulatory defects in the cell.

2.4 L245P filaments resist symmetric compression.

To investigate the structural basis for IMPDH2 dysregulation in mutants that appear structurally similar to the WT enzyme at low resolution, we determined high resolution structures of L245P in the presence of ATP and GTP. We chose L245P as representative of the most common structural phenotype we observed–filaments that undergo the extended to compressed transition in the presence of GTP despite retaining full activity (G207R, Q243H, L245P, K238R, N198S, K229del, F114V).

First, we determined the structure of L245P in the catalytically active, extended conformation, in the absence of GTP. Flexibility in WT IMPDH2 filaments under these conditions arises from heterogeneity in the extended and compressed conformations of protomers within each octamer, which can limit the resolution of cryo-EM structures. We previously developed an image processing strategy for the very flexible WT IMPDH2 filaments, which allows us to computationally separate uniformly extended from partially compressed (bent) filament segments (26). The approach also allows us to generate focused reconstructions of the repeating octameric subunit and the filament assembly interface. Following symmetry expansion and focused classification, we found that the majority of L245P segments were sorted into fully extended classes (73%), compared to only 17% fully extended WT IMPDH2 segments under these conditions (Fig. 2.7) (26). Thus, it appears that L245P reduces octamer flexibility in the active state, leading to a more uniformly extended structure than the very heterogeneous WT filaments.

The extended L245P structures refined to global resolutions that were significantly higher than our earlier WT structures: 2.0 Å for the filament assembly interface and catalytic core, and 2.6 Å resolution for the octamer-centered reconstruction (Fig. 2.7, Fig. 2.8). The mutation of L245 to proline is clear in the cryo-EM map and does not appear to perturb the conformation of the backbone around the mutation site relative to WT (Fig. 2.8E). IMP and NAD+ were clearly resolved in the active site, and ATP was well resolved in sites 1 and 2 in the regulatory domain (Fig. 2.9). Overall, the structures are nearly identical to the WT structure under this condition at the level of individual protomers, octamers, and the filament assembly interface (Fig. 2.8D). Some minor differences in loops of the regulatory domain likely reflect improved accuracy in model building at the improved resolution of the current reconstructions.

Next, we determined the structure of L245P in the presence of 20 mM GTP. At this high GTP concentration, we had previously observed that the WT IMPDH2 forms uniformly compressed filaments, with no significant population of extended or bent octamers (26). However, from initial two-dimensional classification of L245P helical segments, it was clear that the mutant filaments were very heterogeneous (Fig. 2.10, Fig. 2.11). The data processing approach described above allowed us to separate out asymmetric bent segments, which closely resemble bent segments of WT IMPDH2 observed only in the absence of GTP (26). The remaining symmetrically compressed filament segments comprise only about 13% of the data set (Fig. 2.10). Compared to the uniformly compressed WT, then, one consequence of the L245P mutation is to increase the heterogeneity of IMPDH2 filaments in the presence of GTP.

We used the symmetrically compressed filament segments to determine structures with global resolutions of 2.1 Å for the filament assembly interface and 3.0 Å for the octamer-centered reconstruction (Fig. 2.10). We also determined a structure of the asymmetric, bent filament segment at a global resolution of 2.7 Å (Fig. 2.10, 2.11C). Again, all ligands including GTP were well resolved (Fig. 2.9), and the filament interface was nearly identical to WT. The L245P protomer is also nearly identical to the WT protomer under this ligand condition (Fig. 2.11D). Thus, IMPDH2-L245P can adopt a canonical compressed structure in the presence of GTP. However, under conditions that support uniform compression and inhibition of the WT enzyme, the mutant remains in an ensemble of partially compressed states (Fig. 2.12).

2.5 G113E filament is compressed in the absence of GTP.

With negative stain EM, we found that both G113E and G113R assembled into compressed filaments in the presence of ATP (Fig. 2.3), a result not previously observed for the WT enzyme. G113 is located in the hinge region, near allosteric site 3. We hypothesized that a missense mutation to this site may allow for adenine nucleotides to bind in this guanine nucleotide-specific site and stabilize octamer compression. We collected a cryo-EM dataset of G113E in the presence of ATP and found that the filaments were conformationally homogenous and clearly compressed (Fig. 2.14). This dataset resulted in a 2.8 Å cryo-EM structure, revealing that, while ATP was clearly resolved in both allosteric sites 1 and 2 (Fig. 2.15D), there was no ATP occupying allosteric site 3 (Fig. 2.15C). Occupancy of this site was previously thought to be necessary for stabilizing the compressed state. Additionally, the side chain of G113E was found to be 4 Å from K242 across the hinge region, potentially within weak hydrogen bonding distance (Fig. 2.15C). A charged residue at this position may serve to stabilize the compressed conformation of the filament, explaining our negative stain results. Comparing this structure with the previously published structure of the compressed WT filament, we found that the finger domain was significantly shifted towards the Bateman domain (Fig. 2.15A). The only previously published WT structure with similar finger domain positioning is that of the compressed free octamer (Fig. 2.15B). However, the significance of this finger domain position remained unclear.

2.6 S160del disrupts dimerization of Bateman domains.

S160 is located between allosteric sites 1 and 2, and is capable of hydrogen bonding with the phosphates of ATP in site 1 (Fig. 2.17A). We wondered if the deletion of S160 would weaken nucleotide binding in allosteric site 1, or if its deletion would result in misfolding of the Bateman domain.

To test this, we collected a cryo-EM dataset of S160del in the presence of saturating GTP, ATP, IMP, and NAD+. As was observed with negative stain EM, no filaments were present (Fig. 2.16). The dataset was compositionally heterogeneous, with 28% of the selected particles classified as tetramers and 68% of the selected particles classified as an interfacial octameric assembly, in which the filament assembly interface was formed but the Bateman domains were not dimerized (Fig. 2.16, Fig. 2.17B). The tetramer refined to a global resolution of 2.3 Å with C4 symmetry imposed, and the interfacial octamer refined to 2.1 Å with D4 symmetry imposed (Fig. 2.16). In both the tetramer and interfacial octamer reconstructions, the Bateman domains were not resolved, suggesting that they were highly flexible as expected (26) (Fig. 2.17C, E). Substrates were clearly resolved in the active site in both reconstructions (Fig. 2.17D, F). The catalytic domain of the interfacial octamer reconstruction was nearly identical to that of WT hIMPDH2, with a Cα RMSD of 0.6 Å (Fig. 2.19A). The tetramer adopted a more bowed confirmation as compared to the interfacial octamer (Fig. 2.19B). Overall, the catalytic domains of the tetramer and interfacial octamer reconstructions were unremarkable as compared to the WT enzyme under the same conditions.

Surprisingly, 4% of the selected particles (31,924 particles) were classified as canonical octamers, with Bateman dimers clearly resolved in the 2D class averages (Fig. 2.16, 2.17B). These particles adopted a preferred orientation in ice as has been previously observed for canonical octamers of IMPDH (26), impeding high-resolution structural characterization. However, the presence of the canonical octamer in this dataset, and the secondary structure observed in the 2D class averages, suggest that while S160del clearly disrupts the stability of the Bateman dimer interface, possibly by weakening the binding of nucleotides in allosteric site 1, it does not cause misfolding of the Bateman domain.

2.7 Discussion.

Mutations in IMPDH1 were previously shown to cause the retinal diseases Leber congenital amaurosis and retinitis pigmentosa (46–50). Like the IMPDH2 mutations characterized here, a subset of IMPDH1 mutations cluster near the allosteric domain or inter-domain hinge, and disrupt GTP inhibition (21, 27). Importantly, four of the five IMPDH1 mutations that disrupt GTP regulation prevent IMPDH1 from adopting the compressed conformation, which we proposed as the mechanism of GTP dysregulation. We anticipated that the IMPDH2 mutations studied here would have the same effect, but were surprised to see that in each case we could measure, GTP appeared to cause compression of IMPDH2 in low-resolution negative stain micrographs (Fig. 2.3). Because all but one of these enzymes retain high activity levels in the presence of GTP (Fig. 2.1), this result suggested that contrary to prior models, compression of IMPDH2 alone is not sufficient for allosteric inhibition.

IMPDH2-L245P structures provide insight into the seeming contradiction of the enzyme retaining WT activity in a compressed conformation. We found that the canonical extended and compressed states are virtually identical to the WT structures under the same conditions, including the binding of GTP to inhibitory allosteric sites. However, the conformational variability of filaments in different ligand states varies significantly. Active WT IMPDH2 is in an ensemble of structural states with different numbers of compressed and extended protomers within octamers giving rise to multiple bent conformations, and only a minority (17%) of octameric filament segments were classified as symmetrically extended (26). By comparison, the vast majority (73%) of L245P octamers are symmetrically extended, suggesting that one effect of the mutation is to rigidify the enzyme in the extended state. Conversely, under high concentrations of GTP, WT IMPDH2 octamers are uniformly compressed, while only a minority of L245P octamers (13%) are fully compressed, the majority being in an ensemble of bent conformational states that resemble the active WT ensemble. That is, what appeared in low resolution negative stain micrographs to be the compressed conformation was revealed to be an ensemble of partially compressed conformations using higher resolution cryo-EM approaches. Thus, L245P appears to disrupt GTP regulation by shifting the conformational equilibrium away from the inhibited, compressed conformation (Fig. 2.12). We hypothesize that introducing a proline to the hinge region at position 245 may restrict the conformational change from extended to compressed.

Additionally, our results suggest that some of the point mutations may dysregulate IMPDH2 through different mechanisms. Two mutations at residue 113 appear to cause IMPDH2 to be constitutively in a compressed conformation in the absence of GTP (Fig. 2.3A). These mutations raise the question of how compressed IMPDH2 filaments can retain full WT levels of activity and suggest that compression alone is not sufficient to inactivate the enzyme. Our 2.8 Å filament structure of the G113E mutant in the presence of ATP showed that it was compressed without occupancy of a nucleotide in allosteric site 3 (Fig. 15C). This compressed conformation may be stabilized by a glutamate at 113 weakly hydrogen bonding with a lysine residue in the catalytic domain (Fig. 2.15C). The G113E and G113R variants, therefore, may serve as a useful tool for dissecting previously unappreciated mechanisms of regulation of IMPDH2.

Three of the mutants–R341Q, K205E, and S160del–were all found to disrupt filament assembly in different ways. With cryo-EM structures of the recombinantly purified S160del mutant, we showed that while the catalytic domain of S160del was identical to the WT as expected, the Bateman domains were highly flexible and unable to dimerize efficiently. S160del primarily assembles into interfacial octamers and tetramers, though it is surprisingly still capable of assembling into the canonical octamer, suggesting that deletion of S160 may weaken the Bateman dimer interface, preventing the formation of the canonical octamer which is necessary for inhibition. R341Q appears to disrupt filament assembly in a different way. By breaking a key tetramer-stabilizing contact near the N-terminus, it likely disrupts both the tetramer interface and the filament assembly interface (Fig. 2.4). With a weakened tetramer interface, it may be more susceptible to GTP-induced bowing of the filament assembly interface. Finally, K205E only disrupts filament assembly in the presence of ATP, not GTP (Fig. 2.3). This result is surprising, given that K205 forms the same Bateman interface contact in both the extended and compressed conformations (26).

Because these mutations do not all lead to the same structural phenotypes at the level of polymerization or conformational state, it will be important to characterize each one to elucidate mechanisms of disease for each. Understanding individual mechanisms of dysregulation may also provide insight into variation in the onset and severity of disease phenotypes (Table 1.1).

Assembly of IMPDH2 into filaments exacerbates the reduction in GTP sensitivity of the disease mutations. We have previously established the role for polymerization in reducing IMPDH2 sensitivity to GTP inhibition, which increases the working range of the enzyme under conditions of elevated purine nucleotide demand (26, 27). When filament assembly was blocked, all of the point mutants except for S160del partially restored sensitivity to GTP inhibition, although not to WT levels (Fig. 2.6). The sensitivity to GTP inhibition of S160del, which itself prevents filament assembly, was not restored by introduction of our engineered non-assembly mutation Y12A.

Our results suggest potential therapeutic approaches that might be considered for treating patients with IMPDH2-associated developmental disorders. All but one of these mutations are gain-of-function, allowing high levels of IMPDH activity at otherwise inhibitory concentrations of GTP. One approach might be the use of known IMPDH inhibitors, to reduce the activity of the enzyme (60–62). Alternative approaches that target IMPDH2 assembly into filaments might also prove effective in some cases; for example disrupting IMPDH2-L245P filament assembly reduces the IC50 for GTP into a more physiologically relevant range and might reduce activity sufficiently to be therapeutically useful. For R341Q, the only loss-of-function mutant characterized here, efforts to stabilize the tetramer interface and N-terminus may restore the IC50 for GTP. Future work investigating the treatment of IMPDH2-associated disorders using small molecules in cell-based systems and model organisms may prove fruitful.

In both IMPDH1 and IMPDH2, disease-linked mutations in and around the Bateman domain result in the same type of biochemical defect affecting the nervous system. In the case of IMPDH1, this defect results in the degeneration of photoreceptors, possibly due to their unique dependence on IMPDH1 for ATP and cGMP (63–67). Imbalance of nucleotide pools in photoreceptors leads to photoreceptor death (68–70). In the case of IMPDH2, the defect results in neurodevelopmental disorders. In both cases, the dysregulation of IMPDH disrupts the delicate balance of purine pools in the nervous system.

For gain-of-function mutations, selective inhibitors of IMPDH2 could be explored as therapeutics for ameliorating the symptoms of diseases associated with IMPDH2 hyperactivity. Mycophenolic acid (MPA) is a pan-IMPDH inhibitor that is currently used as an immunosuppressive drug by uncompetitive inhibition in the NAD+ site (60, 61). However, MPA is not isoform-specific and has several documented side effects (71, 72). As IMPDH1 generally provides low, basal-level activity in most cells, use of an IMPDH2-specific inhibitor to treat diseases associated with IMPDH2 mutation would be desirable to reduce off-target effects. One reported IMPDH2-specific inhibitor, Sappanone A, is predicted to associate covalently near allosteric site 2 and inhibit through a mechanism like GTP (62). Several natural products were also previously identified as selective inhibitors of IMPDH2, such as shikonin, diosmetin, and Cryptotanshinone (73). Identifying small molecule inhibitors of IMPDH2 and investigating their mechanisms of action could be useful in future drug discovery efforts for the treatment of dystonia or other diseases caused by IMPDH2 mutation.

Figure 2.1: IMPDH2 disease mutations disrupt GTP inhibition.

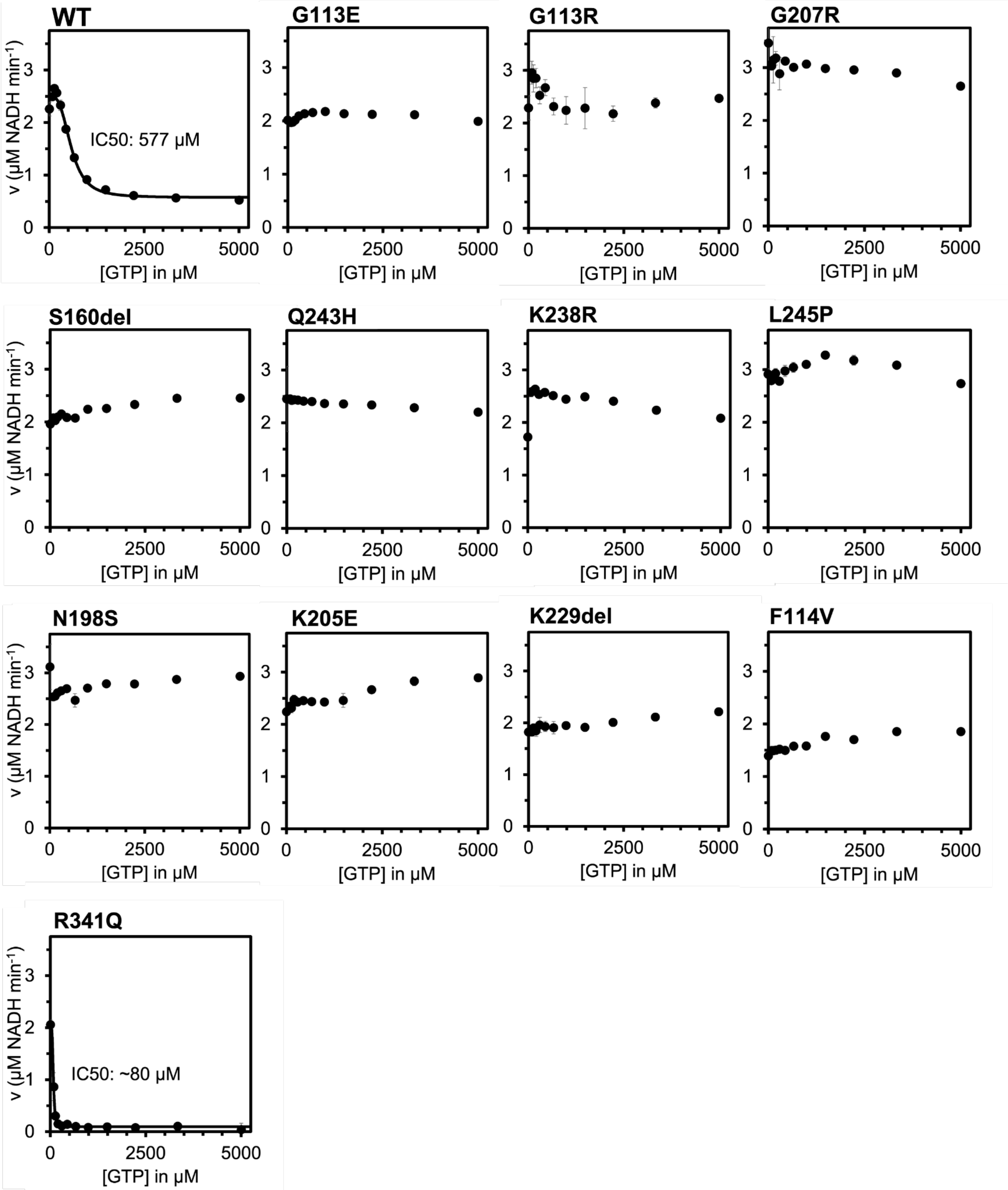

GTP inhibition of WT IMPDH2 and IMPDH2 neurodevelopmental variants. Each data point represents the average initial rate of three reactions. Error bars represent standard deviation for n = 3 technical replicates. Velocities were calculated from the change in absorbance at 340 nm. Reactions were initiated with 300 μM NAD+ and contained 1 μM enzyme, 1 mM ATP, 1 mM IMP, 1 mM MgCl2, and varying concentrations of GTP. IMP, inosine 5′ monophosphate; IMPDH, inosine 5′ monophosphate dehydrogenase.

Figure 2.2: L245P is inhibited by high concentrations of GTP.

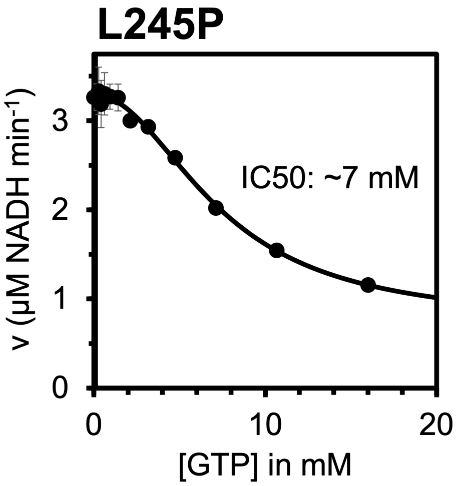

GTP inhibition curve of the L245P variant up to 16 mM GTP. Each data point represents the average initial rate of three reactions. Error bars represent standard deviation for n=3 technical replicates. Velocities were calculated from the change in absorbance at 340 nm. Reactions were initiated with 300 µM NAD+ and contained 1 µM enzyme, 1 mM ATP, 1 mM IMP, 1 mM MgCl2 and varying concentrations of GTP.

Figure 2.3: Negative stain EM reveals low-resolution differences between some mutants.

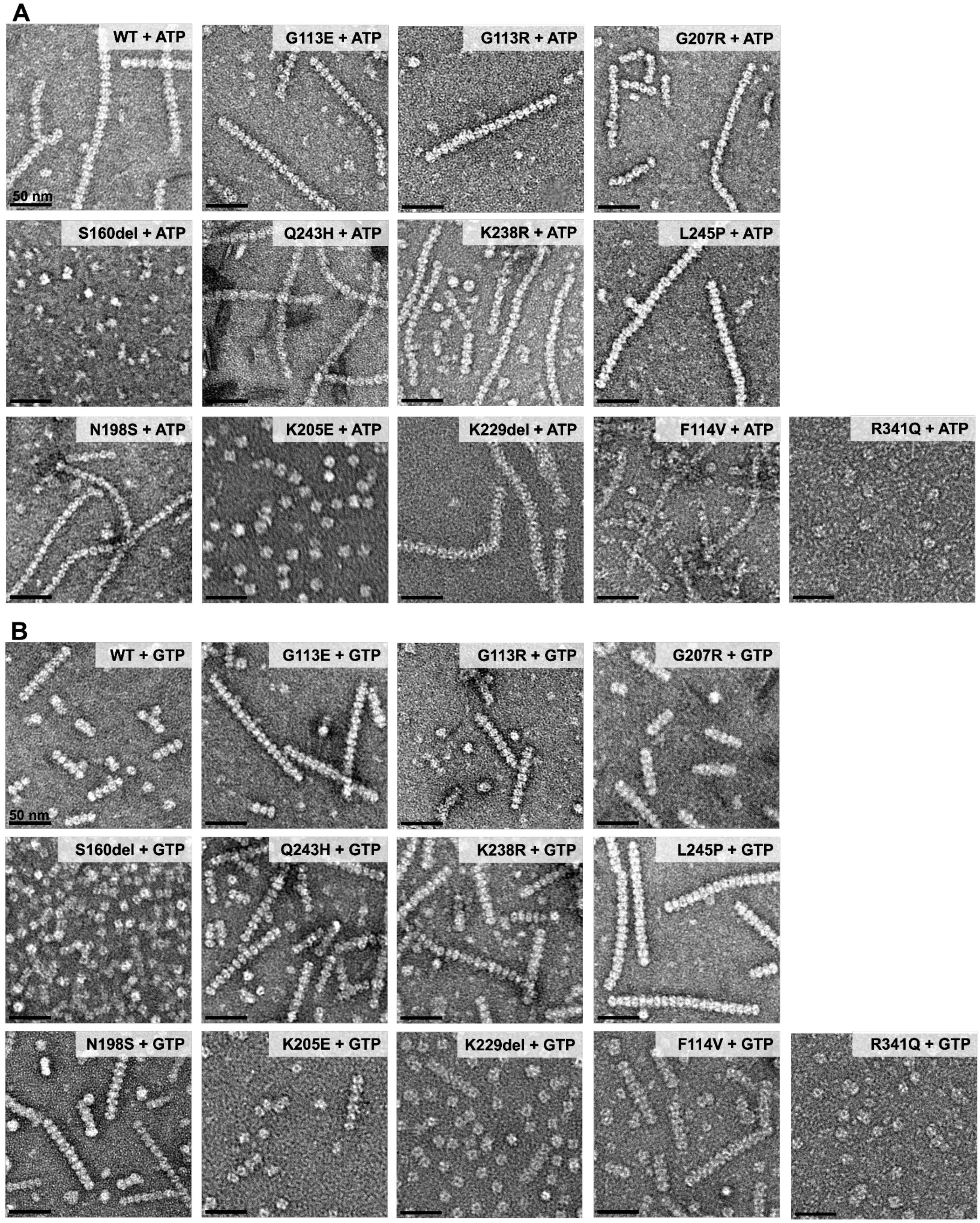

Representative negative stain images of 2 μM enzyme with either 1 mM ATP and 1 mM MgCl2 (A) or 5 mM GTP (B).

Figure 2.4: R341 makes a tetramer-stabilizing contact with D16.

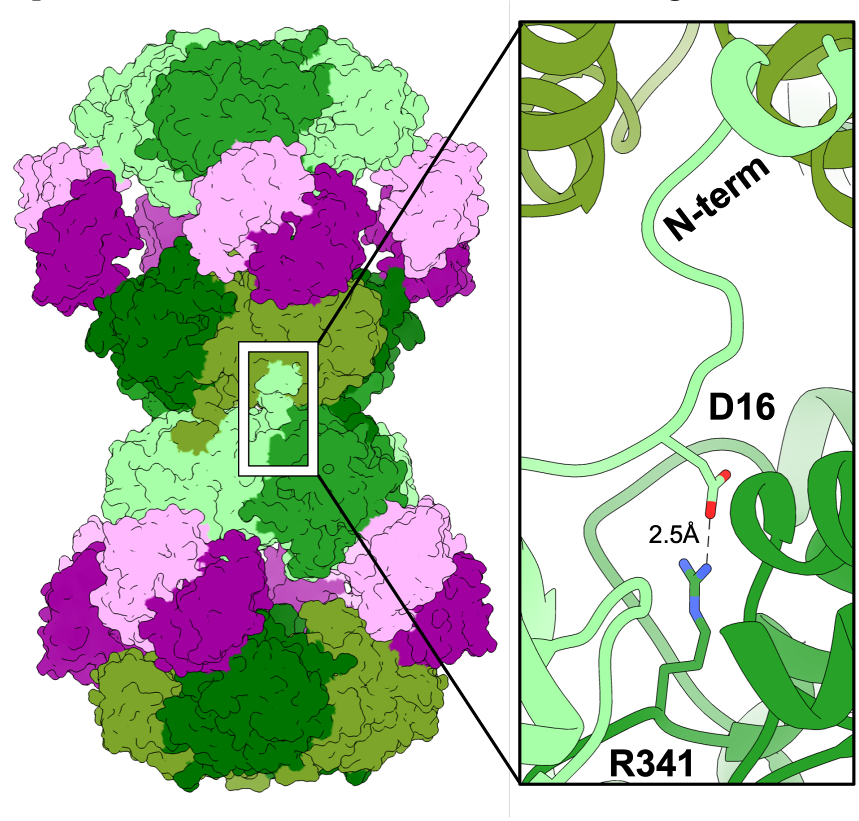

Model of the extended IMPDH2 filament (PDB: 6U8N) highlighting the position of R341 relative to the N-terminus and its contact with D16 in a neighboring chain.

Figure 2.5: Negative stain EM of non-assembling disease mutants.

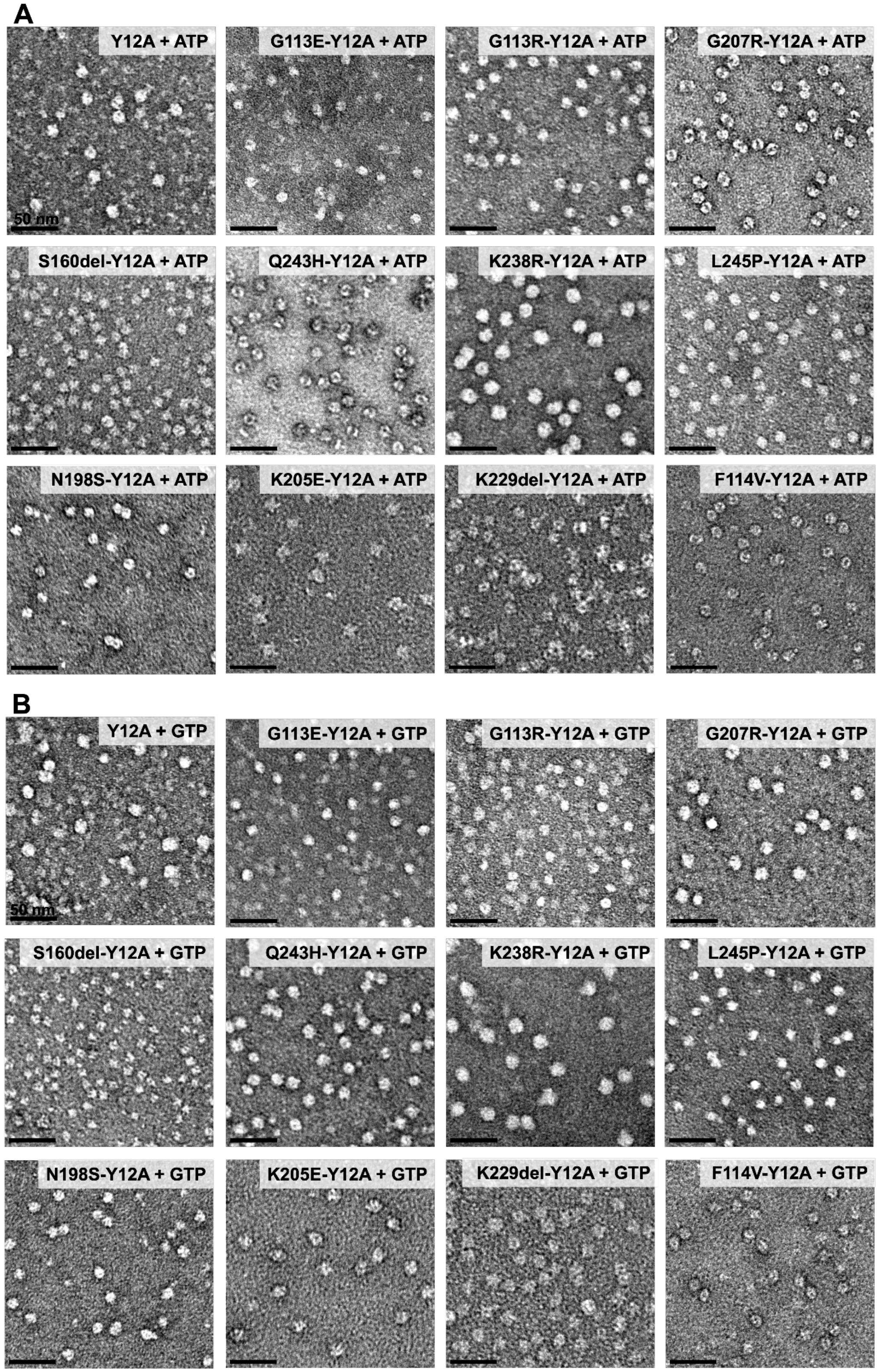

Representative negative stain images of 0.5 µM enzyme with either 1 mM ATP and 1 mM MgCl2 (A) or 5 mM GTP (B). Filaments were not observed in either condition.

2.6 IMPDH2 disease mutations disrupt GTP inhibition of free octamers.

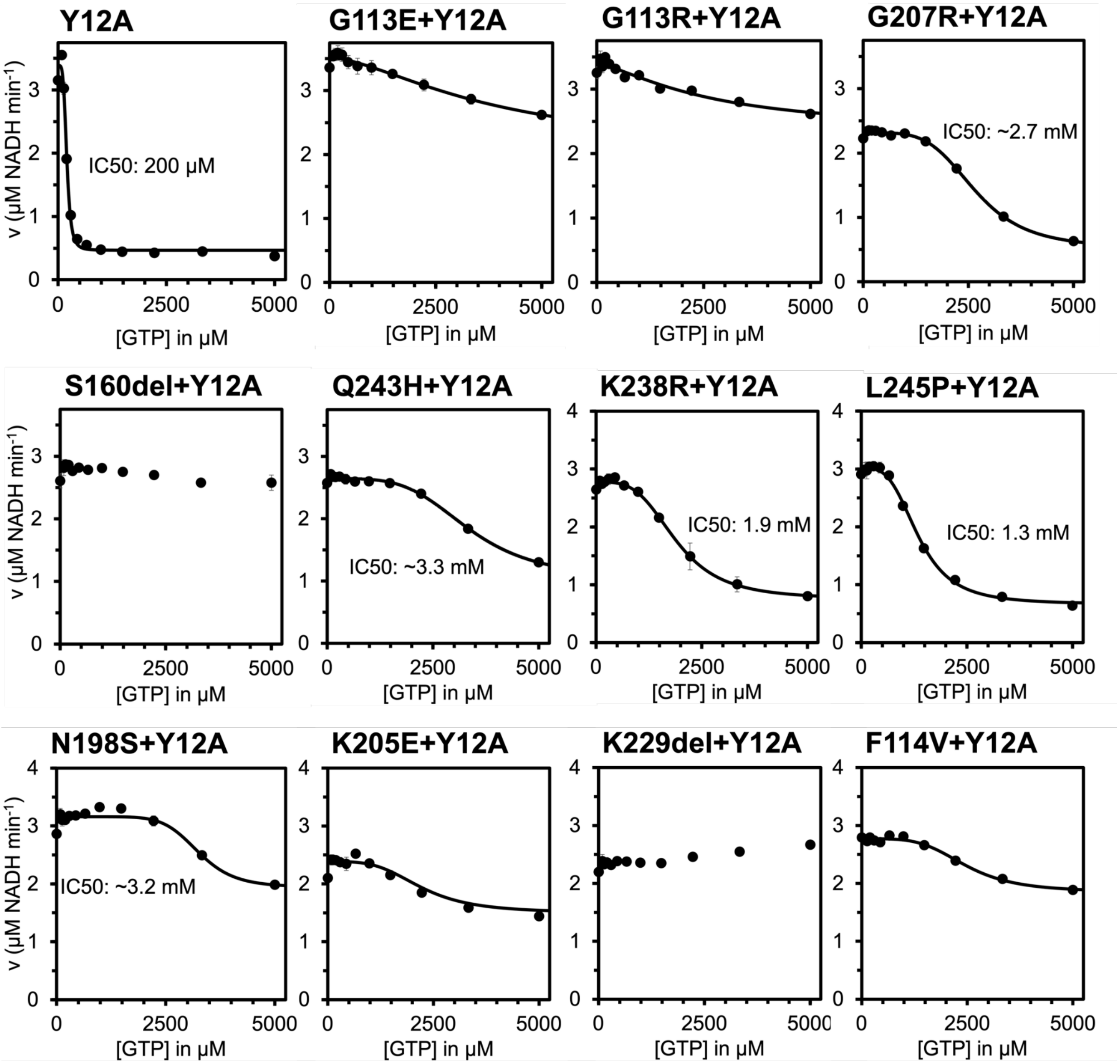

GTP inhibition curves of Y12A nonassembly mutant and Y12A/disease mutant double mutants of IMPDH2. Each data point represents the average initial rate of three reactions. Error bars represent standard deviation for n = 3 technical replicates. Velocities were calculated from the change in absorbance at 340 nm. Reactions were initiated with 300 µM NAD+ and contained 1 µM enzyme, 1 mM ATP, 1 mM IMP, 1 mM MgCl2, and varying concentrations of GTP.

2.7 L245P extended filaments cryo-EM data processing workflow in RELION.

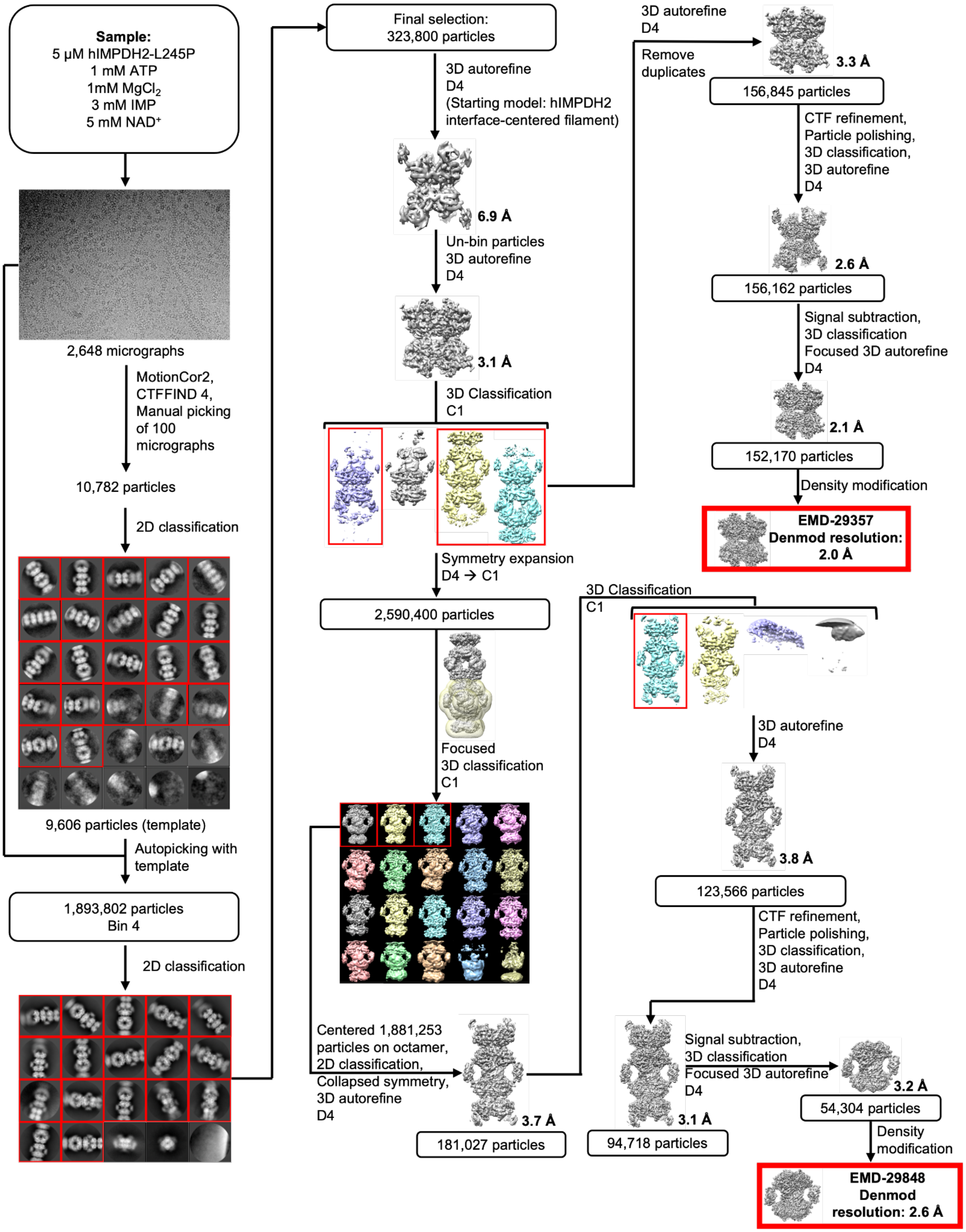

Figure 2.8: L245P mutant adopts similar extended conformation as WT.

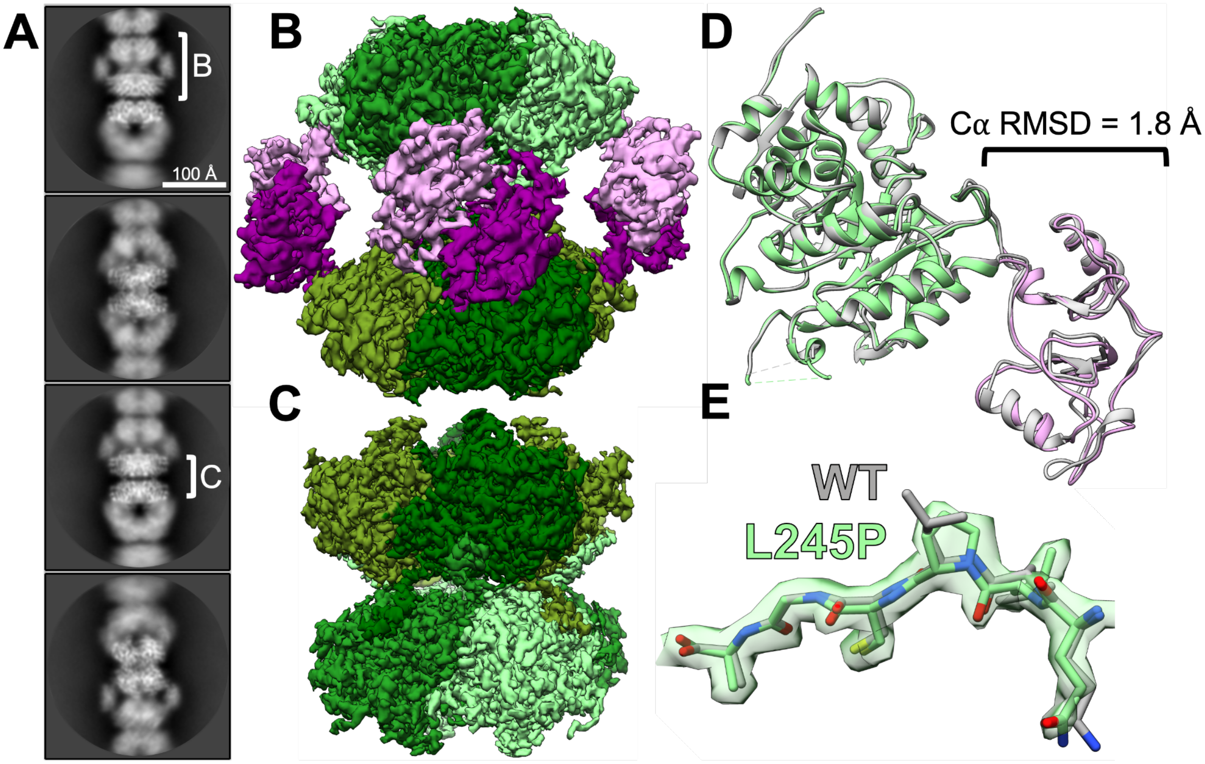

Representative 2D class averages of L245P filaments in the presence of 1 mM ATP, 3 mM IMP, 5 mM NAD+, and 1 mM MgCl2 (A). White brackets illustrate the regions on the filament where refinement was focused to produce reconstructions shown in panels B and C. Final cryo-EM reconstructions of octamer-centered (B) and interface-centered (C) filament segments. Regulatory domains are colored in shades of pink, and catalytic domains are colored in shades of green. Alignment of the L245P octamer-centered ribbon model (color; PDB 8G8F) to the WT ribbon model (gray; PDB 6U8N) at the catalytic domain (green). Calculation of Cα RMSD at the regulatory domain (pink) shows minor differences in the structure of the monomer (D). The density around the mutation site shows that the backbone structure is not affected (E).

Figure 2.9: Volume around ligands in extended and compressed L245P structures.

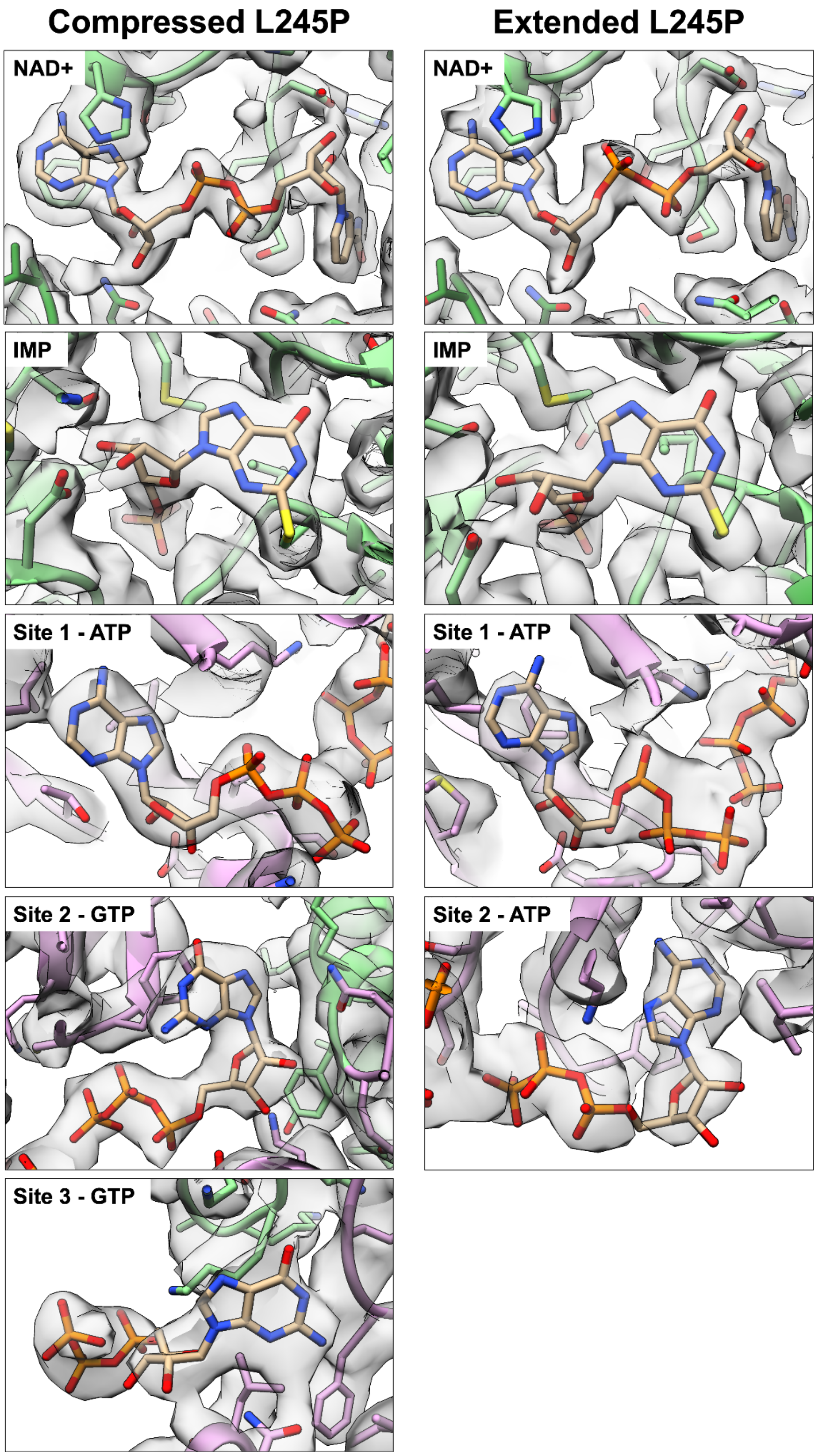

All ligands are resolved in the L245P extended and compressed structures. The catalytic domain is colored in green, and the regulatory domain is colored in pink.

2.10 L245P compressed filaments cryo-EM data processing workflow in RELION.

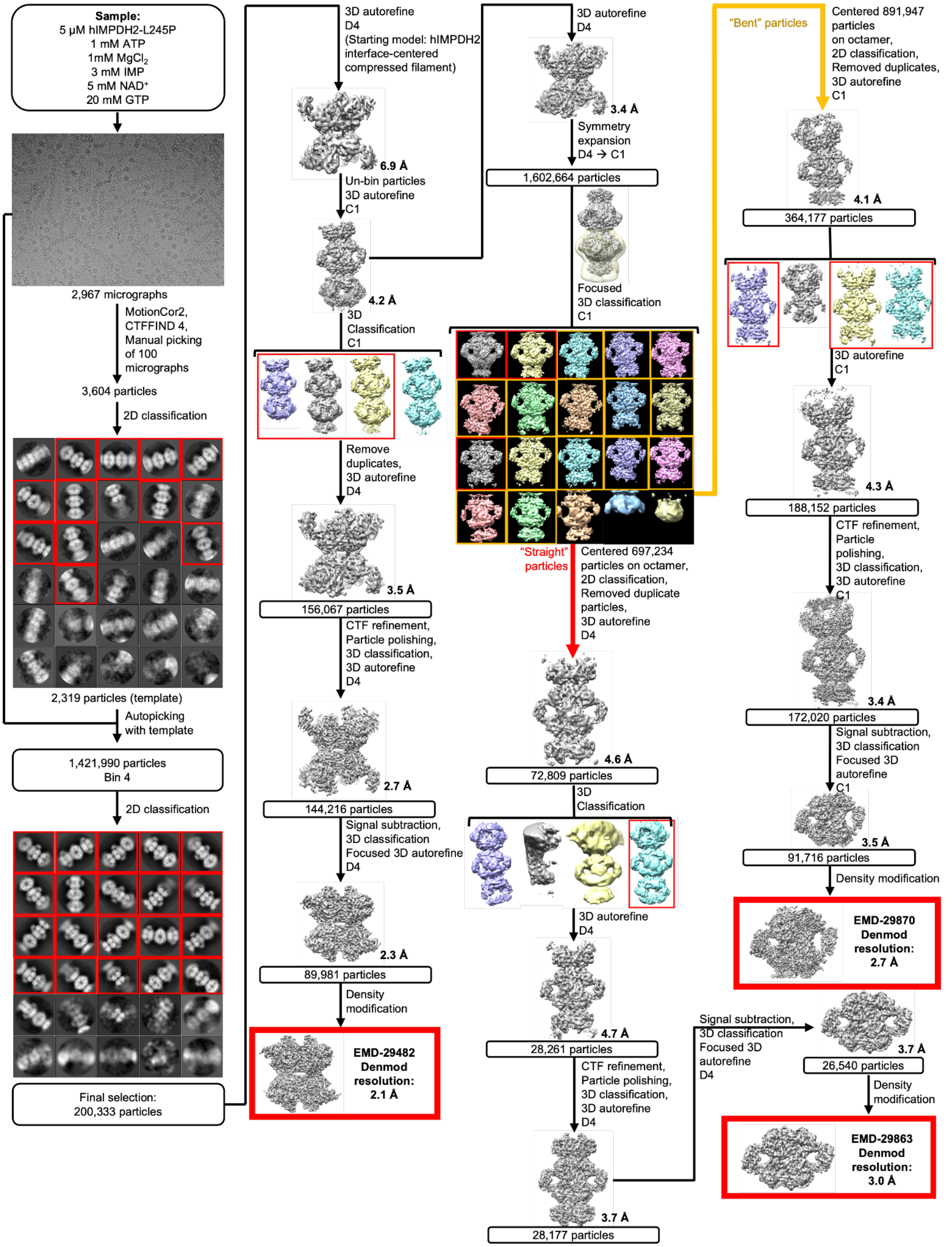

Figure 2.11: L245P filaments are flexible in the presence of GTP.

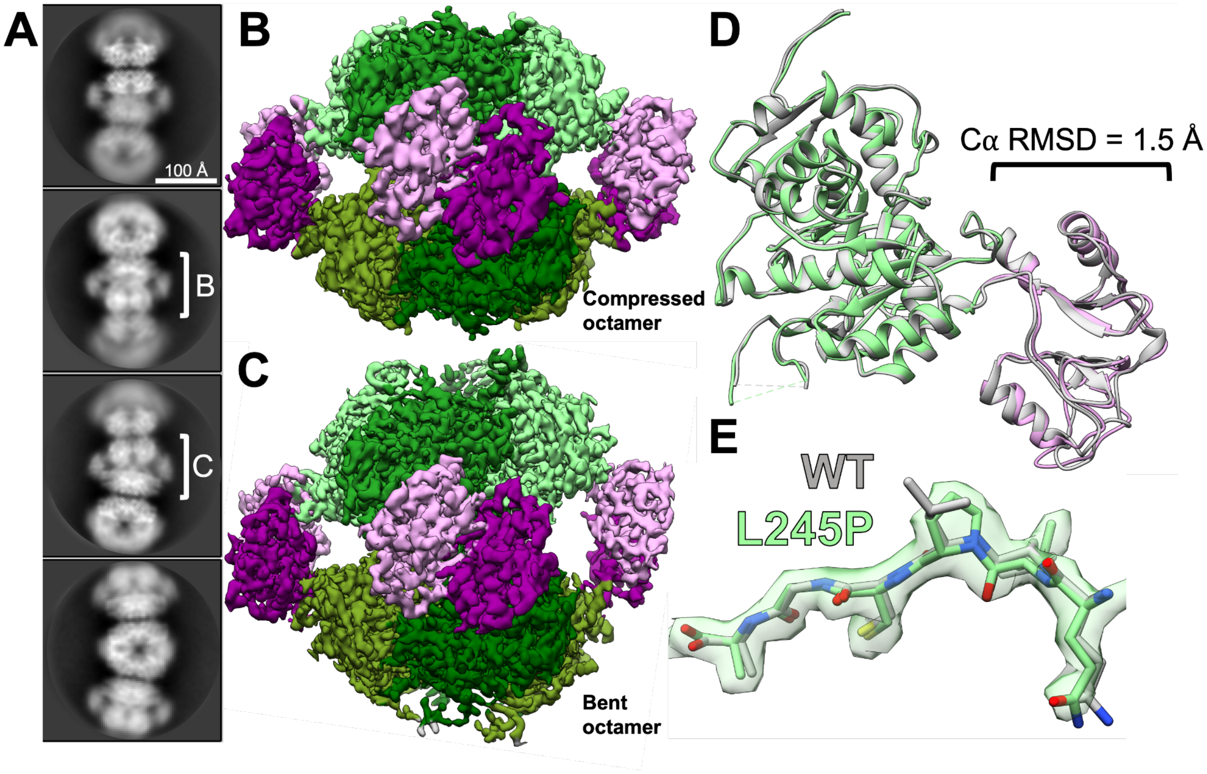

Representative 2D class averages of L245P filaments in the presence of 20 mM GTP, 1 mM ATP, 3 mM IMP, 5 mM NAD+, and 1 mM MgCl2 (A). White brackets illustrate the regions on the filament where refinement was focused to produce reconstructions shown in panels B and C. Final cryo-EM reconstructions of straight octamer-centered (B) and bent octamer-centered (C) filament segments. Regulatory domains are colored in shades of pink, and catalytic domains are colored in shades of green. The filament assembly interface reconstruction is shown in Fig. S8. A model was built into the symmetrically compressed octamer reconstruction. Alignment of the L245P straight octamer-centered ribbon model (color; PDB 8G9B) to the WT ribbon model (gray; PDB 6U9O) at the catalytic domain (green). Calculation of Cα RMSD at the regulatory domain (pink) again shows minor differences in the structure of the monomer (D). The density around the mutation site shows that the backbone structure is not affected (E).

2.12 Model for the effect of L245P on IMPDH2 conformational equilibrium.

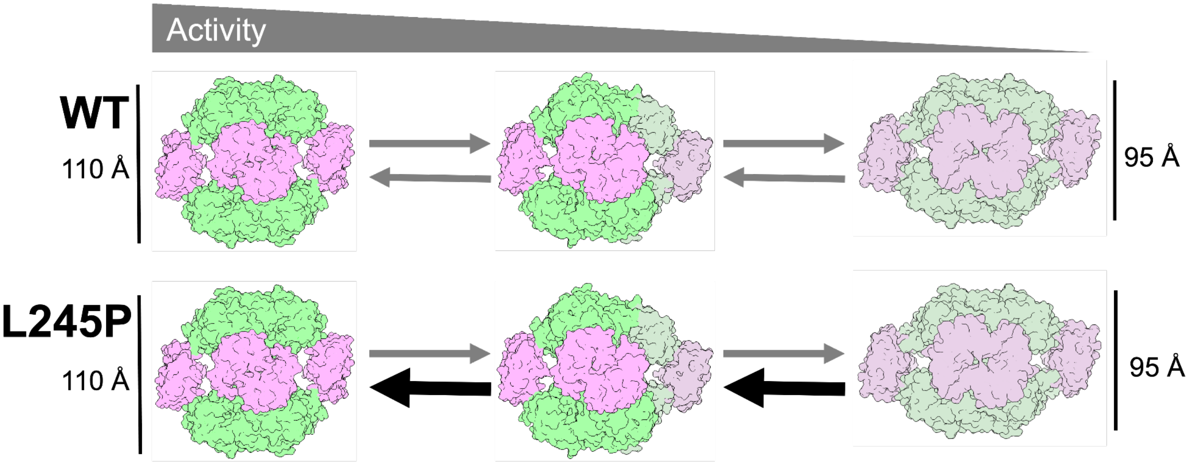

WT IMPDH2 samples conformational space between fully extended and fully compressed octamers. L245P shifts that equilibrium to favor extended and bent conformations, resisting complete compression and maintaining activity.

Figure 2.13: FSC curves for L245P structures.

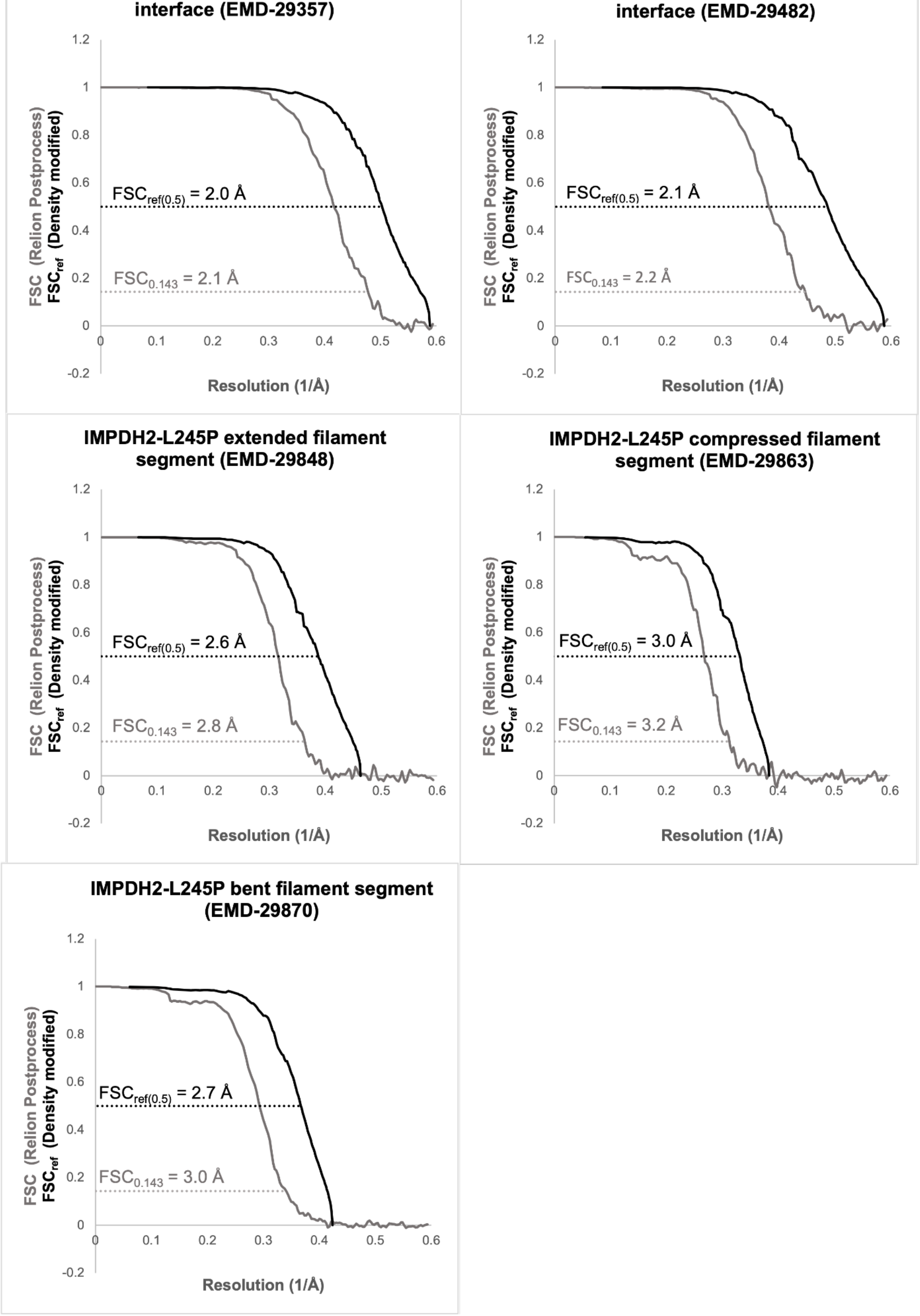

IMPDH2-L245P extended filament interface (EMD-29357)

IMPDH2-L245P compressed filament interface (EMD-29482)

IMPDH2-L245P extended filament segment (EMD-29848)

IMPDH2-L245P compressed filament segment (EMD-29863)

IMPDH2-L245P bent filament segment (EMD-29870)

Figure 2.14: G113E cryo-EM data processing workflow and FSC curve.

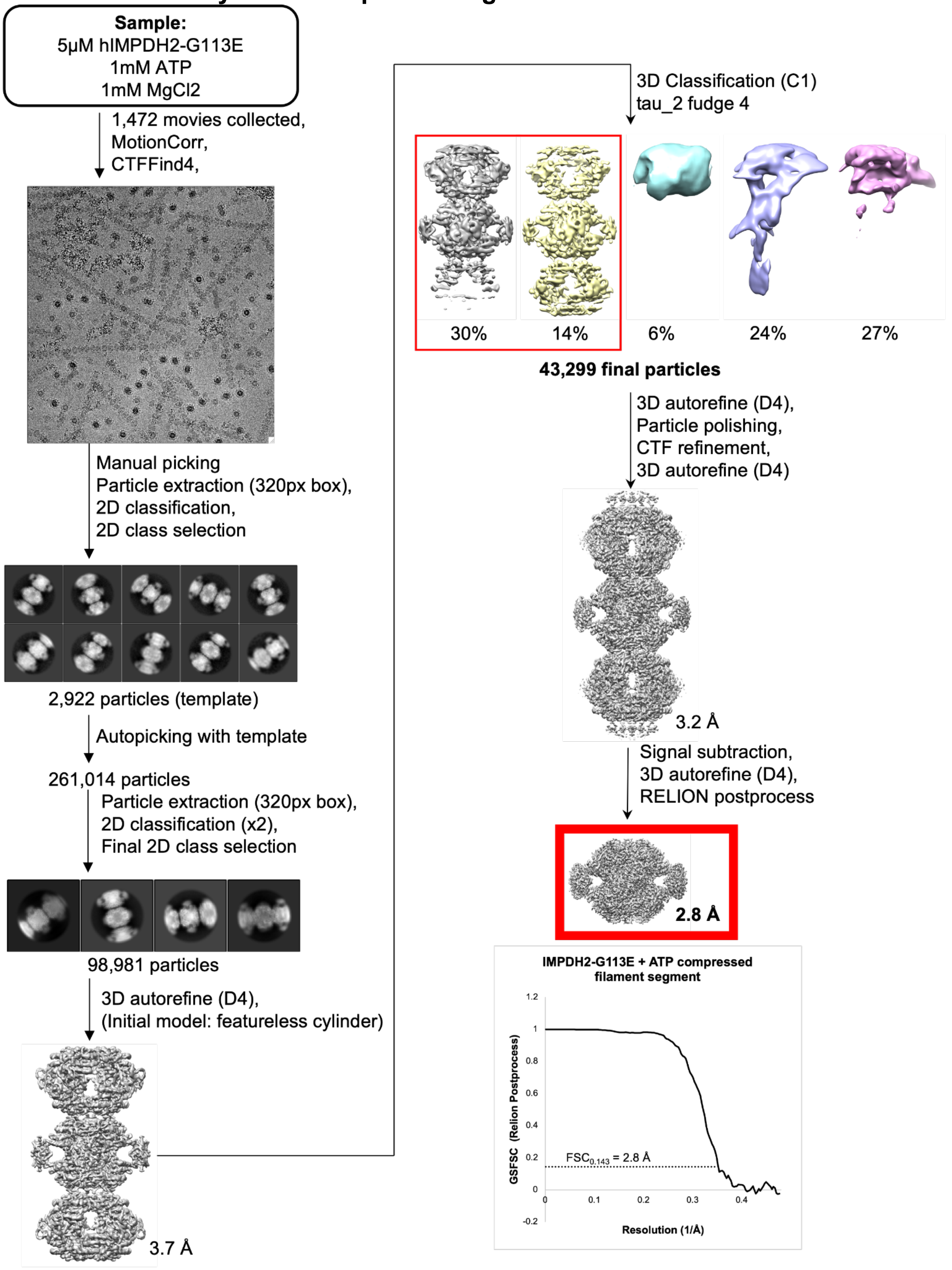

Figure 2.15: G113E compressed filament segment structure.

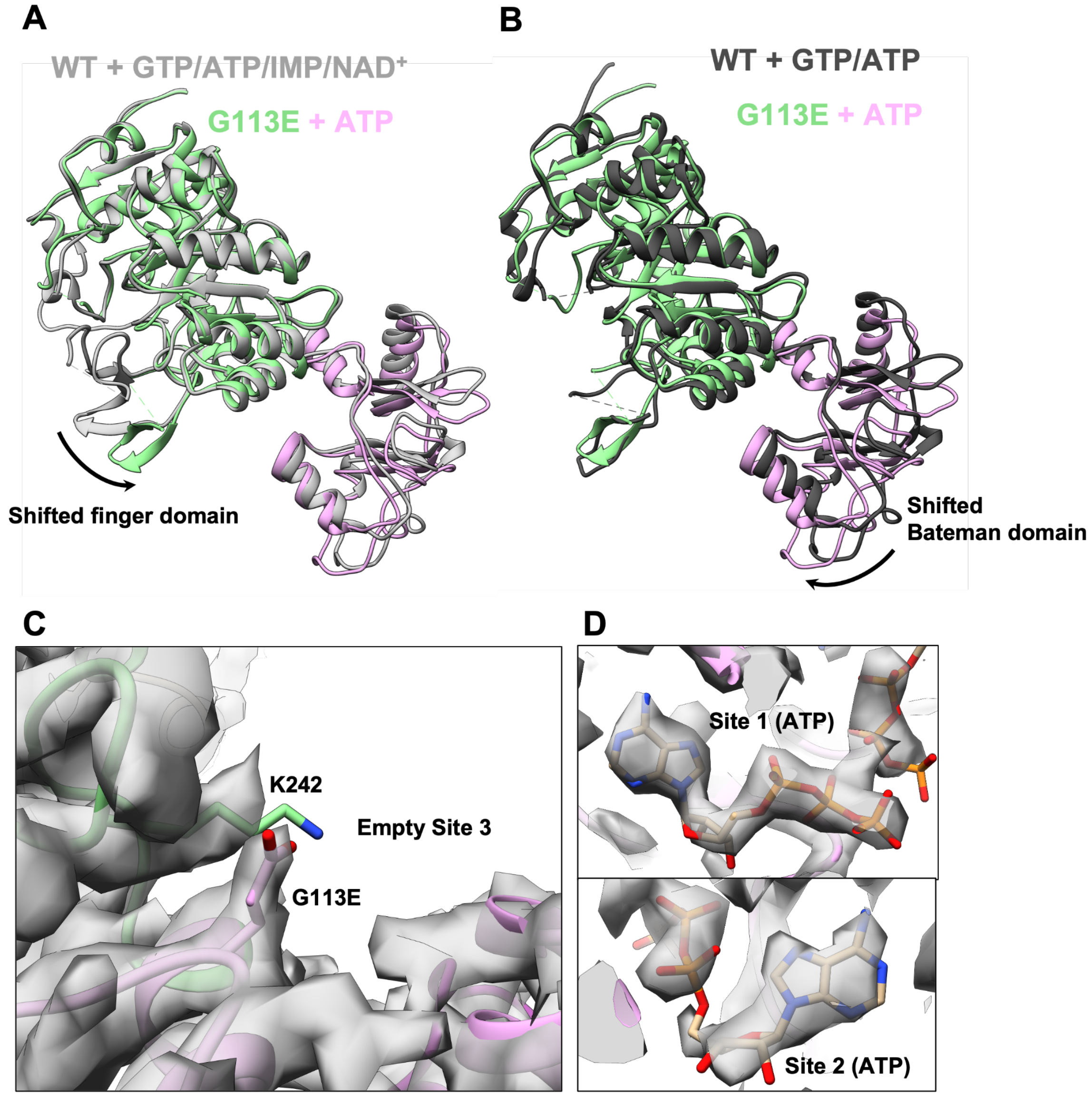

A. G113E+ATP filament structure aligned at the catalytic domain (green) with the structure of a compressed WT IMPDH2 filament (PDB: 6U9O). The finger domain is significantly shifted towards the Bateman domain in the G113E structure.

B. G113E+ATP filament structure aligned at the catalytic domain with the compressed free octamer structure of WT IMPDH2 (PDB: 6UC2). The finger domain is in a similar placement as G113E, but the Bateman domain of G113E is shifted relative to the catalytic domain.

C. The volume around residue 113 and allosteric site 3. No nucleotide is observed in allosteric site 3.

D. Volume around ATP molecules in site 1 and site 2.

Figure 2.16: S160del cryo-EM data processing workflow in cryoSPARC.

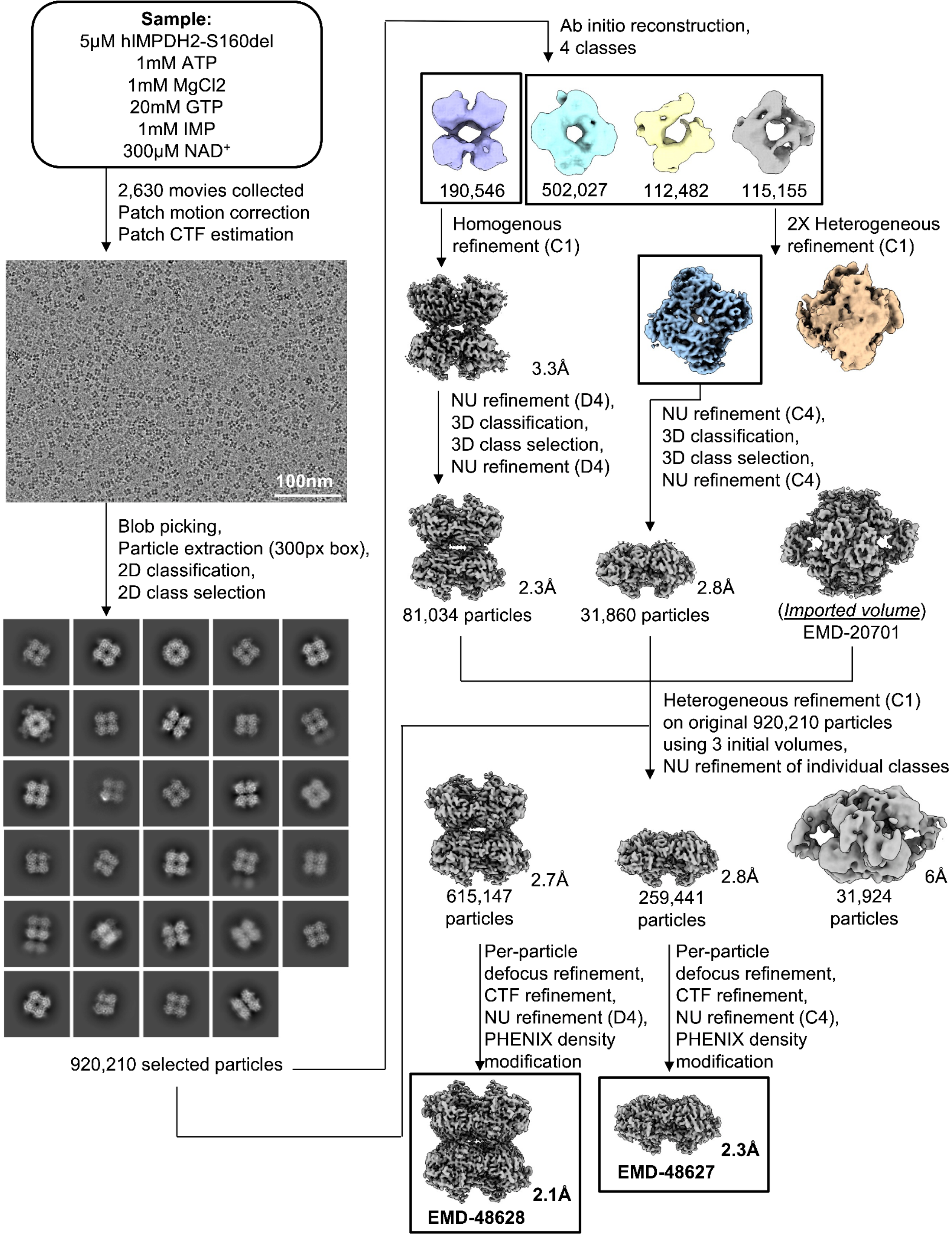

Figure 2.17: S160del cryo-EM structures.

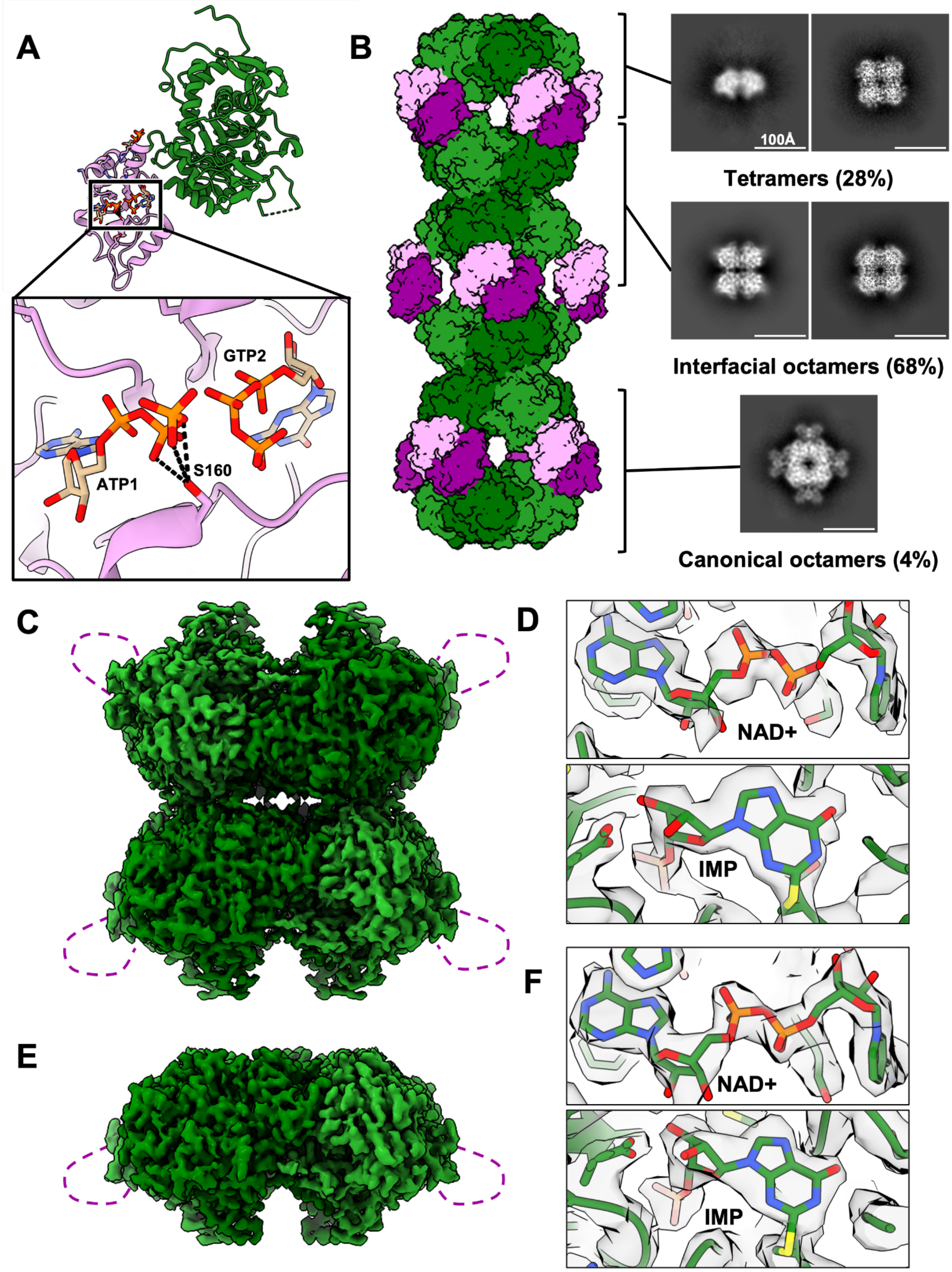

A. Structure of the hIMPDH2 monomer under physiologically relevant ligand conditions (with bound ATP, GTP, IMP, NAD+). Serine 160 is located within the regulatory Bateman domain and is proximal to both ATP in site 1 and GTP in site 2 when bound. Potential hydrogen bonds to the phosphates of ATP in site 1 are displayed as dashed lines.

B. Distribution of S160del assembly states as determined by cryo-EM. Selected 2D class averages are shown. The majority of selected particles (68%) are classified as interfacial octamers with a smaller subset (28%) of tetramers. Only 4% of selected particles existed in the canonical octamer state, but secondary structure is apparent in the Bateman domains.

C-D. Cryo-EM map of the S160del interfacial octamer (C). Only the catalytic domain is resolved (green). The disordered Bateman domain is represented as a purple dashed line. Both NAD+ and IMP are bound (D).

E-F. Cryo-EM map of the S160del tetramer (E). Only the catalytic domain is resolved (green). The disordered Bateman domain is represented as a purple dashed line. Both NAD+ and IMP are bound (F).

Figure 2.18: FSC curves and viewing direction distributions of S160del cryo-EM structures.

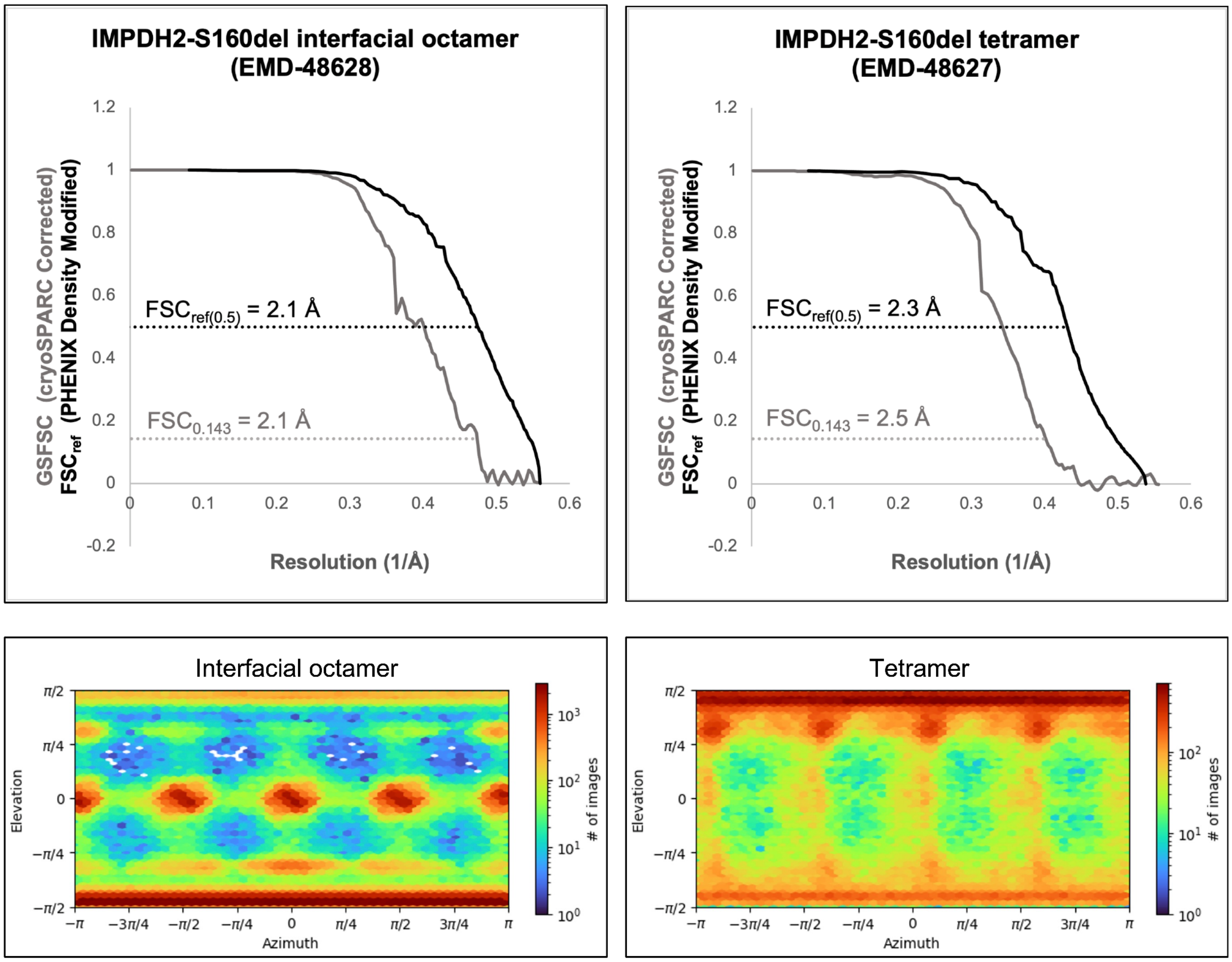

Figure 2.19: Model comparisons of S160del interfacial octamer and tetramer structures.

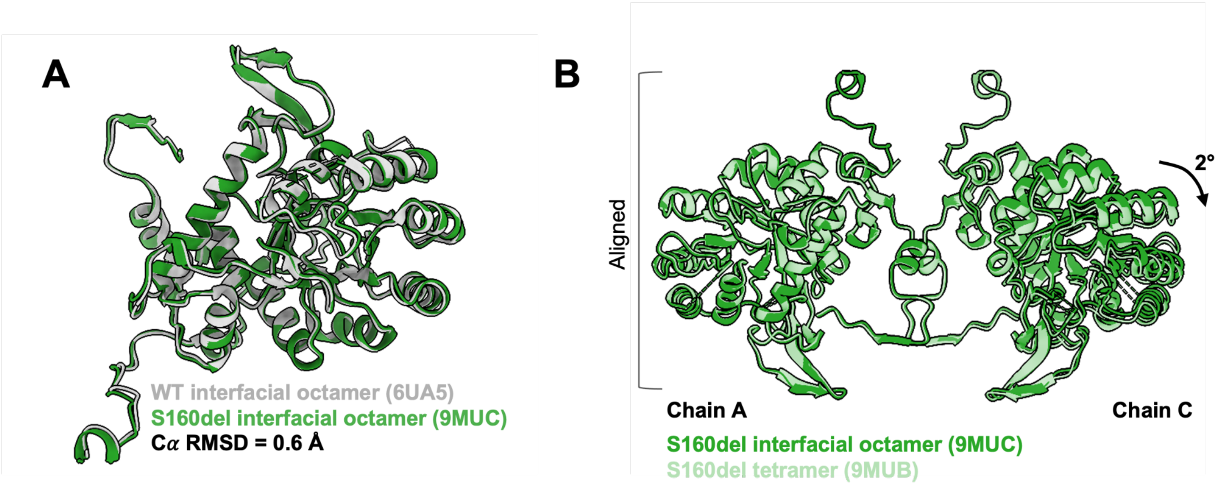

A. The S160del interfacial octamer structure (green) aligned to the previously published WT hIMPDH2 interfacial octamer structure (gray). Bateman domains are highly mobile and unresolved in both structures. The alpha-carbon RMSD of 0.6 Å suggests no major differences in the catalytic domain.

B. The S160del interfacial octamer aligned to the S160del tetramer at Chain A. The filament assembly interface of the interfacial octamer is flat compared to the tetramer, which is bowed by 2 degrees.

Table 2.1: Kinetic parameters of IMPDH2 variants compared to WT IMPDH2.

Variant	IMP		NAD$^+$		$V_{max\ app}$
	$K_{0.5}$ (μM)	Hill	$K_{0.5}$ (μM)	Hill	(μM NADH min^{-1})
WT	45.6	7.4	44.9	5.3	2.2 ± 0.1
G113E	17.6	2.3	44.9	2.8	2.4 ± 0.8
G113R	20.1	2.8	31.5	3.3	2.0 ± 0.5
G207R	35.5	2.8	37.1	5.8	2.1 ± 0.1
S160del	15.1	2.8	25.8	5.7	1.7 ± 0.2
Q243H	52.1	4.9	60.2	3.0	3.6 ± 0.5
L245P	16.9	1.7	24.6	3.5	2.8 ± 0.4
K238R	17.2	2.5	33.4	9.0	1.4 ± 0.1
N198S	25.7	3.2	53.0	5.5	2.2 ± 0.03
K205E	31.7	3.9	53.0	4.1	2.5 ± 0.1
K229del	17.9	3.1	44.6	3.3	2.0 ± 0.3
F114V	22.2	2.6	36.2	2.6	1.8 ± 0.02
R341Q	120.9	1.0	89.0	0.9	1.5 ± 0.2

Table 2.2: Data collection and refinement statistics for L245P structures.

	hIMPDH2-L245P extended filament interface	hIMPDH2-L245P extended filament segment	hIMPDH2-L245P compressed filament interface	hIMPDH2-L245P compressed filament segment	hIMPDH2-L245P bent filament segment
Ligands	ATP, IMP, NAD+	ATP, IMP, NAD+	GTP, ATP, IMP, NAD+	GTP, ATP, IMP, NAD+	GTP, ATP, IMP, NAD+
PDB ID	8FOZ	8G8F	8FUZ	8G9B	N/A
EMDB ID	EMD-29357	EMD-29848	EMD-29482	EMD-29863	EMD-29870
Data collection and refinement					
Magnification	105,000	105,000	105,000	105,000	105,000
Voltage (kV)	300	300	300	300	300
Electron exposure (e$^-$/Å^2)	60	60	60	60	60
Defocus range (μm)	-1.71 — -0.27	-1.71 — -0.27	-1.74 — -0.28	-1.74 — -0.28	-1.74 — -0.28
Pixel size (data collection) (Å)	0.4215	0.4215	0.4215	0.4215	0.4215
Pixel size (reconstruction) (Å)	0.843	0.843	0.843	0.843	0.843
Micrographs (no.)	2,648	2,648	2,967	2,967	2,967
Initial particles (no.)	1,893,802	1,893,802	1,421,990	1,421,990	1,421,990
Final particles (no.)	152,170	54,304	89,981	26,540	91,716
Symmetry imposed	D4	D4	D4	D4	C1
Map resolution range, Relion postprocess (Å)	2.06 – 3.37	2.63 – 4.59	2.13 – 4.10	3.05 – 5.21	2.76 – 5.91
Resolution, Relion postprocess (0.143 FSC) (Å)	2.1	2.8	2.2	3.2	3.0
Resolution, density modified (0.5 FSC$_{ref}$) (Å)	2.0	2.6	2.1	3.0	2.7
Model refinement and validation					
Initial model (PDB ID)	6U8E	6U8N	6U8S	6U9O	N/A
R.m.s. deviations					
Bond lengths (Å)	0.0083	0.0136	0.0109	0.0164	N/A
Bond angles (°)	0.80	1.25	1.01	1.27	N/A
MolProbity score	1.17	2.05	1.31	1.84	N/A
Clashscore	2.94	7.63	4.61	10.84	N/A
C-beta deviations	0	0	0	1	N/A
Rotamer outliers (%)	1.31%	1.87%	1.17%	0.60	N/A
Ramachandran plot					
Favored (%)	99.47%	93.61%	97.92%	95.85%	N/A
Allowed (%)	0.53%	5.98%	2.08%	3.99%	N/A
Disallowed (%)	0.00%	0.41%	0.00%	0.15%	N/A

Table 2.3: Data collection and refinement statistics for G113E structure.

	hIMPDH2-G113E compressed filament segment
Ligands	ATP
PDB ID	N/A
EMDB ID	N/A
Data collection and refinement	
Magnification	130,000
Voltage (kV)	300
Electron exposure ($e^-/Å^2$)	90
Nominal defocus range (µm)	-2.50 — -0.59
Pixel size (data collection) (Å)	0.525
Pixel size (reconstruction) (Å)	1.05
Micrographs (no.)	1,472
Initial particles (no.)	261,014
Final particles (no.)	43,299
Symmetry imposed	D4
Resolution, Relion postprocess (0.143 FSC) (Å)	2.8
Model refinement and validation	
Initial model (PDB ID)	6U9O
R.m.s. deviations	
Bond lengths (Å)	0.0197
Bond angles (°)	1.01
MolProbity score	2.43
Clashscore	8.35
C-beta deviations	0.00%
Rotamer outliers (%)	8.80%
Ramachandran plot	
Favored (%)	96.19%
Allowed (%)	3.81%
Disallowed (%)	0.00%

Table 2.4: Data collection and refinement statistics for S160del structures.

	hIMPDH2-S160del Interfacial octamer	**hIMPDH2-S160del Tetramer**
Ligands	GTP, ATP, IMP, NAD+	GTP, ATP, IMP, NAD+
PDB ID	9MUC	9MUB
EMDB ID	EMD-48628	EMD-48627
Data collection and refinement		
Magnification	45,000	45,000
Voltage (kV)	200	200
Electron exposure (e^-/Å^2)	50	50
Nominal defocus range (μm)	-1.8 — -1.2	-1.8 — -1.2
Pixel size (data collection) (Å)	0.4425	0.4425
Pixel size (reconstruction) (Å)	0.885	0.885
Micrographs (no.)	2,630	2,630
Initial particles (no.)	1,393,912	1,393,912
Final particles (no.)	615,147	259,441
Symmetry imposed	D4	C4
Resolution, CryoSPARC postprocess (0.143 FSC) (Å)	2.1	2.5
Resolution, Phenix density modification (0.5 FSC_{ref}) (Å)	2.1	2.3
Model refinement and validation		
Initial model (PDB ID)	6UA5	6UA5
R.m.s. deviations		
Bond lengths (Å)	0.0162	0.0162
Bond angles (°)	1.90	1.99
MolProbity score	1.17	1.02
Clashscore	1.33	1.35
C-beta deviations	0.00%	0.62%
Rotamer outliers (%)	2.57%	1.49%
Ramachandran plot		
Favored (%)	98.20%	97.88%
Allowed (%)	1.80%	2.12%
Disallowed (%)	0.00%	0.00%

Chapter 3. Using dinucleoside polyphosphates to further interrogate the effects of S160 deletion from IMPDH2

Adapted from:

O’Neill, A. G., McCartney, M. E., Wheeler, G. M., Patel, J. H., Sanchez-Ramirez, G., Kollman, J. M., & Wills, A. E. (2025). An IMPDH2 variant associated with neurodevelopmental disorder disrupts purine biosynthesis and somitogenesis. bioRxiv, 2025-05.

3.1 S160del mutant assembles into filaments with dinucleoside polyphosphates.

We previously showed that the deletion of S160 significantly disfavors filament assembly. This is likely a result of shifting important contacts at the Bateman dimer interface that are downstream of residue 160 and/or reducing affinity for nucleotide binding to allosteric site 1 or 2 (Fig. 3.1). The interaction of opposing finger domains within a compressed IMPDH octamer is thought to be responsible for inhibition of IMPDH2 (Fig. 1B). Finger domains would not be positioned to interact at all in the free tetramers or interfacial octamers observed in our previous cryo-EM dataset of S160del (Fig. 2.17B). However, the small population of canonical octamers that we observed suggested that S160del can form the Bateman dimer interface in the presence of adenine and guanine nucleotides. Dinucleoside polyphosphates have been reported to bind across allosteric sites 1 and 2 of human IMPDH2 with 100x higher affinity than ATP or GTP alone (74). We hypothesized that we could stabilize the Bateman dimer interface of S160del by incubating with either Ap5A or Ap5G. We used negative stain EM to screen for the effects of these ligands on filament assembly.

Incubation of WT hIMPDH2 with Ap5A resulted in extended and flexible filaments, while incubation with Ap5G resulted in symmetrically compressed filaments, matching our previous results with ATP and GTP (26) (Fig. 3.2B). In contrast, S160del formed compressed filaments with either Ap5A or Ap5G, suggesting that the selectivity of nucleotide binding might be impaired in the S160del mutant (Fig. 3.2A). Additionally, S160del filaments, but not WT filaments, disassembled upon addition of IMP and NAD+ (Fig. 3.2A), suggesting that the motions that occur during the catalytic cycle may introduce strain to the Bateman dimer interface, which we hypothesized to be weakened by the deletion of S160.

Interestingly, the addition of GTP to S160del filaments that were formed with Ap5A, but not Ap5G, also caused disassembly (Fig. 3.2A). WT filaments formed with either Ap5A or Ap5G did not disassemble with the addition of GTP (Fig. 3.2B). The observed differences between S160del and WT filaments prompted further *in vitro* characterization of these structures.

3.2 S160del filaments remain insensitive to GTP inhibition.

After establishing that S160del can form filaments with dinucleoside polyphosphates, we next sought to test whether these filaments were sensitive to GTP inhibition. We assayed S160del and WT IMPDH2 in the presence or absence of Ap5G and GTP (Fig. 3.3A). The filaments that formed with the addition of Ap5G, GTP, IMP, and NAD+ were compressed for both S160del and WT (Fig. 3.3B). Interestingly, these S160del filaments retained full activity, suggesting that the effect of S160del on filament formation is independent from its effect on allosteric regulation (Fig. 3.3C).

We further probed the activity of S160del and WT in different dinucleoside polyphosphate states and found that S160del maintained activity in all conditions (Fig. 3.4). WT IMPDH2 was fully inhibited by 1mM Ap5G alone, suggesting that this concentration was saturating all allosteric sites. Interestingly, WT and S160del displayed similar levels of activity in the presence of both Ap5A and GTP, and this level of activity was higher than the basal level of activity. WT IMPDH2 activity was also nearly doubled in the presence of Ap5A alone. The significance of these results remains to be determined, but the differences in behavior between WT and S160del prompted higher-resolution structural characterization with cryo-EM.

3.3 S160del filaments adopt different conformations than WT filaments.

We first collected a cryo-EM dataset of S160del with 1mM Ap5A. The consensus reconstruction from this dataset confirmed that these filaments were compressed (Fig 3.5). The core of the filament was D4 symmetric and well resolved, with a global resolution of 2.8 Å. However, the Bateman domains were unresolved, suggesting a high degree of conformational heterogeneity. To visualize this heterogeneity, C4 symmetry expansion and 3D variability analysis focused around one quarter of the octamer revealed that the Bateman dimers were sampling a range of states along the side of the filament, while the core of the filament remained stably compressed (Fig. 3.5, 3.6). While one protomer was extended, the other protomer across the Bateman dimer interface could compress, allowing the octamer to remain compressed despite conformational changes at the protomer level. Focused 3D classification of these states revealed additional heterogeneity within the Bateman dimer, preventing high resolution characterization of the Bateman domain.

For a direct comparison to the WT enzyme, we collected a dataset of WT hIMPDH2 incubated with 1mM Ap5A (Fig. 3.7). Filaments in this dataset were extended, as expected, with a rise of 110 Å (Fig. 3.5). The finger domains and active site were disordered, as previously observed in IMPDH samples lacking IMP (PDB: 5MCP). The structure of the WT enzyme bound to Ap5A was nearly identical to previous structures of WT enzyme bound to ATP (26), suggesting that dinucleoside polyphosphate binding to sites 1 and 2 does not introduce artifacts to filament assembly.

To attempt to resolve differences at the Bateman dimer interface and around residue 160, we next solved cryo-EM structures of WT and S160del in the presence of Ap5G and GTP. By negative stain, these filaments appeared identical (Fig. 3.2). In both cryo-

EM datasets, the particles were conformationally homogenous and rigidly compressed (Fig. 3.9, 3.10). Both structures refined to sub 3 Å resolution, enabling model building (Fig. 3.8A, E). The Ap5G ligand was clearly resolved spanning sites 1 and 2 in both structures (Fig. 3.8C, G). At the Bateman dimer interface, there were clear differences in the rotamers involved in Bateman dimer contacts (Fig. 3.8D, H). In the WT IMPDH2 filament, D164 forms a salt bridge with R224 across the Bateman dimer interface (Fig. 3.1). This was recapitulated in the presence of Ap5G and GTP (Fig. 3.8D). In the S160del structure under the same condition, the neighboring phenylalanine residue flips rotamers, displacing both the aspartate and the arginine. Therefore, a key Bateman dimer contact is broken as a result of S160 deletion, weakening the interface.

Because S160del + Ap5G/GTP filaments remained intact in the presence of substrates, we wanted to observe these filaments under active turnover conditions. We collected a dataset of S160del in the presence of Ap5G, GTP, IMP, and NAD+ (Fig. 3.11, 3.12). In contrast to all previous S160del structures, the filaments in this dataset were conformationally heterogenous in a similar fashion as the previously described L245P dataset, primarily adopting “bent” conformations. After selecting specifically for filament segments and employing reference-based motion correction to boost resolution, the final structure did not improve beyond 3.2 Å in resolution with relaxed D4 symmetry imposed (Fig. 3.12). Filament bending was clearly observed following C4 symmetry expansion and focused 3D variability analysis around one quarter of the octamer (Fig. 3.12). Focusing in on the finger domains in each of these frames, we observed finger domain motions that were coordinated with filament bending (Fig. 3.11B). In the frame with the best resolved Bateman dimer, the finger domains adopted a position strikingly similar to the previously described G113E filament structure and both the WT and S160del Ap5G/GTP structures (Fig. 3.13). This finger domain position also fits well into the S160del + Ap5A map. In the final frame of the series, the finger domains switch to a position similar to what has previously been observed in WT IMPDH2 filament structures (PDB: 6U8N and 6U9O). This motion of finger domains in actively cycling S160del filaments may be related to motions during the catalytic cycle, as no heterogeneity was observed in the S160del + Ap5G/GTP dataset lacking substrates (Fig. 3.9).

3.4 Discussion.

In order to isolate the effects of S160del on filament formation and GTP inhibition, we showed that we can stabilize the formation of S160del filaments by incubating with dinucleoside polyphosphates, Ap5A and Ap5G, which bind to hIMPDH with high affinity (74). Interestingly, while Ap5G promoted S160del polymerization in a compressed conformation, these filaments remained insensitive to GTP inhibition, suggesting that the deletion of S160 has an effect on allosteric regulation beyond destabilizing filament formation, linking S160del to the other constitutively compressed mutants G113E and G113R (Fig. 3.3).

We further characterized the differences in behavior between WT and S160del filaments in the presence of dinucleoside polyphosphates with negative stain and cryo-EM. Interestingly, S160del filaments formed with either Ap5A or Ap5G disassembled when substrates were added (Fig. 3.2). During the catalytic cycle of IMPDH, the large-scale rearrangement of the catalytic domain (12) may strain the Bateman interface enough to break apart these weakened S160del filaments.

In the presence of Ap5A, WT filaments were extended. S160del + Ap5A filaments were compressed, with finger domains serving to stabilize the central octamer while Bateman domains flexibly sampled a range of states along the side of the filament (Fig. 3.5). In the presence of Ap5G and GTP, we observed a lost contact at the Bateman dimer in S160del, which likely serves to weaken the interface (Fig. 3.8). In all of these conditions, S160del was found to be catalytically active (Fig. 3.4).

In actively turning over S160del filaments, we observed finger domain motions coordinated to filament bending motions (Fig. 3.11B). Previous work has implicated the finger domains to be important for both IMPDH activity and inhibition. Interestingly, mutations which disrupt the secondary structure of the finger domain in *Ashbya gossypii* IMPDH were found to significantly reduce IMPDH activity (21). Future work will shed light on the specific role of the finger domain in the catalytic cycle of hIMPDH2, but the similarities observed between our G113E and S160del structures described here suggest that there may be a unifying explanation for how allosteric regulation is disrupted for these compressed mutants.

Figure 3.1: Bateman dimer interface contacts in WT hIMPDH2.

Extended Bateman dimer interface contacts (6U8N)

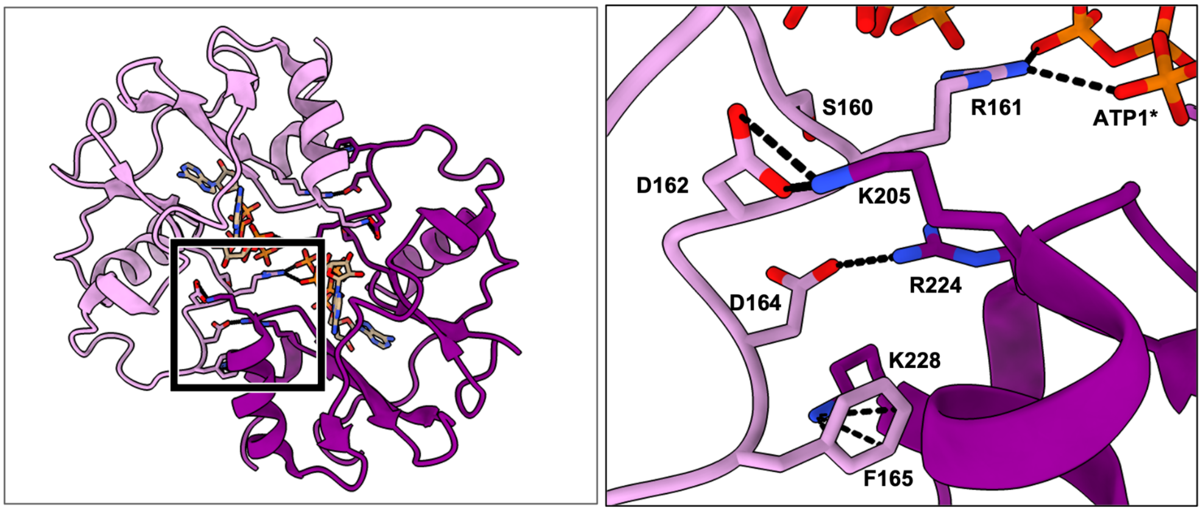

Compressed Bateman dimer interface contacts (6U9O)

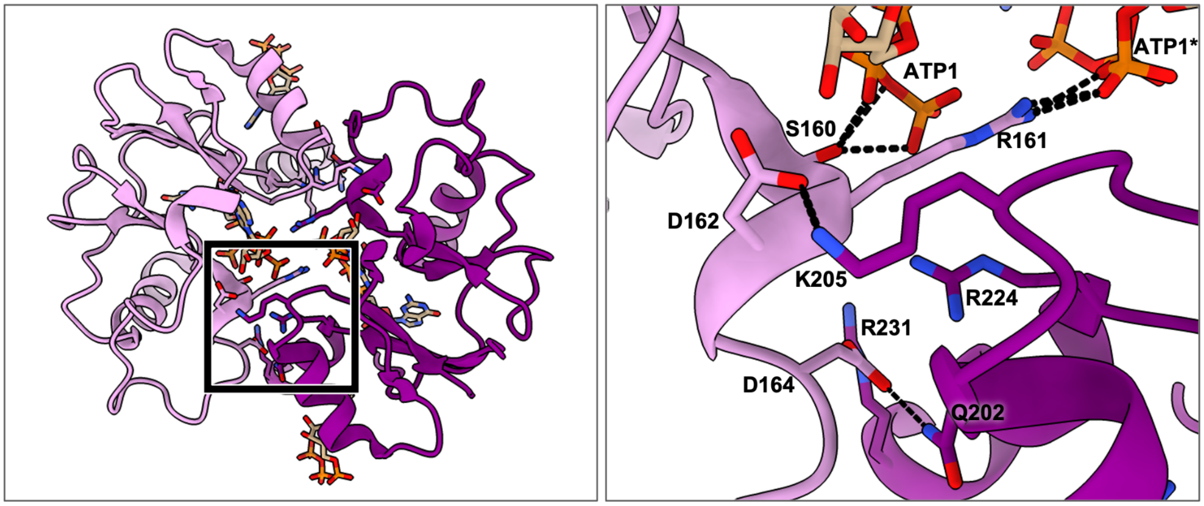

Contacts at the Bateman dimer interface in previously published structures of extended and compressed WT human IMPDH2 filaments.

Figure 3.2: Negative stain of WT and S160del with dinucleoside polyphosphates.

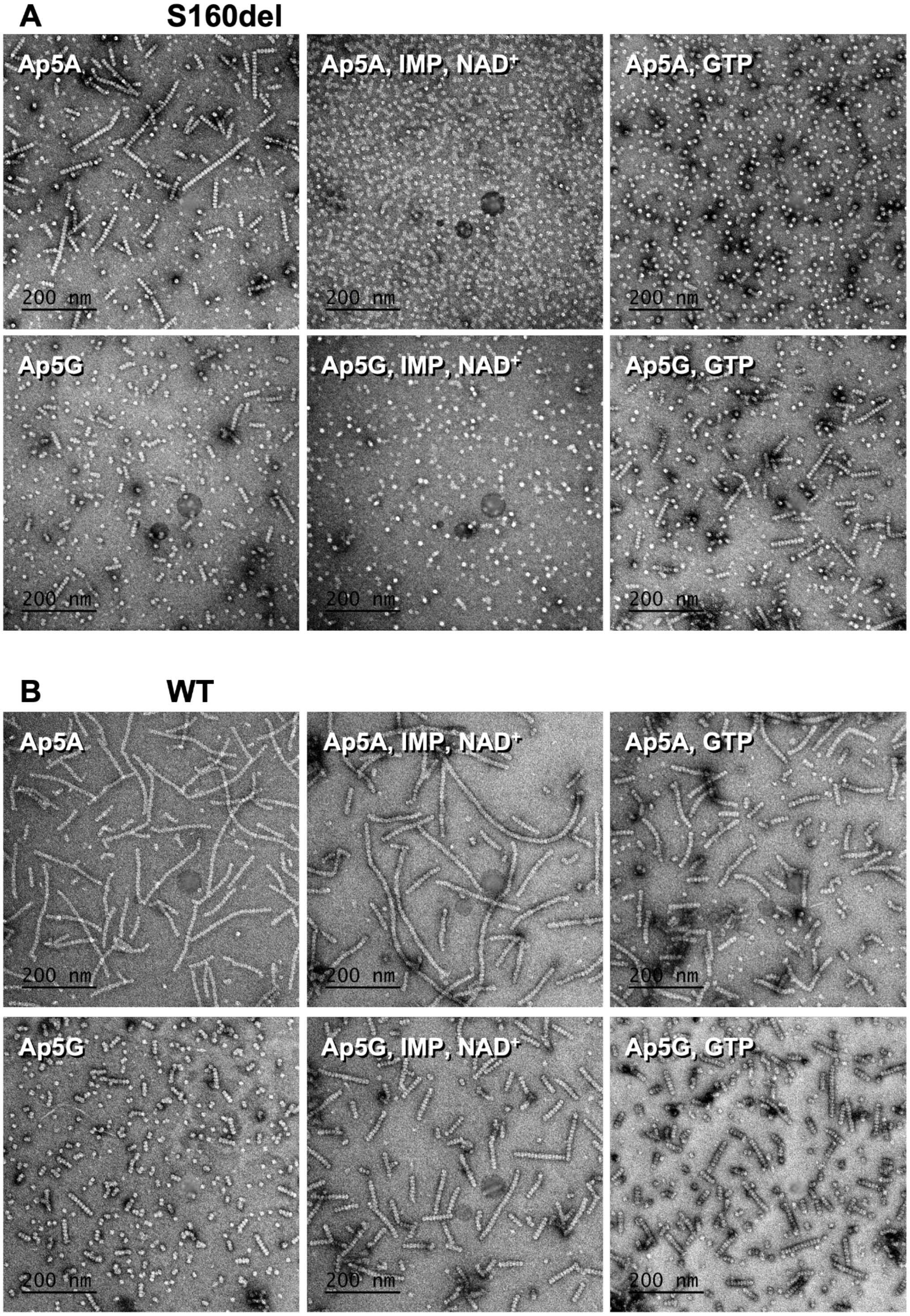

Representative negative stain images of 2 μM S160del (A) or WT (B) IMPDH2 with 1mM MgCl2 and indicated ligands. Final concentrations of ligands are: 1 mM Ap5A, 1 mM Ap5G, 3 mM IMP, 5 mM NAD⁺, and 20 mM GTP.

Figure 3.3: Ligand Binding restores polymerization, but not GTP regulation, to S160del.

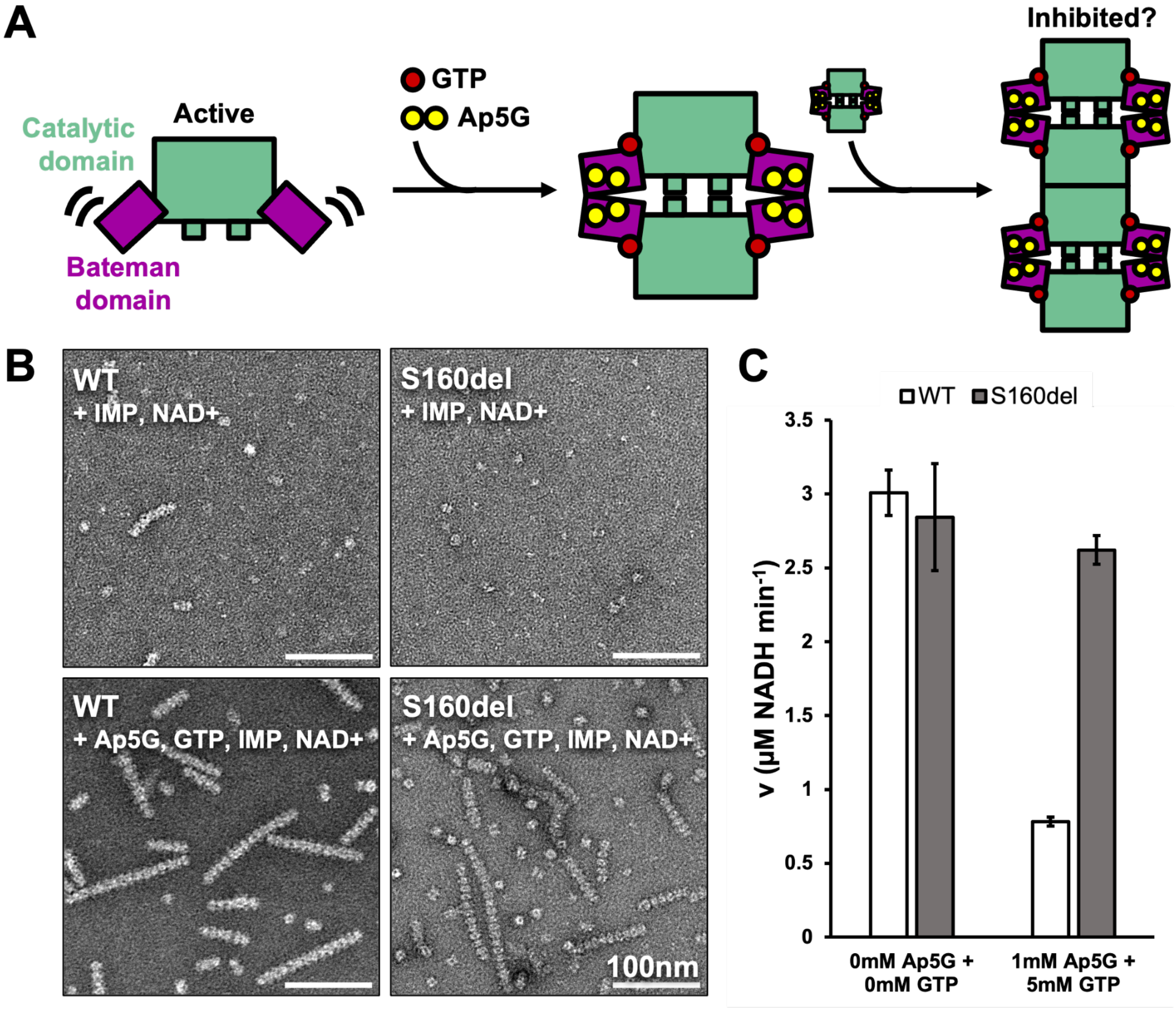

A. Experimental diagram. S160del IMPDH2 tetramers are active, and the regulatory Bateman domain (purple) is highly flexible. Ap5G and GTP bind to the Bateman domains of tetramers and stabilize the formation of canonical octamers and filaments.

B. Negative stain electron micrographs of WT and S160del hIMPDH2 in the assay conditions from panel C.

C. In vitro enzyme assay of WT and S160del hIMPDH2 in the absence (left) or presence (right) of Ap5G and GTP. Plotting the mean of three technical replicates. Error bars represent SD.

Figure 3.4: Activity assays with dinucleoside polyphosphates.

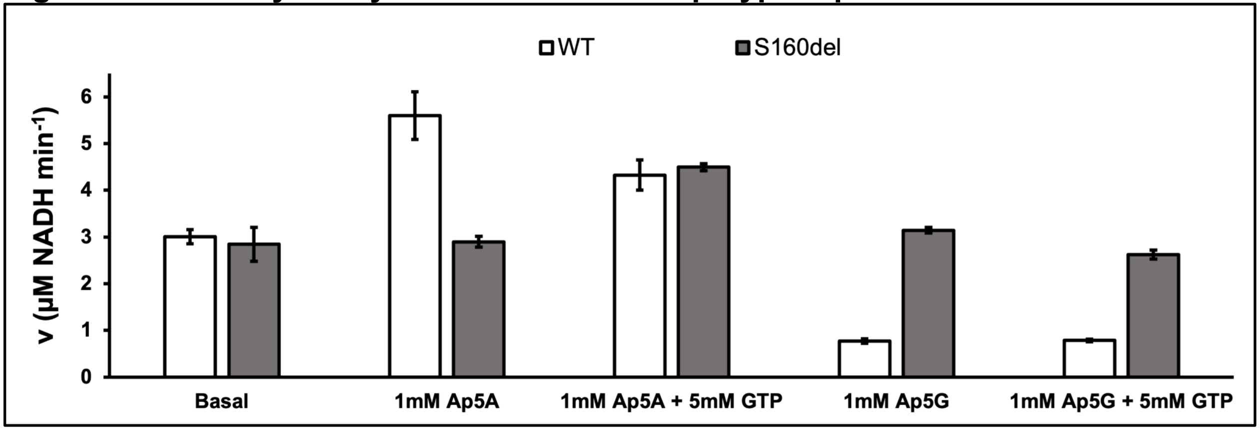

Each bar represents the average initial rate of three reactions. Error bars represent standard deviation for n = 3 technical replicates. Velocities were calculated from the change in absorbance at 340 nm. Reactions were initiated with 300 µM NAD+ and contained 1 µM enzyme, 1 mM IMP, 1 mM MgCl2, and additional nucleotides as indicated.

Figure 3.5: S160del and WT IMPDH2 filament segment structures with Ap5A.

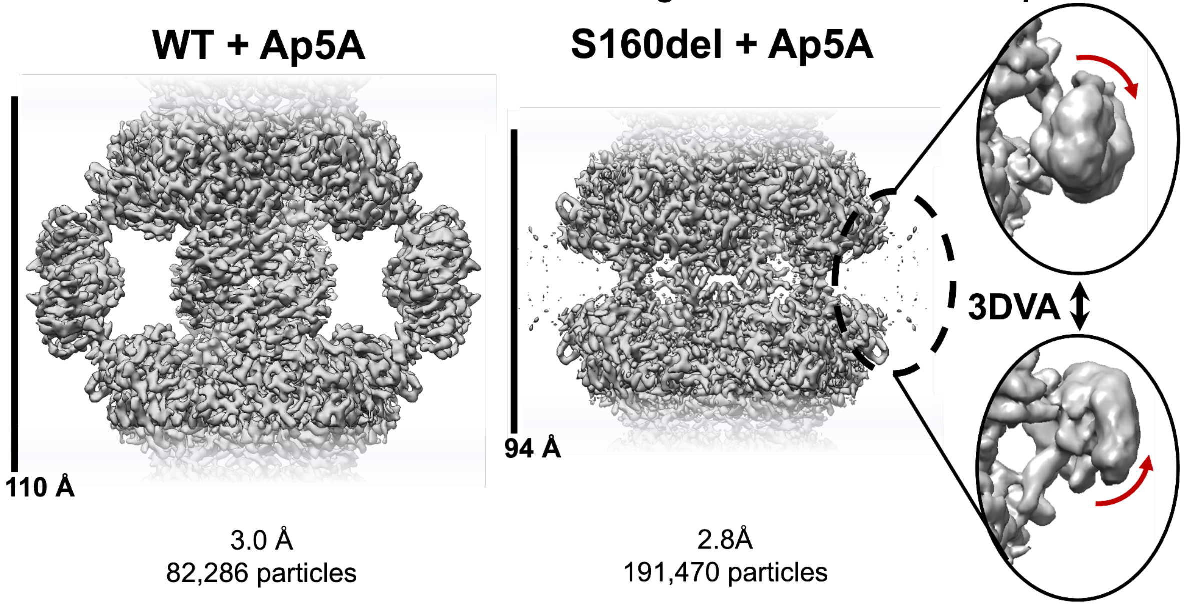

WT and S160del filament segment structures with Ap5A bound. The WT filament is extended, while S160del is compressed with a flexible Bateman domain, as visualized with 3D variability analysis in CryoSPARC.

Figure 3.6: S160del + Ap5A cryo-EM data processing workflow and FSC curve.

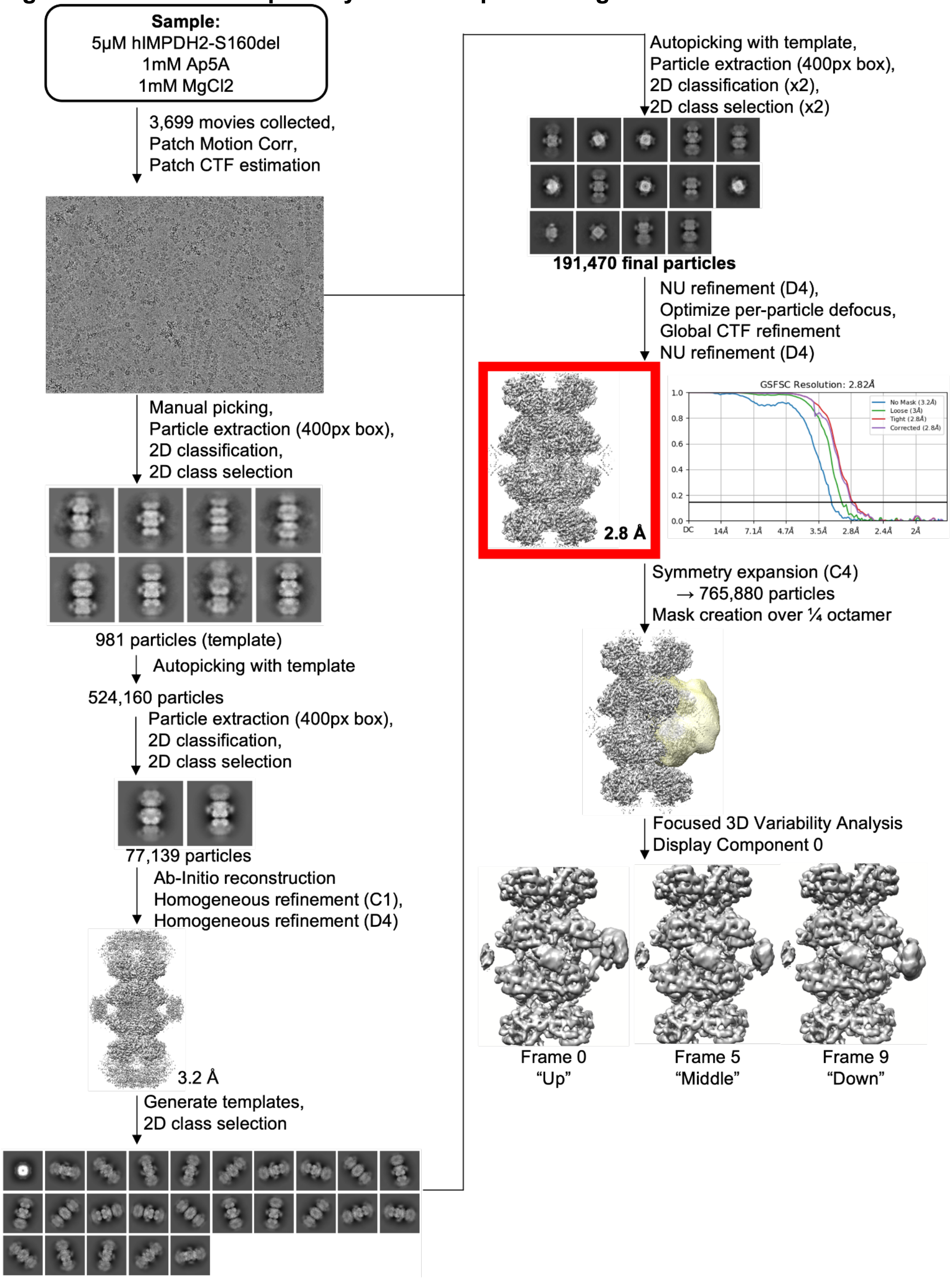

Figure 3.7: WT + Ap5A cryo-EM data processing workflow and FSC curve.

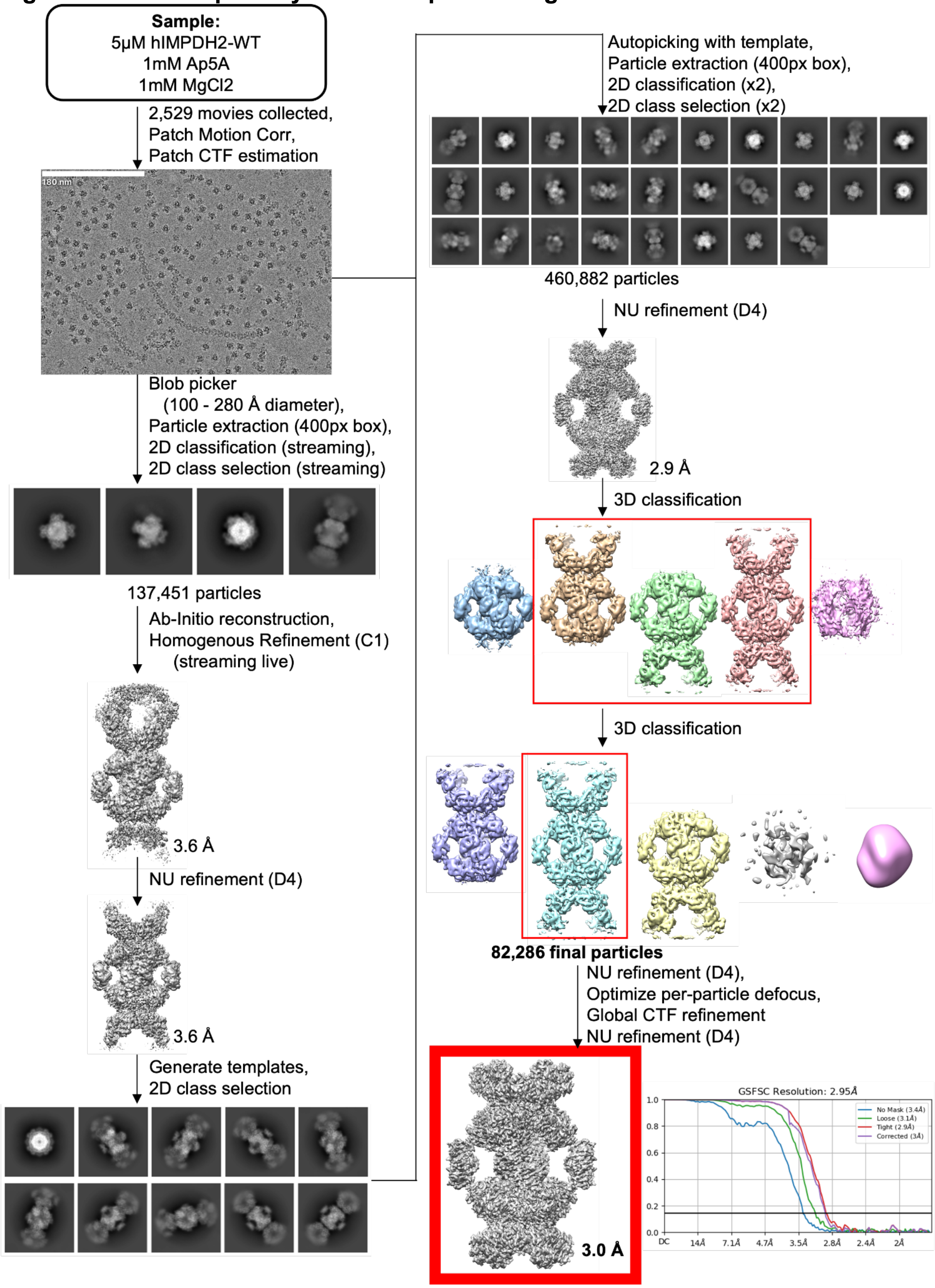

Figure 3.8: S160del and WT IMPDH2 filament segment structures with Ap5G and GTP.

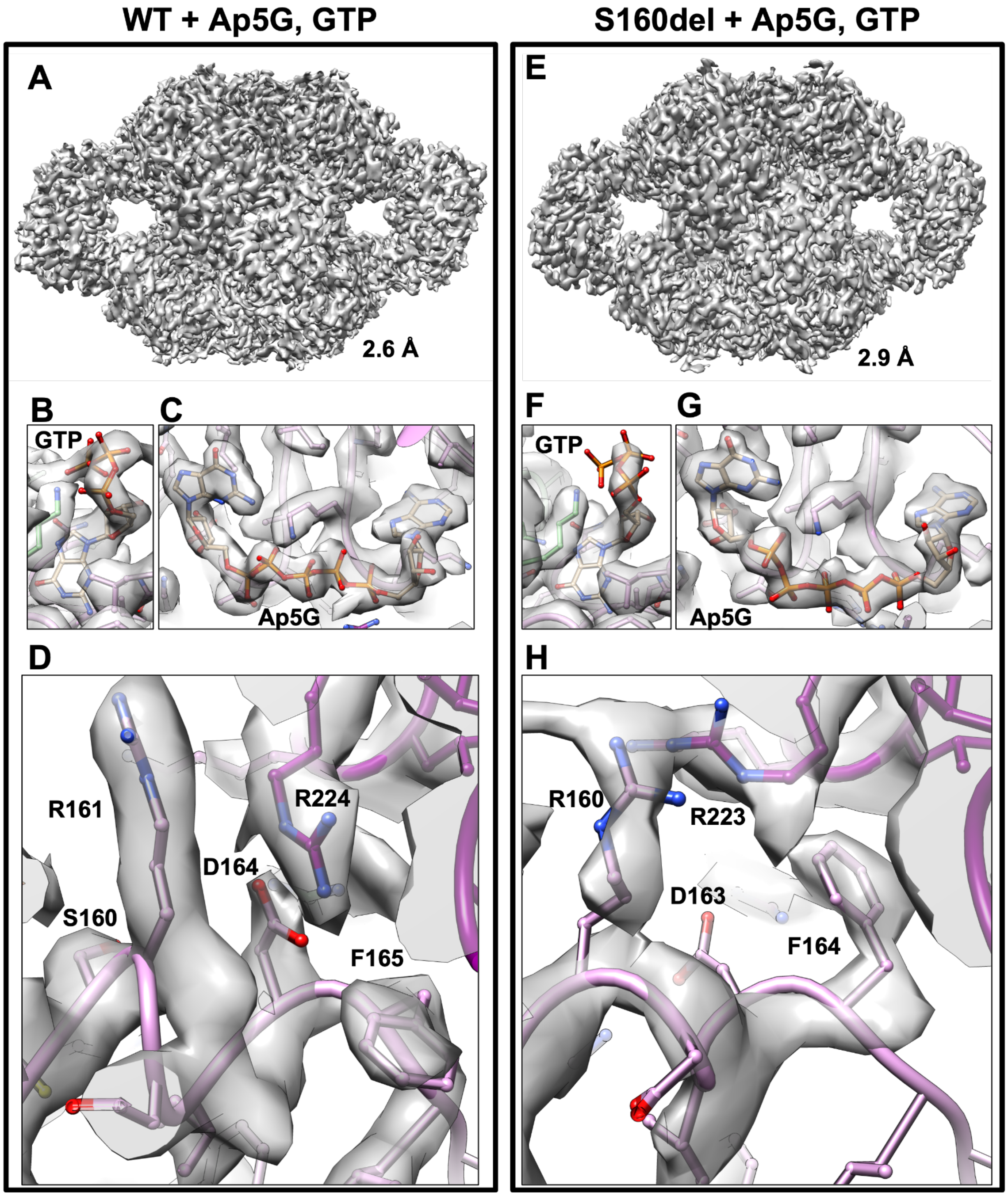

A. Final volume of WT filament segment with Ap5G and GTP bound.

B. Allosteric site 3 of WT structure, showing GTP bound.

C. Allosteric sites 1 and 2 of WT structure, showing Ap5G bound.

D. Bateman dimer interface of WT structure.

E. Final volume of S160del filament segment with Ap5G and GTP bound.

F. Allosteric site 3 of S160del structure, showing GTP bound.

G. Allosteric sites 1 and 2 of S160del structure, showing Ap5G bound.

H. Bateman dimer interface of S160del structure. The rotamer of F164 (F165 in the WT structure) is flipped, displacing R223 (R224 in the WT structure). D163 (D164 in the WT structure) is flipped away from R223 (R224 in the WT structure), preventing it from forming a salt bridge.

Figure 3.9: S160del + Ap5G, GTP cryo-EM data processing workflow and FSC curve.

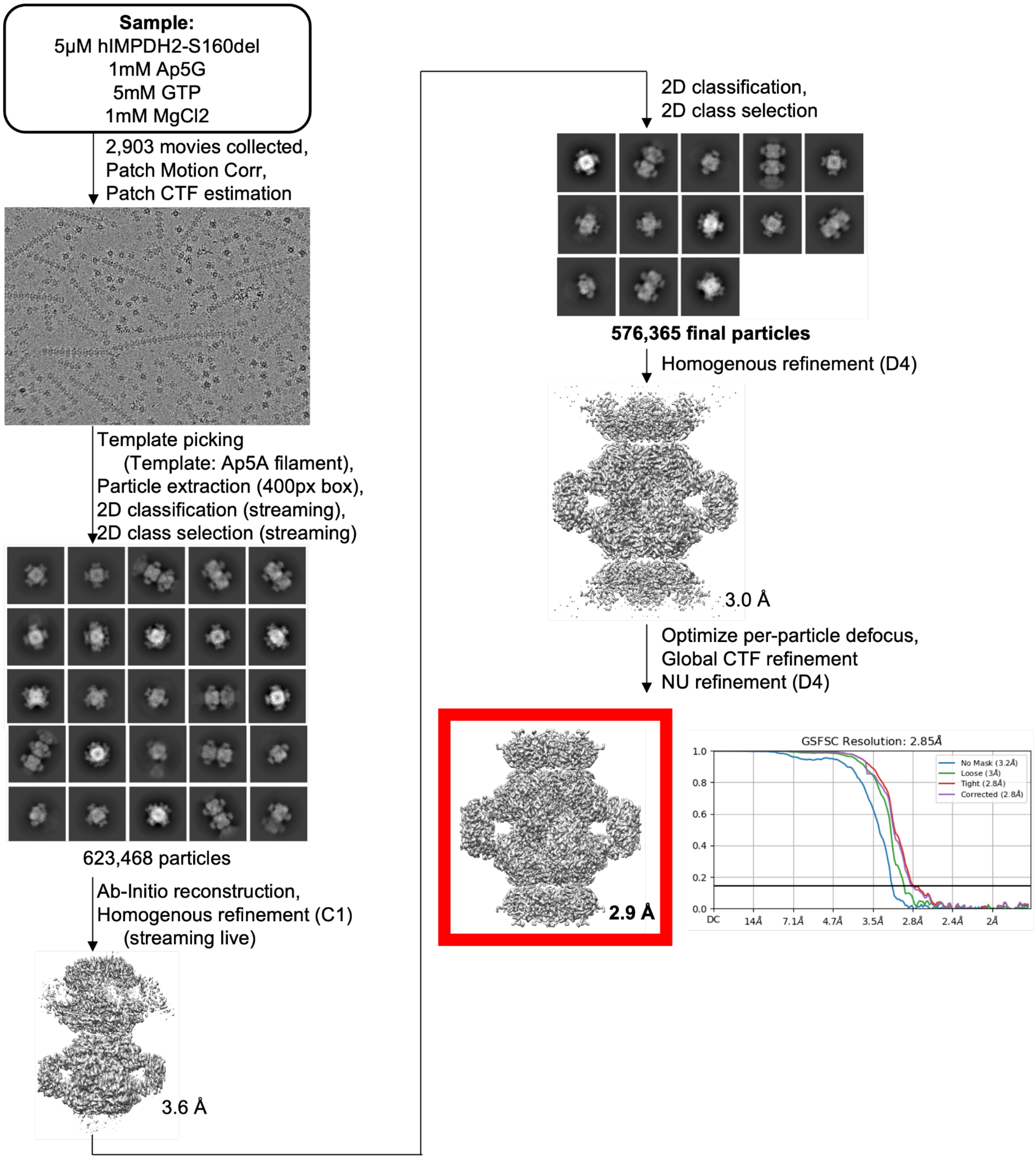

Figure 3.10: WT + Ap5G, GTP cryo-EM data processing workflow and FSC curve.

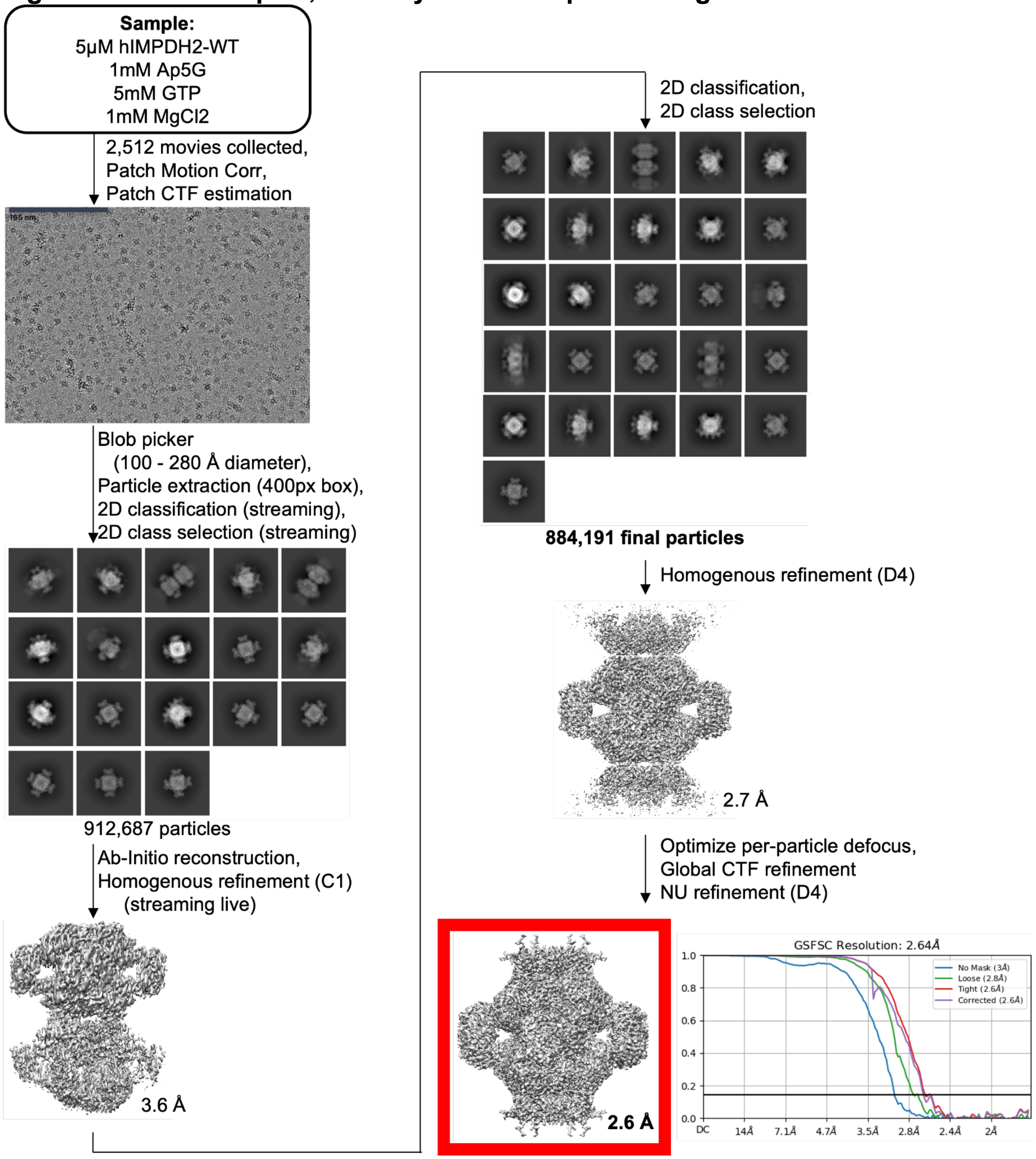

Figure 3.11: S160del + Ap5G, GTP, IMP, NAD⁺ filament segment structure.

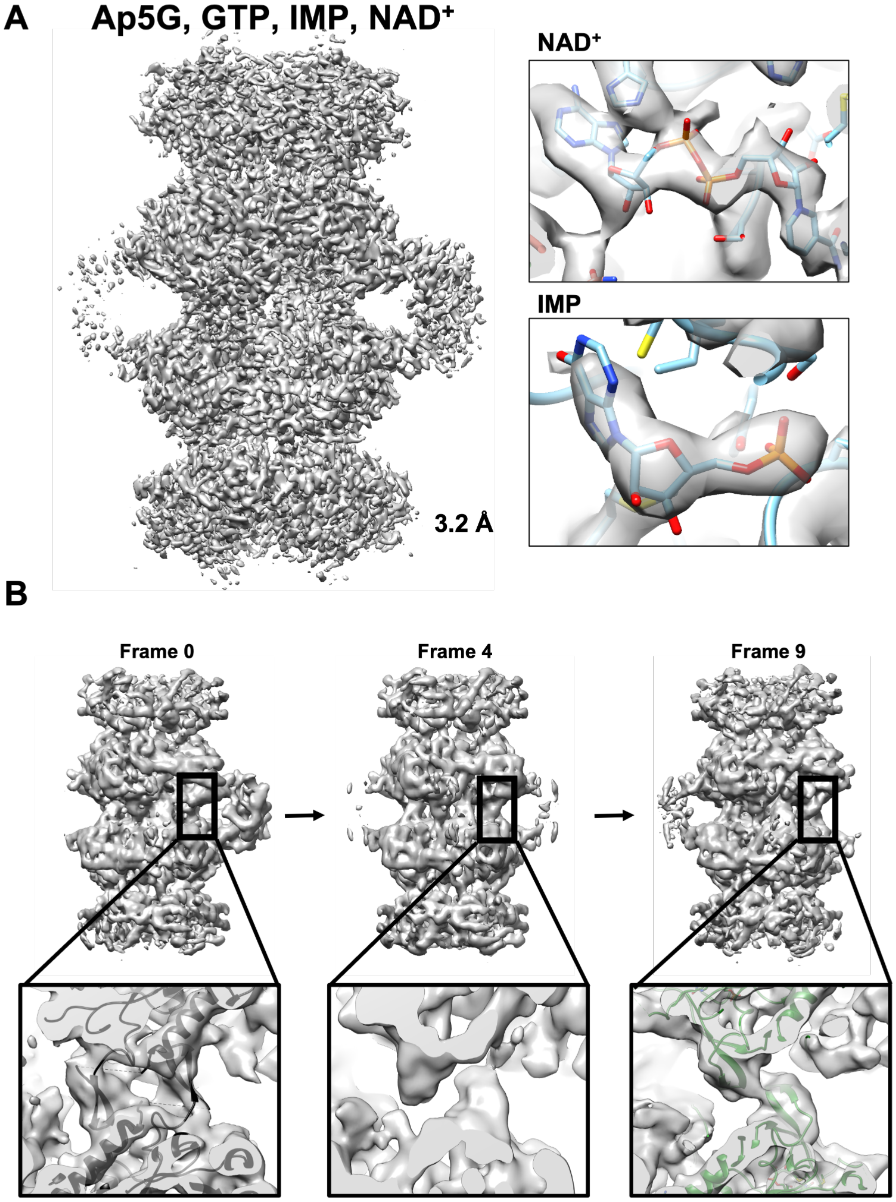

A. Volume of the filament segment structure of S160del with Ap5G, GTP, IMP, and NAD⁺ bound. The previously published compressed filament structure of WT IMPDH2 (6U9O) was rigid body fit into the best resolved volume, and density supporting IMP and NAD⁺ binding is shown.

B. Frames output from 3D variability analysis run on the S160del + Ap5G, GTP, IMP, NAD⁺ filament structure. For each frame, the entire reconstruction is shown above a focused view of the finger domains. The finger domain position in frame 0 agrees with the position of the S160del + Ap5G, GTP filament structure rigid-body fit into the volume (black ribbon). The finger domain position in frame 9 agrees with the position of the previously published, compressed WT filament (PDB: 6U9O), with individual chains rigid-body fit into the volume.

Figure 3.12: S160del + Ap5G, GTP, IMP, NAD⁺ cryo-EM data processing workflow and FSC curve.

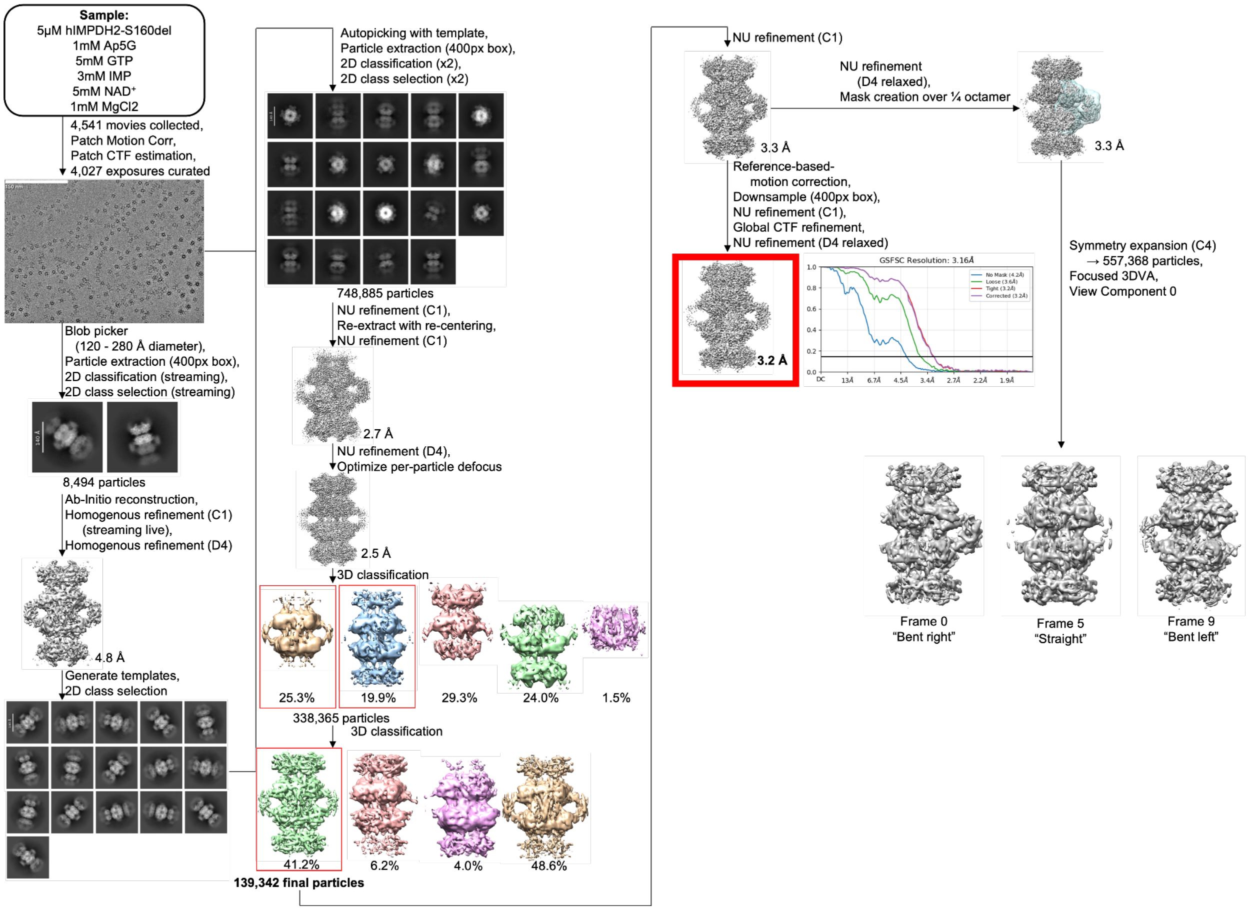

Figure 3.13: Comparison of G113E, WT, and S160del structures.

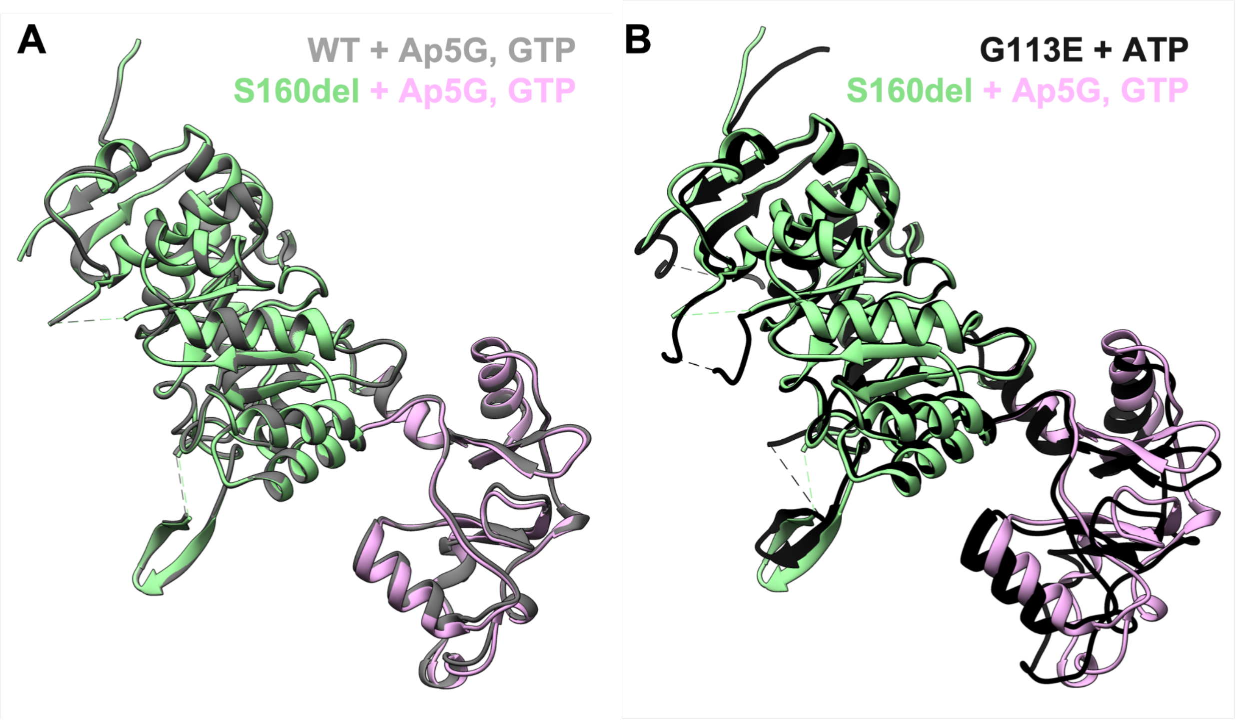

A. WT (gray) and S160del (green/pink) structures with Ap5G and GTP bound. Models are aligned at the catalytic domain (green). No significant differences in backbone are observed.

B. G113E + ATP (black) and S160del + Ap5G, GTP (green/pink) structures. Models are aligned at the catalytic domain (green). The position of the finger domains is comparable, but the Bateman domain of G113E is shifted closer towards the catalytic domain.

Table 3.1: Data collection and refinement statistics of S160del and WT cryo-EM structures with dinucleoside polyphosphates.

	hIMPDH2-S160del + Ap5A compressed filament segment	**hIMPDH2-WT + Ap5A extended filament segment**	**hIMPDH2-S160del + Ap5G, GTP compressed filament segment**	**hIMPDH2-WT + Ap5G, GTP compressed filament segment**	**hIMPDH2-S160del compressed filament segment with substrates**
Ligands	Ap5A	Ap5A	Ap5G, GTP	Ap5G, GTP	Ap5G, GTP, IMP, NAD+
Data collection and refinement					
Magnification	45,000	45,000	45,000	45,000	105,000
Voltage (kV)	200	200	200	200	300
Electron exposure (e^-/Å^2)	50	50	50	50	49
Nominal defocus range (μm)	-1.8 — -1.2	-1.8 — -1.2	-1.8 — -1.2	-1.8 — -1.2	-1.0 — -0.7
Pixel size (data collection) (Å)	0.885	0.4425	0.885	0.885	0.4215
Pixel size (reconstruction) (Å)	0.885	0.885	0.885	0.885	0.843
Micrographs (no.)	3,699	2,529	2,903	2,512	4,541
Initial particles (no.)	680,501	2,333,565	816,600	1,848,983	2,596,236
Final particles (no.)	191,470	82,286	576,365	884,191	139,342
Symmetry imposed	D4	D4	D4	D4	D4 (relaxed)
Resolution, CryoSPARC postprocess (0.143 FSC) (Å)	2.8	3.0	2.9	2.6	3.2
Model refinement and validation					
Initial model (PDB ID)	N/A	N/A	6UC2	(S160del + Ap5G, GTP)	N/A
R.m.s. deviations					
Bond lengths (Å)	N/A	N/A	0.0194	0.0202	N/A
Bond angles (°)	N/A	N/A	2.10	2.26	N/A
MolProbity score	N/A	N/A	1.78	1.23	N/A
Clashscore	N/A	N/A	4.23	1.10	N/A
C-beta deviations	N/A	N/A	23	25	N/A
Rotamer outliers (%)	N/A	N/A	3.69%	3.50%	N/A
Ramachandran plot					
Favored (%)	N/A	N/A	97.20%	98.28%	N/A
Allowed (%)	N/A	N/A	2.27%	1.72%	N/A
Disallowed (%)	N/A	N/A	0.53%	0.00%	N/A

Chapter 4. S160del expression in *Xenopus tropicalis* results in metabolic, neuromuscular, and filament-assembly defects

Adapted from:

O'Neill, A. G., McCartney, M. E., Wheeler, G. M., Patel, J. H., Sanchez-Ramirez, G., Kollman, J. M., & Wills, A. E. (2025). An IMPDH2 variant associated with neurodevelopmental disorder disrupts purine biosynthesis and somitogenesis. bioRxiv, 2025-05.

4.1 Overexpression of S160del in *Xenopus tropicalis.*

Previous studies on enzymes in the purine biosynthetic pathways have used *Xenopus laevis* to gain insight into neuromuscular phenotypes caused by imbalanced purine pools during embryonic development, motivating our present study (75). *Xenopus* is also a convenient vertebrate system for *in situ* imaging of large macrostructures using immunostaining, making it amenable to our study of IMPDH filaments. With human IMPDH2 sharing 93% amino acid sequence identity with *Xenopus tropicalis* IMPDH2 (Fig. 4.1), *Xenopus tropicalis* is therefore a useful animal model to study the effects of IMPDH2 mutants on both neurodevelopment and the formation of filament macrostructures *in vivo*, bridging the gap between *in vitro* work and disease phenotypes.

Because all patients were heterozygous for these IMPDH2 variants (Table 1.1), we hypothesized that the mutants would exert a dominant effect on early development (44). We therefore sought to interrogate the effects of adding S160del to the endogenous functions of IMPDH2 *in vivo*. To test this, we overexpressed WT and S160del human IMPDH2 (hIMPDH2) in *Xenopus tropicalis* embryos. We synthesized mRNA transcripts encoding WT or S160del hIMPDH2 (Fig. 4.2) and injected this mRNA into both cells at the 2-cell stage (Fig. 4.3C). Western blots of whole embryo lysates at stage 21, approximately 1 day post fertilization (dpf), confirmed dose-dependent overexpression of the injected mRNA compared to uninjected controls (Fig. 4.3D, 4.4). We detected the persistence of overexpressed IMPDH2 via western blot up to stage 47, approximately 5 dpf, for the 1000 pg dose of mRNA (Fig. 4.5).

4.2 S160del disrupts purine metabolism *in vivo.*

We then investigated the mutant's effect on metabolism in the developing tadpole through liquid chromatography-mass spectrometry (LC-MS) of whole tadpole lysates, collected at stage 41, approximately 3 dpf. Our previous *in vitro* characterization of S160del led us to propose that its insensitivity to feedback inhibition would result in a gain-of-function effect *in vivo*. We hypothesized that expression of this mutant would result in increased pools of guanine nucleotides over adenine nucleotides in purine biosynthesis (Fig. 4.3B). Strikingly, we found that while WT-expressing tadpoles had no significant difference in metabolite levels compared to uninjected tadpoles, the metabolic profile of S160del-expressing tadpoles had significantly shifted (Fig. 4.6, 4.7).

The downstream metabolites XMP, GMP, guanine, guanosine, and xanthosine were significantly elevated (Fig. 4.3F-G, 4.8). Conversely, IMP and AMP levels were decreased in the S160del group (Fig. 4.3E, H). The S160del group also had elevated levels of urate, a product of purine nucleotide degradation (Fig. 4.8). These findings demonstrate that S160del specifically disrupts the physiological abundance of purine nucleotides, supporting the hypothesis that the gain-of-function effect of S160del impacts relevant metabolite levels.

4.3 S160del expression affects early *Xenopus tropicalis* development.

After establishing that S160del expression affects metabolism in an animal model, we sought to understand its impact on early development. We began with behavioral and morphological characterization of tadpoles expressing S160del. At stage 41, tadpoles expressing WT or S160del hIMPDH2, as well as uninjected controls, were tested for their ability to swim away from physical stimulus with a blinded escape reflex assay (76). Tadpoles expressing S160del were significantly less responsive than the dose-matched WT groups and the uninjected controls (Fig. 4.3J). They also twitched spontaneously, without any external stimulus (Fig. 4.3K). Following behavioral scoring, tadpoles were fixed and imaged on a stereomicroscope for morphological phenotyping and measurements of tail curvature (77). Both groups expressing S160del were significantly shorter (Fig. 4.9) and had significantly more ventrally curved tails, compared to the dose-matched WT groups and the uninjected controls (Fig. 4.3I, 4.3L). Notably, tadpoles injected with 1000 pg of hIMPDH2-WT mRNA were also shorter than the uninjected controls (Fig. 4.9). However, the ventral tail curvature and the twitching behavior cannot be attributed to overexpression of hIMPDH2, as the controls overexpressing WT hIMPDH2 at similar levels were indistinguishable from uninjected controls with endogenous IMPDH2 levels. These phenotypes resemble patient symptoms of hyperkinetic movements and abnormal posturing and suggest that expression of S160del in a vertebrate system specifically results in morphological and neurobehavioral defects during development.

4.4 Somite boundaries are disorganized in tadpoles expressing S160del.

The motor defects and tail morphology in S160del-expressing tadpoles led us to hypothesize that there were underlying defects in either muscle or neuronal development. To assess tissue-specific defects in the developing tadpoles, we performed immunostaining of neurofilament and skeletal muscle on fixed tadpoles at stage 41. From the neurofilament staining, tadpoles expressing S160del had a significantly lower density of intersomitic axon bundles along the length of the tail, and organization of the remaining axons was disrupted (Fig. 4.10B, D). Notably, the WT-injected group had a slightly higher number of axon bundles per millimeter as compared to the uninjected controls (Fig. 4.10D). From the skeletal muscle staining, there was also a clear defect in the number and clarity of somite boundaries, with poorly defined or indistinguishable somite boundaries in tadpoles expressing S160del (Fig. 4.10C, E). Taken together, these results suggest a defect in both myogenesis and intersomitic neuron distribution resulting from S160del expression, resembling the hypotonia of patients.

4.5 S160del has a dominant negative effect on IMPDH assembly *in vivo*.

To understand how S160del might exert a dominant effect, we sought to determine whether it might disrupt one of the key properties of IMPDH2: its ability to form rod and ring filament structures. We previously described the formation of rods and rings in the developing tadpole under metabolic challenges, including tail regeneration and treatment with the IMPDH inhibitor mycophenolic acid (MPA) (78). In wildtype, uninjected tadpoles, IMPDH2 expression was primarily diffuse in the axial skeletal muscle when observed via immunostaining (Fig. 4.11E). However, upon MPA treatment, we observed robust rod and ring formation from endogenous IMPDH2, particularly along the boundaries of the somitic muscles (Fig. 4.11B). Similarly, tadpoles expressing WT hIMPDH2 formed rods and rings in response to MPA treatment. Notably, even without MPA treatment, some rods and rings were present in WT hIMPDH2-expressing tadpoles, presumably due to the effects of overexpression (Fig. 4.11C, 4.11F). Overexpression of IMPDH has been reported to induce in rods and rings in previous cell culture studies (13, 79, 80).

In contrast to uninjected and WT-injected tadpoles, tadpoles expressing S160del hIMPDH2 exhibited a dominant-negative loss of rod and ring formation under MPA treatment, with fewer structures observed (Fig. 4.11D, 4.11G). This data indicates that the structural phenotype we have observed *in vitro* for S160del translates to a defect in rod and ring formation in the cells of a vertebrate system. S160del is likely able to co-assemble with endogenous IMPDH into heterooligomers, preventing endogenous IMPDH filament assembly.

4.6 Discussion.

Errors in purine and pyrimidine metabolism result in a variety of disorders affecting neuromuscular development, including dystonia (81, 82). Both gain-of-function and loss-of-function mutations have been documented in purine-related developmental disorders, sometimes affecting the same enzyme. Such is the case for phosphoribosylpyrophosphate synthetase (PRPS), a regulatory enzyme upstream of IMPDH in purine biosynthesis, where mutations that decrease activity lead to hearing and vision loss, muscle weakness, and intellectual disability; mutations that increase PRPS activity lead to gout and progressive renal failure. The more severe, early-onset phenotype of PRPS superactivity also includes symptoms similar to those resulting from PRPS deficiency, such as hypotonia and developmental delay (82). This suggests that a delicate balance between metabolites in these pathways is essential for proper functioning of nerves and muscle, and disrupting that balance in either direction can have deleterious consequences on neuromuscular development, sometimes even leading to overlapping clinical presentations.

The gout caused by PRPS superactivity is a result of overproduction of uric acid, the final degradation product of purine nucleotides (83). Build-up of guanine and hypoxanthine, and subsequent overproduction of uric acid, is characteristic of congenital HPRT deficiency, which results in increased flux through *de novo* purine biosynthesis rather than the salvage pathway (56, 84, 85). Metabolites like urate and guanine can therefore be useful biomarkers for diagnosing these disorders.

Recently, *Xenopus laevis* was used as a model to study the role of purine biosynthesis in embryonic development (75). Their study focused on the role of adenylosuccinate lyase (ADSL), an enzyme which functions both up- and down-stream of IMPDH in the *de novo* purine biosynthesis pathway. ADSL deficiency in humans also causes developmental delay, autism, epilepsy, and hyperkinetic movements. Knockdown of ADSL in *Xenopus laevis* leads to defects in somitogenesis and hypaxial muscle formation, likely through disrupting the balance of purine nucleotide pools. Knockdown of other purine biosynthetic enzymes, hypoxanthine phosphoribosyltransferase (HPRT) and phosphoribosyl pyrophosphate amido transferase (PPAT) likewise led to the same myogenic defects in tadpoles, and mirrored the hypotonia seen in patients (75).

Here, we show that expressing the gain-of-function IMPDH2 variant S160del in *Xenopus tropicalis* resulted in significantly elevated levels of GMP, guanine, and urate, supporting our hypothesis that the IMPDH2 hyperactivity we characterized *in vitro* would affect metabolite levels *in vivo*. In addition, we demonstrated that the S160del mutant, which we previously showed is incapable of forming filaments *in vitro*, has a dominant negative effect on the ability of IMPDH to assemble into rod and ring shaped superstructures *in vivo*. The expression of this hyperactive variant also resulted in behavioral and morphological defects in the developing tadpole, including ventral tail curvature and twitching. Immunostaining of the tail revealed a disorganization of muscle patterning in the trunk, with poorly defined or indistinguishable somite boundaries and disorganized innervation of axon bundles in between somites. These data suggest that disrupted purine pools resulting from S160del hyperactivity may be affecting somitogenesis, and that the hypotonia and hyperkinetic movements similar to those observed in patients can be recapitulated in a *Xenopus* model. Future studies may investigate if these metabolomic signatures and tissue-level phenotypes hold in patients.

This work establishes a model for studying the consequences of IMPDH2 dysregulation in a vertebrate system, interrogating the embryonic origin of the disease in parallel with metabolism and enzyme behavior. The gain-of-function S160del variant impairs neuromuscular development and IMPDH filament formation in a dominant fashion and significantly affects purine metabolite levels. Strikingly, overexpression of WT hIMPDH2 did not result in these defects in the developing tadpole, supporting the hypothesis that normal guanine nucleotide levels are sufficient to inhibit the WT enzyme despite overexpression. We conclude that dysregulation of IMPDH2 is likely the main driver of disease in S160del patients, rather than changes in overall IMPDH protein levels. Future work may focus on using this system to test IMPDH inhibitors as potential therapeutics for disorders related to IMPDH2 hyperactivity.

Figure 4.1: Amino acid sequence alignment of human and *Xenopus tropicalis* IMPDH2.

```
                        Catalytic Domain
sp|P12268|IMDH2_HUMAN   MADYLISGGTSYVPDDGLTAQQLFNCGDGLTYNDFLILPGYIDFTADQVDLTSALTKKIT   60
sp|F7CYY5|IMDH2_XENTR   MADYLISGGTSYVPDDGLTAQQLFGAGDGLTYNDFLILPGYIDFTADQVDLTSALTKKIT   60
                        ************************..**********************************

sp|P12268|IMDH2_HUMAN   LKTPLVSSPMDTVTEAGMAIAMALTGGIGFIHHNCTPEFQANEVRKVKKYEQGFITDPVV   120
sp|F7CYY5|IMDH2_XENTR   LKTPMVSSPMDTVTEASMAIAMALTGGIGIMHHNCTPEFQANEVRKVKKYEQGFITDPVV   120
                        ****:***********.************::*****************************
                        Regulatory Domain                                 160
sp|P12268|IMDH2_HUMAN   LSPKDRVRDVFEAKARHGFCGIPITDTGRMGSRLVGIISSRDIDFLKEEEHDCFLEEIMT   180
sp|F7CYY5|IMDH2_XENTR   LSPKHRVRDVFEAKARHGFCGIPITENGKMGSKLAGIISSRDIDFLKSEEHDLALSEIMT   180
                        ****.********************:.*:***:*.*************.****  *.****

sp|P12268|IMDH2_HUMAN   KREDLVVAPAGITLKEANEILQRSKKGK-LPIVNEDDELVAIIARTDLKKNRDYPLASKD   239
sp|F7CYY5|IMDH2_XENTR   RREDLVVAPAGVTLKEANEILQRSKKGKLLPIVNGNDELVAIIARTDLKKNRDYPLASKD   240
                        :**********:**************** ***** :************************

sp|P12268|IMDH2_HUMAN   AKKQLLCGAAIGTHEDDKYRLDLLAQAGVDVVVLDSSQGNSIFQINMIKYIKDKYPNLQV   299
sp|F7CYY5|IMDH2_XENTR   AKKQLLCGAAIGTHEDDKYRLDLLVQAGVDAVVLDSSQGNSIFQINMIKFIKEKYQDLQV   300
                        ************************.*****.******************:**:** :***

sp|P12268|IMDH2_HUMAN   IGGNVVTAAQAKNLIDAGVDALRVGMGSGSICITQEVLACGRPQATAVYKVSEYARRFGV   359
sp|F7CYY5|IMDH2_XENTR   IAGNVVTAAQAKNLIDAGADALRVGMGSGSICITQEVLACGRPQATAVYKVSEYARRFGV   360
                        *.****************.*****************************************

sp|P12268|IMDH2_HUMAN   PVIADGGIQNVGHIAKALALGASTVMMGSLLAATTEAPGEYFFSDGIRLKKYRGMGSLDA   419
sp|F7CYY5|IMDH2_XENTR   PVIADGGIQTVGHIAKALALGASTVMMGSLLAATTEAPGEYFFSDGIRLKKYRGMGSLDA   420
                        *********.**************************************************

sp|P12268|IMDH2_HUMAN   MDKHLSSQNRYFSEADKIKVAQGVSGAVQDKGSIHKFVPYLIAGIQHSCQDIGAKSLTQV   479
sp|F7CYY5|IMDH2_XENTR   MDKNVSSQKRYFSEADKIKVAQGVSGAVQDKGSIHKFIPYLIAGIQHSCQDIGAKSLTQV   480
                        ***::***:****************************:**********************

sp|P12268|IMDH2_HUMAN   RAMMYSGELKFEKRTSSAQVEGGVHSLHSYEKRLF              514
sp|F7CYY5|IMDH2_XENTR   RAMMYSGELKFEKRTMSAQVEGGVHGLHSYEKRLF              515
                        *************** *********.*********
```

Protein sequence alignment of human and Xenopus tropicalis IMPDH2 generated with Clustal O (1.2.4) MSA. Green color represents the catalytic domain and purple color represents the regulatory Bateman domain. The conserved serine residue 160 is highlighted.

Figure 4.2: In vitro synthesis of hIMPDH2 mRNA.

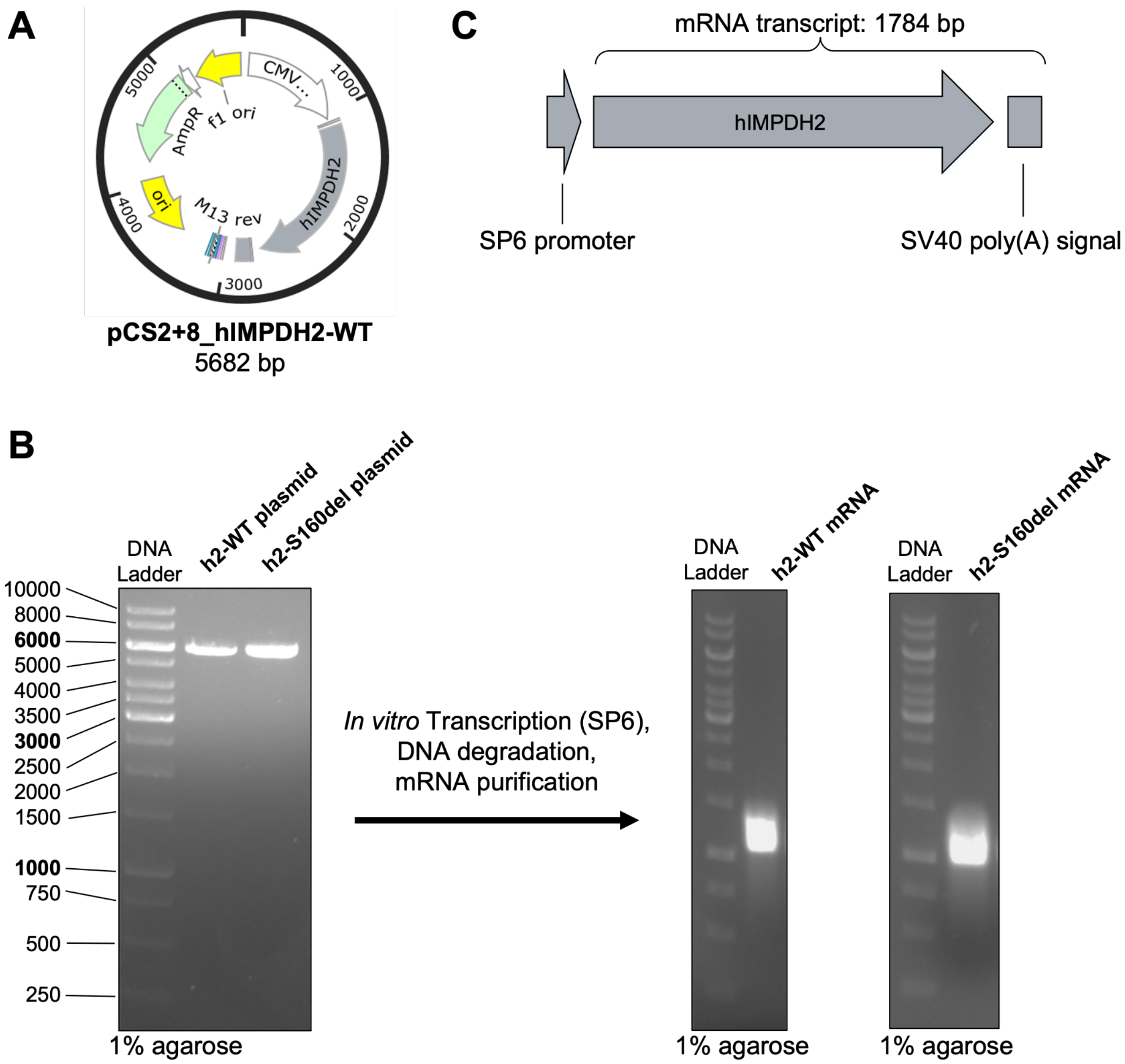

A. Plasmid map encoding hIMPDH2 in the pCS2+8 backbone vector.

B. hIMPDH2 coding region is under control of the SP6 promoter and followed by a poly(A) signal. The expected mRNA transcript size is 1784 bp.

C. Agarose gel of linearized plasmid DNA.

D. Agarose gel of the final mRNA product for WT and S160del hIMPDH2.

Figure 4.3: Overexpression of human IMPDH2 in Xenopus tropicalis.

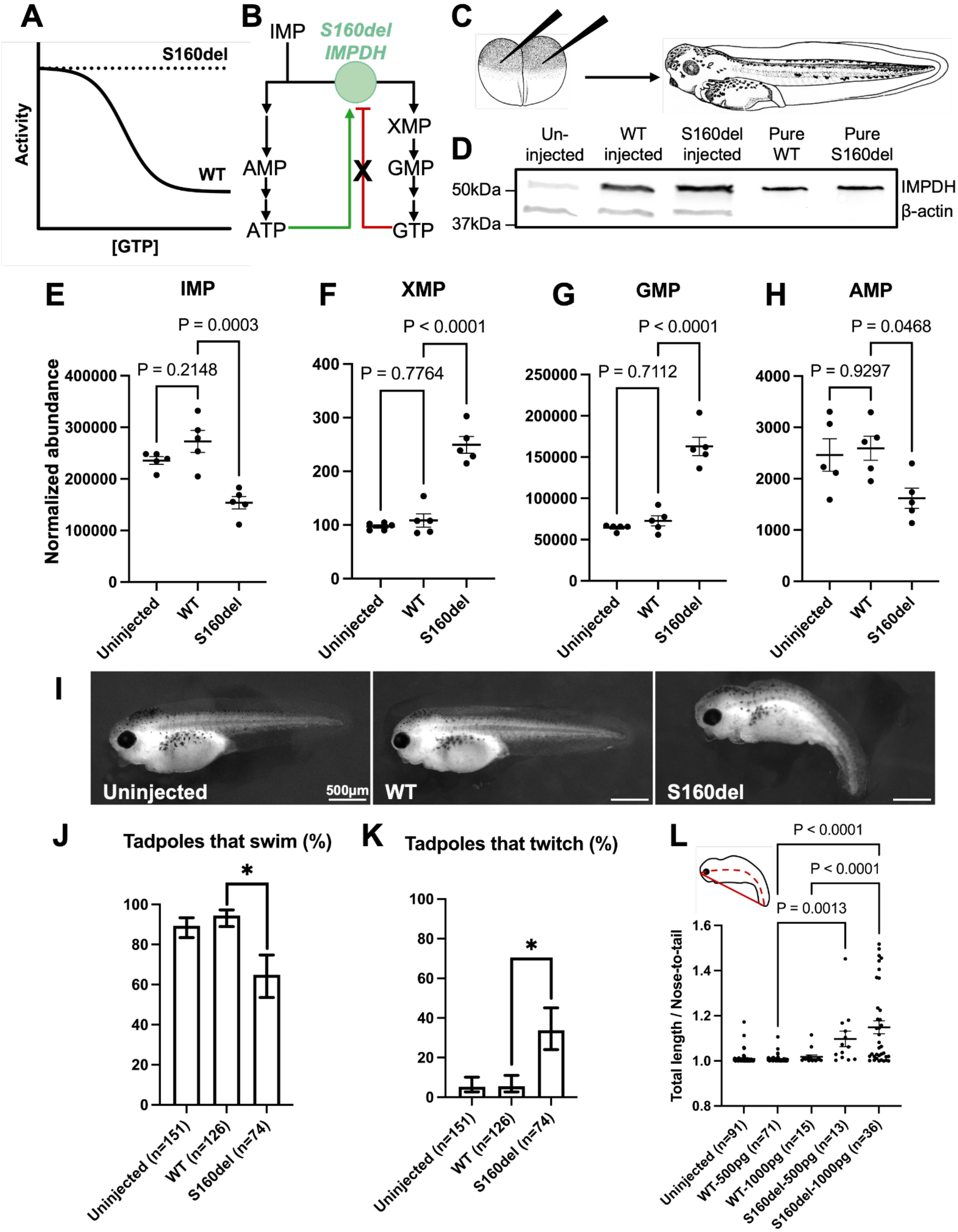

A. Representative plot of IMPDH2 activity under increasing concentrations of GTP for WT and S160del hIMPDH2.

B. Schematic diagram of de novo purine synthesis. The S160del mutation disrupts normal allosteric feedback inhibition by GTP, represented as a black (X) in the diagram.

C. Experimental diagram. Xenopus tropicalis embryos are injected with mRNA into each cell at the 2-cell stage and then raised to NF stage 41 for phenotype and metabolic assay. Drawings from Nieuwkoop and Faber (1994) Normal Table of Xenopus laevis (Daudin). Garland Publishing Inc, New York ISBN 0-8153-1896-0. Copyright © 1994 Pieter D. Nieuwkoop and J. Faber. Digital images created by and accessed from XenBase.

D. Representative western blot analysis of overexpression of hIMPDH2 in Xenopus tropicalis embryos at NF stage 21, following mRNA injection.

E-H. Quantification of selected purine synthesis metabolites from LC-MS assay. Each data point represents normalized metabolite abundance of an aggregate tissue sample composed of 10 whole tadpoles. One-way ANOVA and Tukey's multiple comparisons test performed on metabolite levels normalized to total protein from BCA. Plotting mean +/- SEM.

I. Photographs of NF stage 41 tadpoles following injection with the indicated mRNA.

J and K. Quantification of behavior effects of IMPDH2 overexpression. Plotting percentage +/- the 95% confidence interval of the proportion, calculated using the Wilson/Brown method. Chi-square analysis indicated significance. The Marasculio procedure was used to determine if WT and S160del groups were significantly different, at P=0.05.

L. Quantification of ventral tail curvature. One-way ANOVA and Tukey's multiple comparisons test. Plotting mean +/- SEM.

Figure 4.4: Dose-dependent overexpression of hIMPDH2 mRNA.

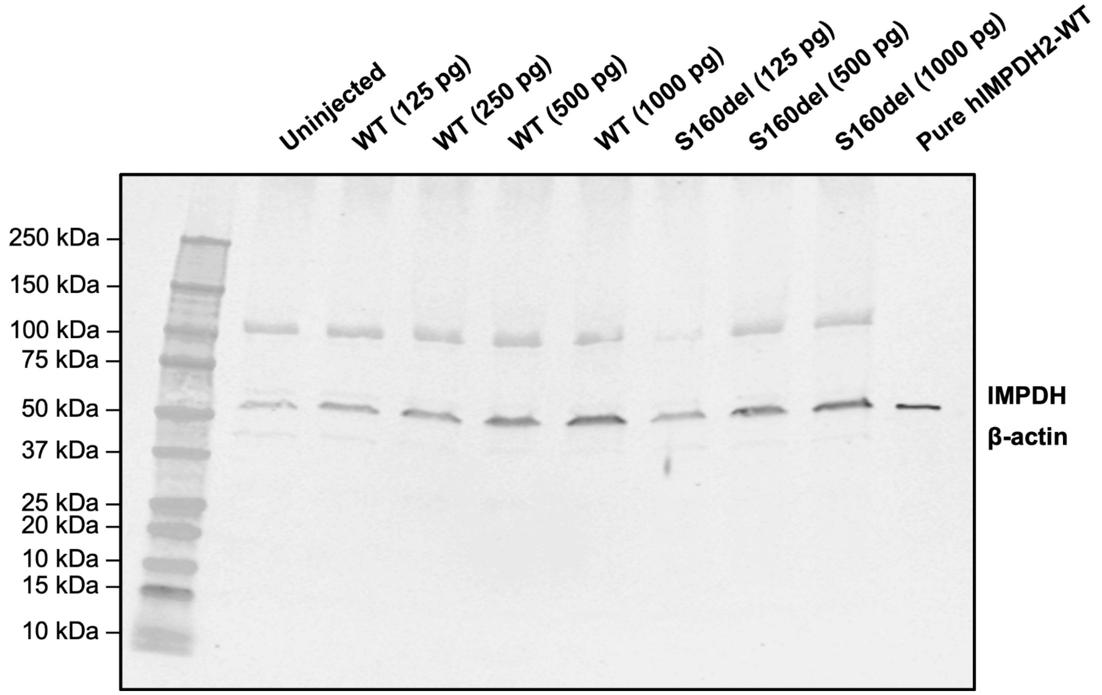

Representative western blot analysis of the mRNA dose response on hIMPDH2 protein expression in Xenopus embryos at NF stage 21, approximately 1 dpf. Trend was seen across two independent experiments.

Figure 4.5: Time-course western blot of tadpoles injected with S160del mRNA.

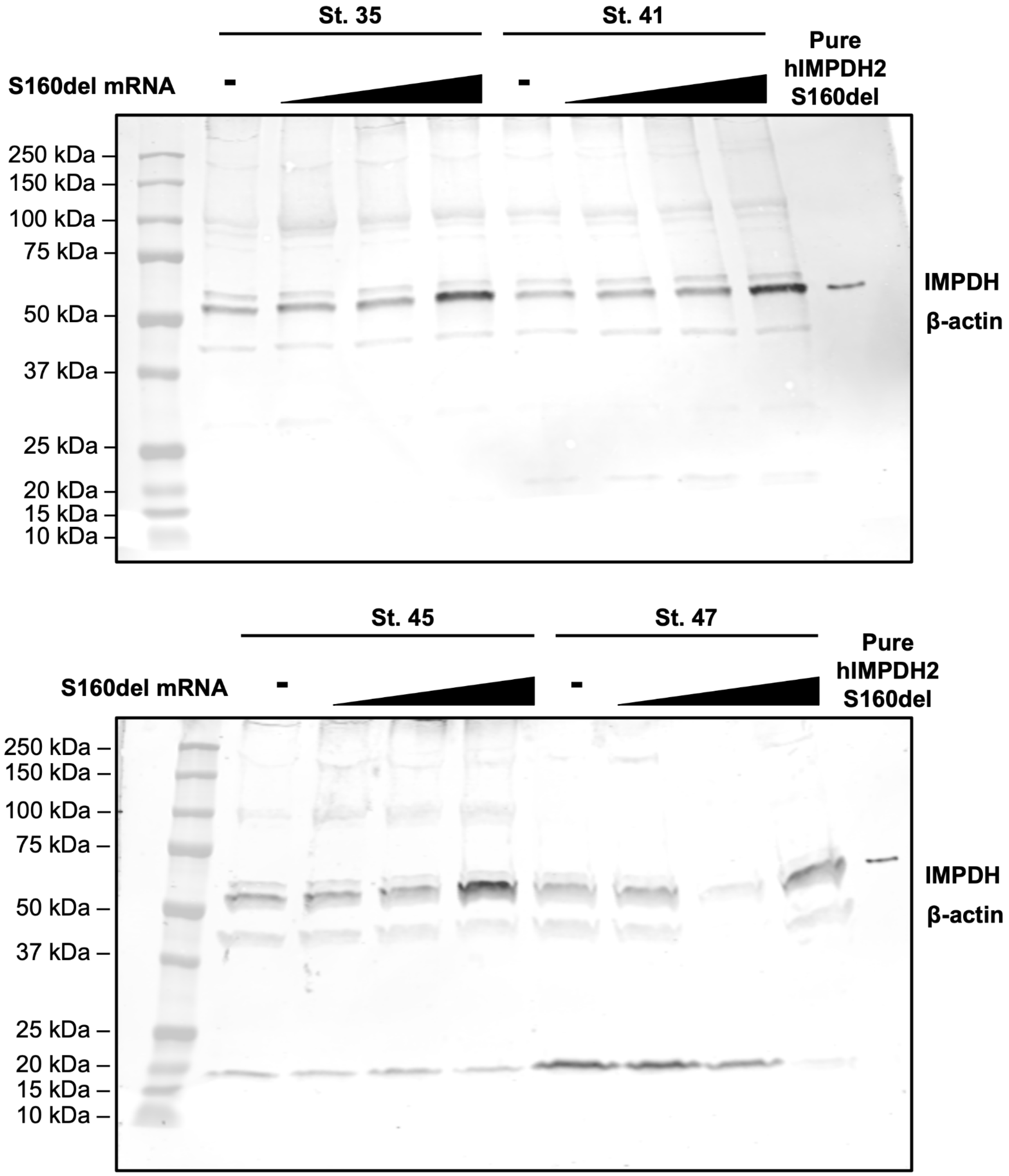

Western blot analysis of S160del hIMPDH2 expression in injected tadpoles from NF stages 35-47, or approximately 2-5 dpf. The doses of mRNA injected were 0 pg, 250 pg, 500 pg, and 1000 pg.

Figure 4.6: Volcano plots of metabolomics data.

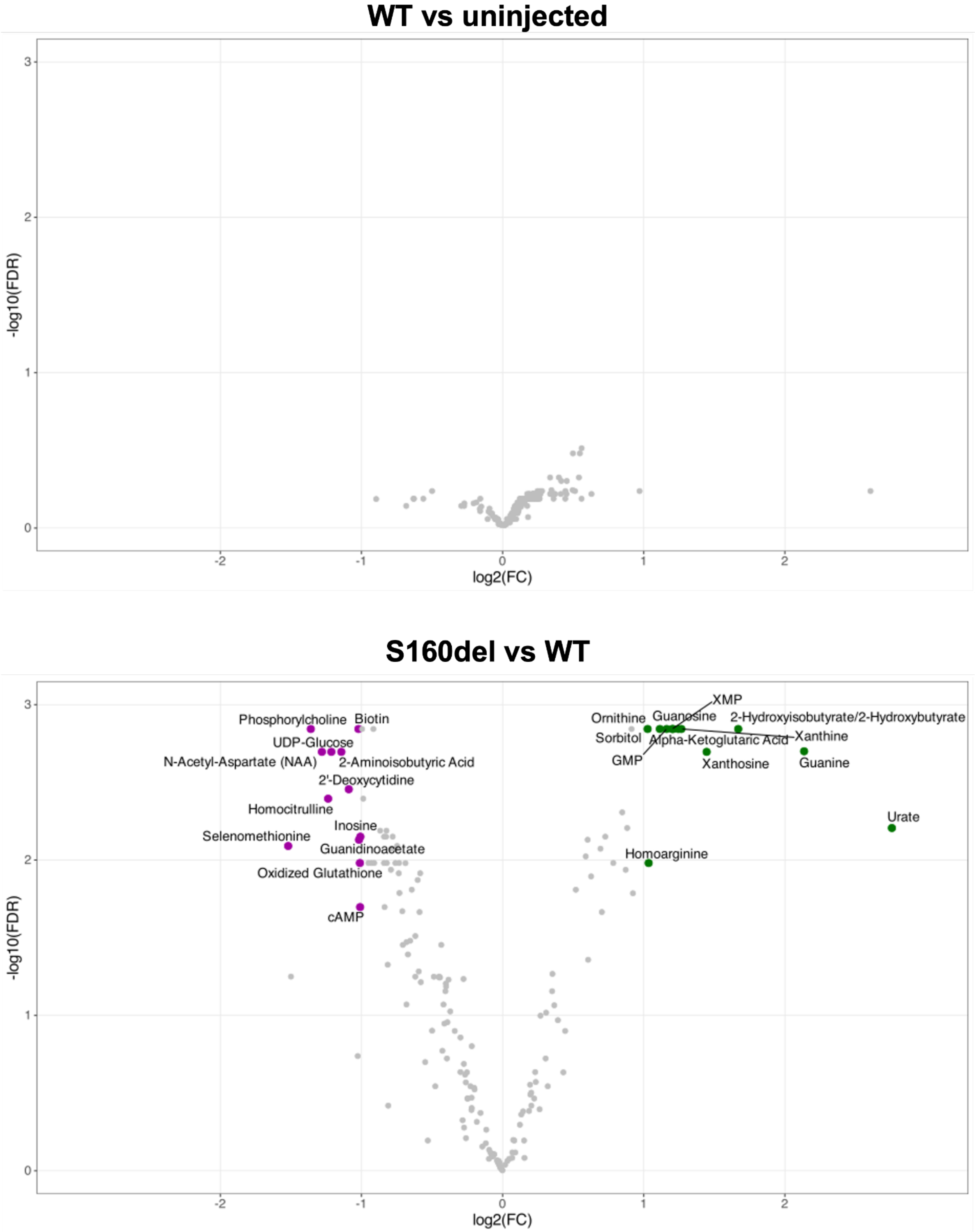

Volcano plots of metabolite levels comparing WT hIMPDH2 expressing to uninjected tadpoles (A) and comparing S160del hIMPDH2 expressing to WT hIMPDH2 expressing tadpoles (B). Labels represent metabolites with a Bonferroni false discovery rate of less than 0.05 and a fold-change of at least 2.

Figure 4.7: Principal component analysis of metabolomics dataset.

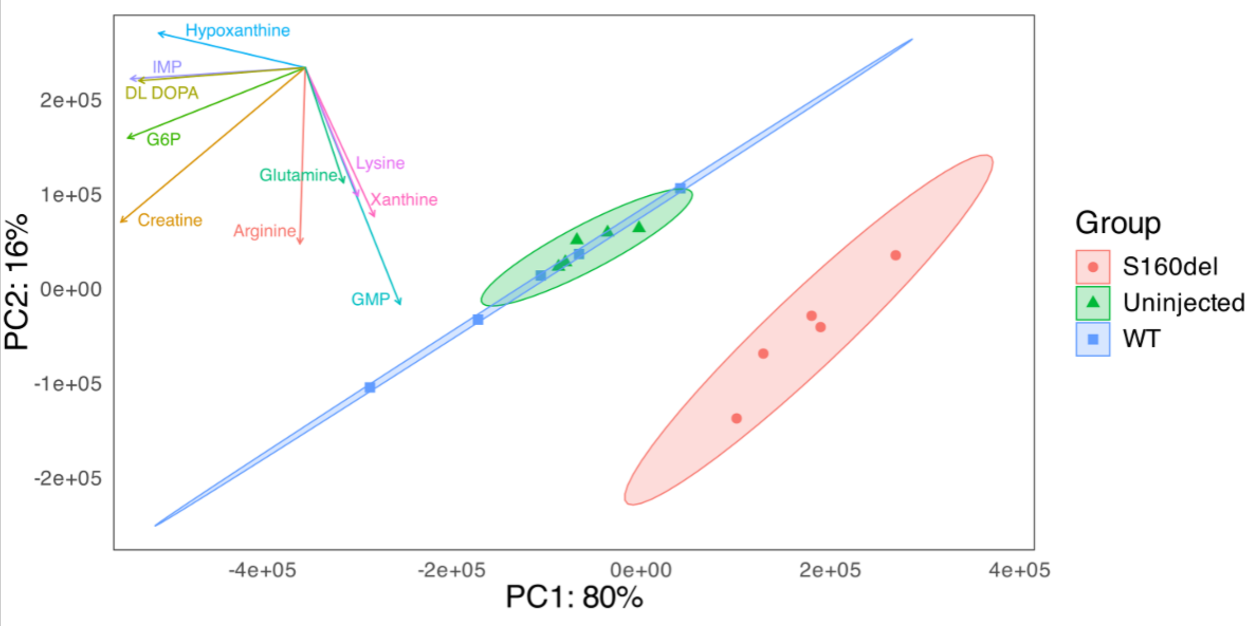

Principal component analysis of metabolomics data. Loading vectors for the 10 most weighted metabolites in PC1 are shown in the top-left corner.

Figure 4.8: Other metabolites of interest.

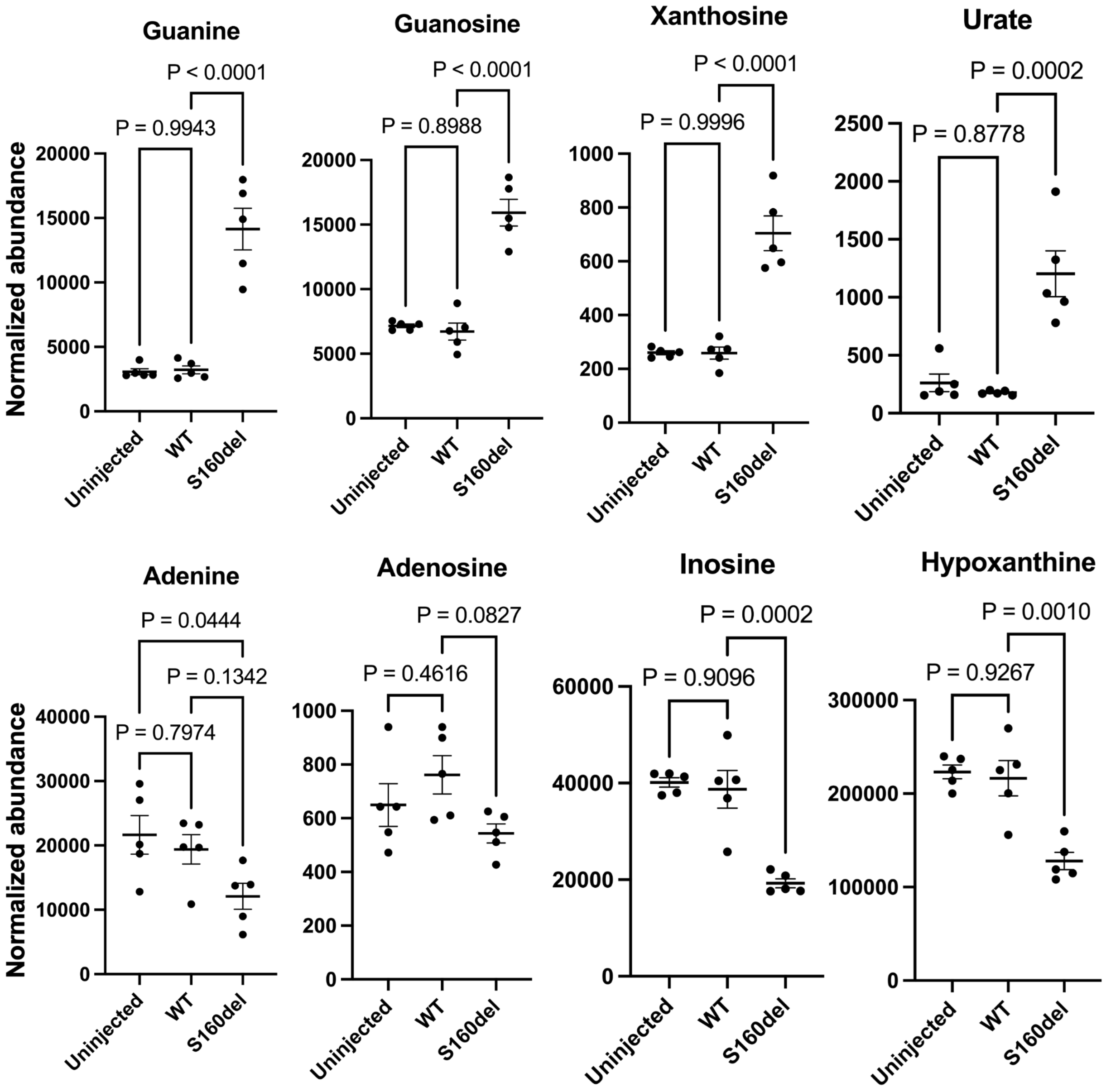

Additional plots of other metabolite levels relevant to purine synthesis and degradation. Each data point represents normalized metabolite abundance of an aggregate tissue sample composed of 10 whole tadpoles. One-way ANOVA and Tukey’s multiple comparisons test performed on metabolite levels normalized to total protein from BCA. Plotting mean +/- SEM.

Figure 4.9: Length of tadpoles at stage 41.

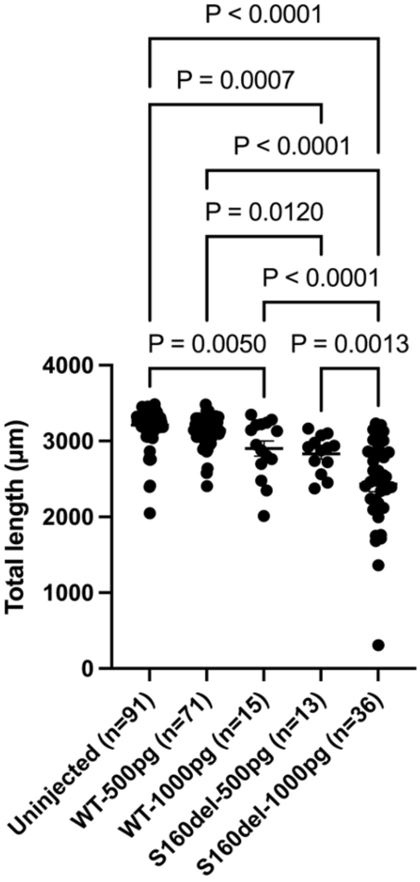

Mean length of tadpoles at stage 41, approximately 3 dpf, measured from nose to tail tip, along the spinal cord. Error bars represent the SEM.

Figure 4.10: Tadpoles expressing hIMPDH2-S160del have somitic defects.

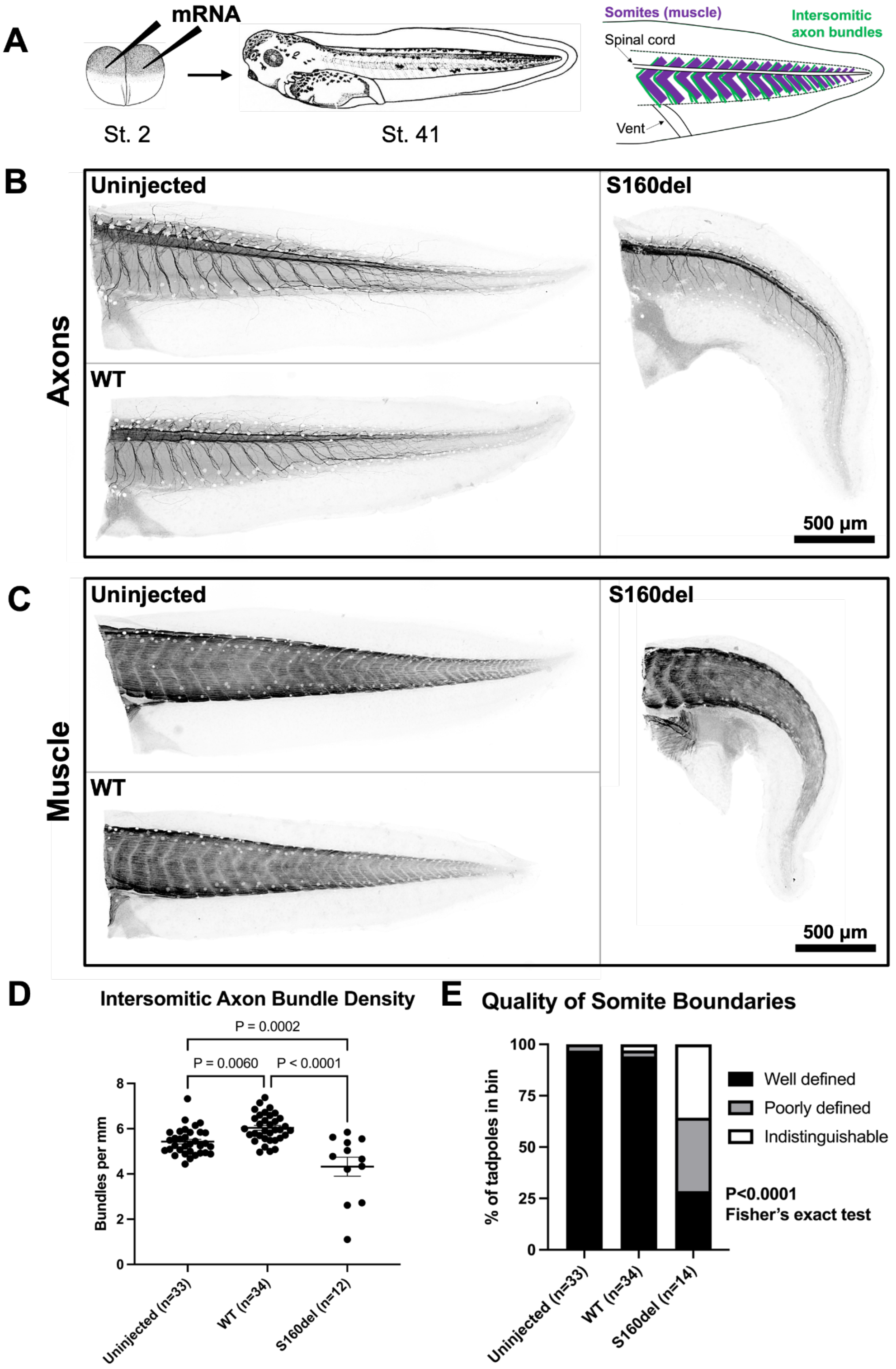

A. Diagrams of experimental design and simplified Xenopus tropicalis tail anatomy. Xenopus tropicalis embryos are injected with 500 pg of mRNA into each cell at the 2-cell stage and then raised to NF stage 41, approximately 3 dpf.

B. Representative anti-neurofilament immunofluorescence images of tadpoles injected with the indicated mRNA.

C. Representative anti-skeletal muscle immunofluorescence images of tadpoles injected with the indicated mRNA.

D. Quantification of the number of intersomitic axon bundles per mm in the tail. One-way ANOVA and Tukey’s multiple comparisons test.

E. Quantification of somite boundary quality. Fisher’s exact test for categorical variables.

Figure 4.11: S160del destabilizes IMPDH superstructures in vivo.

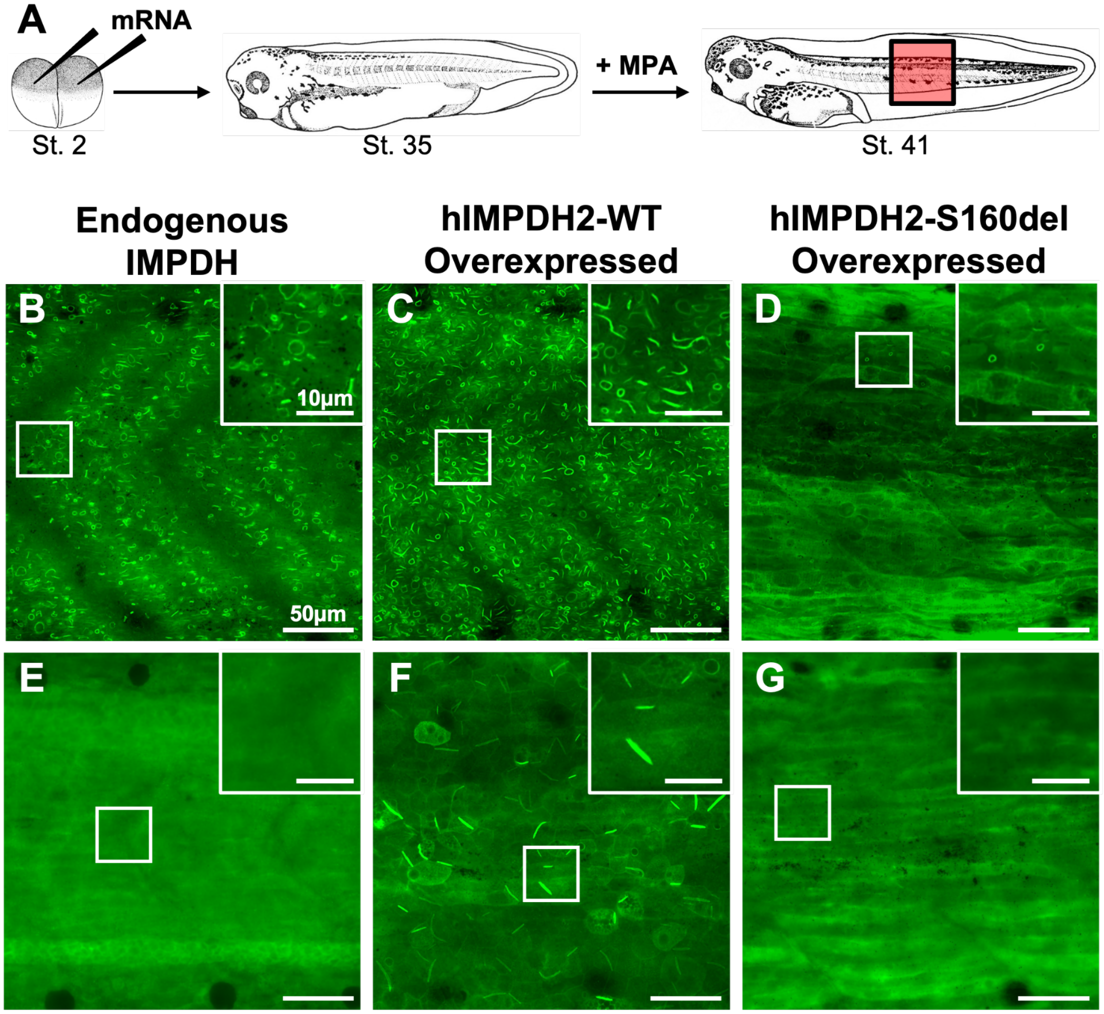

A. Experimental diagram. Xenopus tropicalis embryos are injected with 500 pg of mRNA into each cell at the 2-cell stage, raised to NF stage 35 (approximately 2 dpf), and then treated with either 1 uM MPA or vehicle control. Tadpoles are raised for an additional 24 hours to NF stage 41 and then stained for IMPDH2.

B-G. Representative anti-IMPDH2 immunofluorescence images of uninjected (endogenous) or mRNA injected tadpoles treated with either 1 uM MPA (B-D) or DMSO vehicle control (E-G). Insets in the top right corners of each image are close-ups of the regions indicated by white boxes.

Chapter 5. Concluding Remarks

In this thesis, I investigated molecular mechanisms of disease resulting from IMPDH2 mutation through the perspectives of allosteric regulation of enzyme activity, macromolecular structure, conformational equilibrium, metabolism, and vertebrate development.

This work has demonstrated the following:

1. Pathogenic mutations in IMPDH2 disrupt allosteric regulation by either increasing or decreasing the enzyme's sensitivity to GTP.
2. The allosteric regulation of both IMPDH2 filaments and free octamers is impaired by these mutations.
3. The mutations have differing effects on IMPDH2 filament structure.
4. The effect of S160 deletion on filament assembly is a separable feature from its effect on allosteric regulation.
5. S160del expression blocks IMPDH filament assembly in *Xenopus tropicalis*.
6. S160del expression in *Xenopus tropicalis* disrupts purine nucleotide metabolism and neuromuscular development.

Pathogenic mutations in IMPDH2 disrupt allosteric regulation.

Conclusions 1 and 2

IMPDH2, a filament-forming enzyme which catalyzes the first committed and rate-limiting step in guanine nucleotide biosynthesis, is allosterically regulated by downstream nucleotides GDP and GTP (Fig. 1.1). Here, we show that eleven IMPDH2 mutants desensitize the enzyme to GTP inhibition, and one mutant, R341Q, hypersensitizes the enzyme to GTP inhibition (Fig. 2.1). Making use of an engineered filament-interface disrupting mutation, Y12A, we also show that the disease mutations disrupt the GTP inhibition of IMPDH2 when not assembled into filaments (Fig. 2.5, 2.6). Because IMPDH2 filaments serve to reduce the enzyme's sensitivity to allosteric inhibition by GTP, assembly into filaments would further exacerbate the metabolic consequences of the eleven GTP-desensitized mutants, suggesting that ligands designed to disrupt the filament interface of IMPDH2 may help throttle the activity of these mutants and bring their GTP sensitivity closer to physiological nucleotide levels.

Structural biology techniques reveal different mechanisms of disruption to allosteric regulation.

Conclusions 3 and 4

Interestingly, the twelve mutants investigated here alter IMPDH2 structure in different ways–disrupting filament assembly through destabilizing either the Bateman dimer interface or filament assembly interface, constitutively forming compressed filaments, or disrupting the conformational equilibrium to disfavor compression (Fig. 2.3).

The R341Q mutant was found to abolish enzyme cooperativity (Table 2.1), increase sensitivity to GTP (Fig. 2.1), and prevent filament formation (Fig. 2.3). This mutation is predicted to break a contact at the tetramer interface, which would likely destabilize the placement of the N-terminus and disrupt filament assembly (Fig. 2.4). A high-resolution structure of this mutant is needed to support this hypothesis and will aid in drug design efforts to restore this interface.

WT IMPDH2 filaments and octamers are conformationally heterogeneous, sampling a range of states between the symmetrically extended conformation, which is catalytically active, and the symmetrically compressed conformation, which is catalytically inhibited and induced by GTP binding to the regulatory domain (Fig. 1.1). Cryo-EM analysis of one mutant, L245P, revealed that this mutation, which introduces a proline to the hinge mediating this conformational change, disrupts the equilibrium between extended and compressed states, disfavoring symmetric compression of the octamer (Fig. 2.11, 2.12). Other mutants which resemble L245P by their appearance in negative stain EM (Fig. 2.3) and sensitivity to GTP as free octamers (Fig. 2.6), such as G207R, Q245H, and K238R, may operate through similar mechanism, though higher resolution characterization of these mutants is required to support this hypothesis.

Two mutants with differing side chain charges, G113E and G113R, appeared to both form compressed filaments in the presence of ATP, observed with negative stain EM (Fig. 2.3). Since residue 113 is proximal to allosteric site 3, where GTP binds to stabilize compression, we hypothesized that these mutations may alter the environment in site 3 to allow for ATP binding to induce compression. With a high-resolution structure of the G113E mutant in the presence of ATP, we showed that this mutant was compressed without the binding of a nucleotide in this site (Fig. 2.15). A possible contact between a charged residue at position 113 and lysine 242 in the catalytic domain across the hinge may explain the stabilization of this compressed state (Fig. 2.15C). These mutants raised the question of how IMPDH2 filaments can maintain activity in a constitutively compressed state.

For the S160del mutant, we initially showed with negative stain EM that it does not form filaments in the presence of ATP or GTP (Fig. 2.3). We hypothesized that the deletion of S160 would destabilize downstream contacts across the Bateman dimer interface or affect nucleotide binding in allosteric sites 1 or 2, thus disrupting the assembly of canonical octamers and filaments (Fig. 3.1). With cryo-EM, we showed that the mutant predominantly assembles into interfacial octamers and tetramers with highly flexible Bateman domains (Fig. 2.17). However, one small class of canonical octamers was observed in this dataset, suggesting that the mutation does not completely prevent dimerization of Bateman domains (Fig. 2.17). Using dinucleoside polyphosphates Ap5G and Ap5A, which bind IMPDH with higher affinity than ATP or GTP, we demonstrated that S160del forms constitutively compressed filaments that are catalytically active and closely resemble the G113E + ATP filament structure (Fig. 3.5, 3.8, 3.13). These compressed filaments retain full activity in the presence of GTP (Fig. 3.3, 3.4). Cryo-EM analysis of actively cycling S160del filaments revealed slight filament bending that was correlated with movement of the finger domains (Fig. 3.11, 3.12). Because this heterogeneity was not observed in our dataset lacking substrates (Fig. 3.8, 3.9), we hypothesized that the observed motion is related to the catalytic cycle of the enzyme.

Further studies interrogating the role of the finger domain in the catalytic cycle of WT filaments will reveal whether this is a specific feature of the S160del mutant or generalizable to the mechanism of human IMPDH2.

***Xenopus tropicalis* is a useful model to study IMPDH2 mutation.**

Conclusions 5 and 6

To begin investigating the effects of these mutations on vertebrate development, we overexpressed one gain-of-function mutant, S160del, in the model organism *Xenopus tropicalis*, which expresses a version of IMPDH2 that is 93% identical in amino acid sequence to human IMPDH2 (Fig. 4.1). While overexpression of WT hIMPDH2 in *Xenopus tropicalis* did not result in major defects in tadpole development, overexpression of S160del hIMPDH2 resulted in clear neuromotor defects in 3-day-old tadpoles (Fig. 4.3). Immunostaining of these tadpoles revealed defects in somite structure and intersomitic axon organization at somite boundaries, suggesting defects in myogenesis and/or pathfinding of axons through the trunk tissue (Fig. 4.10). Metabolomic analysis of these tadpoles demonstrated that purine nucleotide levels were perturbed in the S160del-expressing group, leading to an overproduction of guanine nucleotides and a build-up of uric acid, a product of purine nucleotide degradation (Fig. 4.3, 4.7, 4.8). Additionally, when these tadpoles were treated with MPA and immunostained for IMPDH, S160del expression appeared to have a dominant negative effect on IMPDH filament formation, suggesting that the *in vitro* phenotypes we have described for the S160del mutant translate to this animal model (Fig. 4.11). Taken together, this work supports the use of *Xenopus tropicalis* to model neuromuscular disorders that arise from IMPDH2 mutation, and future work will shed light on the molecular mechanisms that connect IMPDH2 dysregulation to the described neuromotor defects and errors in somitogenesis.

Future directions.

While the mutations discussed here are rare, careful characterization of each emerging IMPDH2 variant will lay the foundation for developing personalized medical interventions for patients. Because not all mutations disrupt IMPDH2 filament structure or GTP inhibition in the same way, drug design efforts must take these differences into consideration. For example, while IMPDH2 inhibitors may be a useful strategy for the eleven GTP-insensitive mutants which likely retain high levels of activity in the cell, this would not be a suitable approach for the hypersensitive R341Q mutant which we predict to have low activity in the cell. For R341Q, ligands targeting the tetramer interface to stabilize the N-terminus and filament assembly may remedy its hypersensitivity to GTP and restore the enzyme’s cooperativity. Conversely, filament-disrupting approaches may be suitable for mutants like L245P, to bring GTP-sensitivity closer to physiological levels. Using the *Xenopus tropicalis* model to explore these approaches may be a useful first step towards designing therapeutics.

Our cryo-EM work investigating the effects of IMPDH2 mutations on filament structure revealed interesting changes in conformational dynamics and protein flexibility. These results generated new hypotheses that are testable *in silico* with molecular dynamics simulations or *in vitro* with methods like hydrogen deuterium exchange mass spectrometry. For example, it would be interesting to use one of these orthogonal methods to recapitulate the shift in conformational equilibrium we observed with the L245P mutant or further characterize the motion of the finger domain in the catalytic cycle of the S160del mutant.

Here, we demonstrated that S160del expression in *Xenopus tropicalis* impairs both somite structure and intersomitic axon organization. However, whether these defects are intrinsic to myogenesis or neurodevelopment remain to be determined, and the cellular mechanisms bridging purine nucleotide imbalance to these phenotypes are largely undefined. One possibility could be related to Rho family GTPase activity which is involved in a wide range of developmental processes including somitogenesis (86), angiogenesis (87), and axon guidance and branching (88). During somitogenesis, myogenic precursor cells must undergo a mesenchymal-epithelial transition which is regulated by Rac1 activity. Previous work expressing either constitutively active or dominant negative Rac1 in chick embryos showed that both increased and decreased Rac1 activity resulted in failed somitic epithelialization, suggesting that a narrow window of Rac1 activity is required for proper development of somites (89). An epithelial-mesenchymal transition and Rho GTPase activity is also involved in the development of the neural crest, a structure which depends on IMPDH2 for proper development of the craniofacial skeleton and enteric nervous system (18). In zebrafish, either treating embryos with MPA or knocking down IMPDH2 expression inhibits intersegmental blood vessel formation, suggesting that decreased IMPDH2 activity can also result in defects in angiogenesis at the somite boundaries (20). And in a study in drosophila, knocking down either IMPDH or GMP synthetase was shown to impair axon guidance (90). Interestingly, angiogenesis and axon guidance have implications on the health of muscle, as improper innervation of muscle or blood supply through the muscle leads to muscle wasting (91). Therefore, all of these processes and the interplay between them are likely affected by IMPDH2 dysregulation, possibly through aberrant Rho GTPase activity. A recent paper has indeed proposed a direct interaction between Rac1 and IMPDH2, that would serve to activate Rac1 by increasing the local concentration of GTP in the cell (92). However, a structure of the proposed complex has not yet been reported. Future work investigating Rac1 activity in our model may further clarify the link between IMPDH2 and Rho GTPases in developmental processes.

Chapter 6. Methods

Adapted from:

O’Neill, A. G., Burrell, A. L., Zech, M., Elpeleg, O., Harel, T., Edvardson, S., ... & Kollman, J. M. (2023). Neurodevelopmental disorder mutations in the purine biosynthetic enzyme IMPDH2 disrupt its allosteric regulation. Journal of Biological Chemistry, 299(8).

O’Neill, A. G., McCartney, M. E., Wheeler, G. M., Patel, J. H., Sanchez-Ramirez, G., Kollman, J. M., & Wills, A. E. (2025). An IMPDH2 variant associated with neurodevelopmental disorder disrupts purine biosynthesis and somitogenesis. bioRxiv, 2025-05.

Subcloning of IMPDH2 mutants

IMPDH2 variants were cloned into a pSMT3-Kan vector with an N-terminal 6xHis-SMT3/SUMO tag. Briefly, primers overlapping the mutation site and overlapping the Kanamycin resistance region were used for PCR amplification of vector fragments. PCR products were run on an agarose DNA gel and gel-extracted. Fragments were annealed in a Gibson assembly reaction for 1 hour at 50°C. Gibson assembly product was transformed into TOP10 cells and plated. Individual colonies were picked and cultured in LB media supplemented with Kanamycin. Plasmids were purified with the GeneJET plasmid miniprep kit, nanodropped, and sequenced with either traditional Sanger sequencing of the insert (Genewiz) or Nanopore sequencing of the whole plasmid (Plasmidsaurus).

Recombinant IMPDH expression and purification

Purified IMPDH protein was prepared as described previously (25–27). Briefly, bacterial expression plasmids were transformed into BL21 (DE3) *E. coli* and cultured in LB at 37°C to an OD600 of 0.9. Overexpression was induced with 1mM IPTG for 4 hr at 30°C. Cells were collected by centrifugation. Cell pellets were resuspended at 4°C in lysis buffer (50 mM KPO_4, 300 mM KCl, 10 mM imidazole, 800 mM urea, pH 8) with a dounce homogenizer, and the cells were lysed with an Emulsiflex-05 homogenizer. Lysate was cleared by centrifugation, and 6xHis-SMT3/SUMO tagged IMPDH2 was initially purified by Ni affinity chromatography using either a HisTrap FF column (GE Healthcare Life Sciences) on an Äkta Start chromatography system or a handpacked HisPur^{TM} Ni-NTA resin (Thermo Scientific), eluting with 50 mM KPO_4, 300 mM KCl, 500 mM imidazole, pH 8. Fractions containing IMPDH2 were treated with 1 mg ULP1 protease (93) per 100 mg IMPDH for 1 hour at 4°C to cleave the 6xHis-SMT3/SUMO tag. Following cleavage, 1 mM dithiothreitol (DTT) and 800 mM urea were added to inhibit polymerization. Protein was concentrated using a 30,000 MWCO Amicon filter and applied to a Superose 6 column pre-equilibrated in gel filtration buffer (20 mM HEPES, 100 mM KCl, 800 mM urea, 1 mM DTT, pH 8) using an Äkta Pure FPLC system. Peak fractions were concentrated using a 10,000 MWCO Amicon filter, flash-frozen in liquid nitrogen, and stored in single use aliquots at −80°C.

IMPDH activity assays

Protein aliquots were diluted in assay buffer (20 mM HEPES, 100 mM KCl, 1 mM DTT, pH 7.0) and pre-treated with varying concentrations of ATP, GTP, and IMP for 15 minutes at 25°C in 96 well UV half-area transparent plates (Corning model 3679). Reactions (100 µL total) were initiated by addition of varying concentrations of NAD+. NADH production was measured over time in increments of 1 minute for 15 minutes by absorbance at 340 nm using a Varioskan Lux microplate reader (Thermo Scientific) at 25°C. Absorbance was correlated with NADH concentration using a standard curve. Specific activity was calculated by linear interpretation of the reaction slope for a 4 minute window. All data points reported are an average of 3 measurements from the same protein preparation. Error bars are standard deviation. Fits for activity assays were calculated using the Hill-Langmuir equation $V = V_{max} * [S]^n/((K0.5)^n + [S]^n)$ and IC_{50} was calculated using a modified Hill equation $V = V_{min} * (V_{max} - V_{min})/(1 + (I/IC_{50})^{hill}$ (94).

Negatively stained electron microscopy

Samples were applied to glow-discharged continuous carbon EM grids and negatively stained with 2% uranyl formate. Grids were imaged by transmission electron microscopy using either an FEI Morgagni at 100kV acceleration voltage and a Gatan Orius CCD or a 120 kV FEI Tecnai Spirit microscope with a 4k x 4k Gatan Ultrascan CCD camera. Micrographs were collected at a nominal 22,000x magnification on the Morgagni or 42,000x magnification on the Tecnai Spirit.

Electron cryo-microscopy sample preparation and data collection

Samples were applied to glow-discharged C-flat holey carbon EM grids (Protochips), blotted, and plunge-frozen in liquid ethane using a Vitrobot plunging apparatus (FEI) at 4°C, 100% relative humidity. High-throughput data collection was performed using either an FEI Titan Krios transmission electron microscope operating at 300 kV (equipped with a Gatan image filter (GIF) and post-GIF Gatan K3 Summit direct electron detector) or a Thermo Fisher Scientific Glacios TEM operating at 200 kV and equipped with a Gatan K3 Summit direct electron detector. Data was collected using either the Leginon software package (95) or SerialEM (96).

Cryo-EM image processing

Data collection parameters are summarized in Tables 2.2, 2.3, 2.4, and 3.1. Individual workflows for processing each dataset are described in detail in Figures 2.7, 2.10, 2.14, 2.16, 3.6, 3.7, 3.9, 3.10, and 3.12.

Model building and refinement

For L245P and G113E structures, models of human IMPDH2 filaments in the extended conformation (PDB 6U8N for the octamer-centered reconstruction and PDB 6U8E for the interface-centered reconstruction) and the compressed conformation (PDB 6U9O for the octamer-centered reconstruction and PDB 6U8S for the interface-centered reconstruction) were used as templates for model building. Templates were rigid-body fit into the cryo-EM maps using UCSF Chimera, and phenix.real_space_refine was used for automated fitting employing rigid-body refinement, NCS constraints, gradient-driven minimization and simulated annealing (97). Outputs from real-space refinement in PHENIX were inspected and manually adjusted with semi-automated fitting in ISOLDE and manual fitting in Coot (98–100). This process was repeated iteratively, improving Molprobity statistics and fit to density. Refinement statistics are summarized in Supplemental Table 3. Structure figures were prepared using UCSF Chimera (101).

For all other structures: The structure of the WT hIMPDH2 free interfacial octamer was used as an initial model for the S160del interfacial octamer (PDB: 6UA5). The structure of the compressed WT hIMPDH2 free canonical octamer was used as an initial model for the S160del + Ap5G, GTP filament. Initial models were rigid-body fit into the final volume in UCSF ChimeraX v1.6.1 (102), and automated fitting was done with real space refinement in PHENIX v1.20.1-4487, with rigid-body refinement, noncrystallographic symmetry constraints, gradient-driven minimization, and simulated annealing (97, 103). The output was manually adjusted residue-by-residue in Coot v0.9.8.8 (100) and with semi-automated fitting in Isolde v1.6.0 (98). These steps were repeated iteratively to improve fit and Molprobity statistics. The final model of the interfacial octamer was used as an initial model for the tetramer, and the same model refinement process was used. Refinement statistics for the interfacial octamer and tetramer structures are reported in Table 1. Figures were prepared using UCSF Chimera (101).

X. tropicalis husbandry and use

Use of *Xenopus tropicalis* was carried out under the approval and oversight of the IACUC committee at UW, an AAALAC-accredited institution. (IACUC protocol number 4374-01) Ovulation of adult *X. tropicalis* and generation of embryos by natural matings were performed according to published methods (104, 105). Fertilized eggs were de-jellied in 3% w/v cysteine in 1/9x modified frog ringer's solution (MR) for 10–15 minutes. Embryos were reared as previously described (104). Briefly, animals were reared in petri dishes at a density of no more than 2 tadpoles/mL of 1/9x MR at a temperature of 22 °C. Clutchmates were randomly assigned to treatment groups. Staging was assessed by the Nieuwkoop and Faber (1994) staging series. Tadpoles do not begin to feed independently until approximately stage 45 and so were not fed during the course of these experiments.

Subcloning vectors for mRNA preparation

Plasmids encoding WT and S160del hIMPDH2 were subcloned from pSMT3 bacterial expression plasmids (pJK053_pSMT3_hIMPDH2 and pJK314_pSMT3_hIMPDH2-S160del) (25, 45) into the pCS2+8 vector (106) using Gibson assembly. The pCS2+8 vector was a gift from Amro Hamdoun (Addgene plasmid # 34931 ; http://n2t.net/addgene:34931 ; RRID:Addgene_34931). The IMPDH2 coding region was amplified with the following primers: hIMPDH2 template (forward - TTGTTCTTTTTGCAGGATCCATGGCCGACTACCTGATTAGTG; reverse -

ATTAATGGCGCGCCACTAGTTCAGAAAAGCCGCTTCTCATACGAATGGAG) pCS2+8 vector (forward- TGAGAAGCGGCTTTTCTGAACTAGTGGCGCGCCATTAATTAAAG; reverse-
CACTAATCAGGTAGTCGGCCATGGATCCTGCAAAAAGAACAAGTAGCTTG). PCR products were gel extracted. Insert and backbone were ligated at 50°C for 1 hour in a Gibson assembly reaction. Gibson products were transformed into chemically competent TOP10 *E. coli* cells and grown on LB agar plates containing 100 µg/ml carbenicillin. Individual colonies were picked and grown for 6 hours at 37°C in LB medium + 100 µg/ml carbenicillin. Plasmid DNA was purified using the GeneJET Plasmid Miniprep Kit (Thermo Fisher Scientific). Final construct sequence was verified with both traditional Sanger sequencing of the insert (Genewiz) and Nanopore sequencing of the whole plasmid (Plasmidsaurus) before using for *in vitro* transcription.

Preparation of mRNA

Plasmid DNA was linearized by overnight digestion with *NotI* enzyme at 37 °C (New England Biolabs). Linear DNA was purified by phenol:chloroform:isoamyl alcohol (25:24:1 v/v) extraction followed by precipitation in isopropanol with 0.05 M sodium acetate. Transcription of mRNA was performed using mMESSAGE mMACHINE SP6 Transcription Kit (Invitrogen). Template DNA was degraded by treating with DNase for 10 minutes at 37°C. The resulting mRNA product was purified by two rounds of precipitation: first in 2.5 M lithium chloride and second in ethanol with 0.14 M ammonium acetate to remove residual lithium ions. Presence of unfragmented mRNA was verified by agarose gel electrophoresis before resuspending in nuclease-free water to a stock concentration of 500 ng/µL.

Microinjections

Injection mixtures were prepared using mRNA, nuclease-free water, and fluorescent dextran fluoro-Ruby (Invitrogen) to an mRNA concentration of 250 pg/nL. Needles for injections were created from thin wall glass capillaries containing filament (World Precision Instrument) using a needle puller. Embryos were collected in batches of approximately 50 onto a petri dish coated with a thin layer of 0.1% agarose prepared in 1/9x MR to prevent dehydration. A Picospritzer III (Parker Hannifin Corporation) connected to a micromanipulator (Narishige) was used to deliver 2 nL of injection mixture into each blastomere of the 2-cell stage embryo, for a total of 1000 pg of mRNA per embryo. Injected embryos were moved into a recovery solution of 3% w/v Ficoll PM400 (Cytiva) in 1/9x MR for no more than 2 hours before transferring into 1/9x MR rearing media.

Western Blotting

Four whole embryos or tadpoles per group were homogenized on ice in 100 µL of lysis buffer (50 mM Tris pH 7.6, 150 mM NaCl, 10 mM EDTA, 0.1% Triton X-100, Roche cOmpleteTM Protease Inhibitor Cocktail). Homogenized samples were centrifuged at 18,400xg for 20 minutes at 4°C. The soluble fraction was collected, and samples were denatured by adding 1/4 volume of 4X Protein Sample Loading Buffer (Licor 928-40004). Samples were heated at 100 °C for 5 minutes. Equal inputs of the samples were run on a 4-20% Mini-PROTEAN TGX precast gel (BIO-RAD 4561094) at 180 V for

40 minutes in manufacturer recommended running buffer (25 mM Tris, 192 mM glycine, 0.1% SDS, pH 8.3). Transfer to a nitrocellulose membrane was done using an Invitrogen Power Blotter Select Transfer Stack (Thermo Fisher PB3310) on an Invitrogen Power Blotter System (Thermo Fisher PB0012) using the Mixed Range MW Pre-Programmed method (constant 2.5 A with 25 V limit for 7 minutes). Membrane was incubated in Intercept PBS Blocking Buffer (Licor 927-70001) for 1 hour at 25°C with rocking. Membrane was added into 5 mL of 1X PBS-Tween (137 mM NaCl, 2.7 mM KCl, 10 mM Na2HPO4, 1.8 mM KH2PO4, 0.1% w/v Tween-20 detergent) and 5 mL of Intercept PBS Blocking Buffer. Membrane was incubated in primary antibodies: 1:1000 rabbit anti-IMPDH2 (Proteintech 12948-1-AP) and 1:3000 mouse anti-β-actin (Santa Cruz Biotech sc-47778) overnight, shaking at 4 °C. Membrane was washed with 1X PBS-Tween for 4 x 5 minutes, then added into 5mL of 1X PBS-Tween mixed with 5mL of Intercept PBS Blocking Buffer. Membrane was incubated in the dark for 1 hour, shaking at 25 °C with secondary antibodies: 1:10000 goat anti-rabbit IgG (H+L) (DyLight 800 Fisher PISA510036) and 1:10000 goat anti-mouse IgG (H+L) (DyLight 680 Fisher PI35518). After 4 x 5 minute washes in 1X PBS-Tween, the membrane was imaged on a LI-COR Imaging System (LI-COR Biosciences).

Behavioral assays

At stage 41, tadpoles were tested for their ability to swim away from physical stimulus using a blinded escape reflex assay (76). Each tadpole was prodded once with a pipette tip at the tip of their tail, and their ability to swim away was tallied. Tadpoles that appeared to twitch without external stimulus were also tallied. Swimming and twitching were not treated as mutually exclusive behaviors.

Morphological phenotyping

At stage 41, whole tadpoles were fixed in 1x MEM with 3.7% formaldehyde at 4°C overnight. Tadpoles were imaged in 1x PBS + 0.1% Tween-20 on a bed of 1% agarose using a Leica M205 FA stereomicroscope with a color camera. Image analysis and measurements were done in Fiji.

Immunostaining

Fixed tadpoles were permeabilized by washing 3 × 20 minutes in 1x PBS + 0.01% Triton X-100 (PBS-Triton). Tadpoles were blocked for 1 hour at room temperature in 10% CAS-block (Invitrogen #00-8120) in PBS-Triton. Tadpoles were then incubated in primary antibody [1:100 rabbit anti-IMPDH2, proteintech 12948-1-AP; 1:50 mouse anti-skeletal muscle marker, DSHB 12/101; 1:50 mouse anti-neurofilament, DSHB 3A10] diluted in 100% CAS-block overnight at 4°C. Tadpoles were washed 3 × 10 minutes at room temperature in PBS-Triton then blocked for 30 minutes in 10% CAS-block in PBS-Triton. Secondary antibody [goat anti-rabbit 488, Invitrogen A11008; goat anti-mouse 594, Abcam ab150116] was diluted 1:500 in 100% CAS-block and incubated for 2 hours at room temperature. Tadpoles were then washed 3 × 10 minutes in PBS-Triton followed by a 10 minute incubation in 1:2000 DAPI (Sigma D9542) in PBS-Triton before 3 × 20 minute washes in PBS-Triton. Isolated tails were mounted on slides in ProLong Diamond (ThermoFisher P36970).

Light Microscopy

Images for Figure 1 were acquired on a Leica M205 stereo microscope with Leica DFC550 color camera using a Plan APO 1.0x objective. Images for Figures 2 and 3 were acquired on a Leica DM5500B upright microscope with motorized stage using 10x/0.30 HC PL Fluotar and 20x/0.50 HCX PL Fluotar objectives. Leica filter sets for GFP (Ex: 470/40 | Dc: 495 | Em: 525/50) and Texas Red (Ex: 560/50 | Dc: 585 | Em: 630/76) were used for immunofluorescent images. Images were collected using a 4 megapixel CCD sensor (Hamamatsu ORCA-Flash4.0 LT+) at 16-bit depth. Leica LAS X software was used for image acquisition and processing. All images were Extended Depth of Field processed from Z-stacks and fluorescent images of whole-mounted tadpole tails were created by stitching tiles from 3-4 acquisition regions.

Quantification of Immunostaining results

For neurofilament bundle quantification, the number of neurofilament bundles present posterior of the vent were counted for stage 41 tadpoles injected with 1000pg WT or S160del hIMPDH2 mRNA, as well as uninjected controls.

For somitic boundary scoring, tadpoles injected with 1000pg WT or S160del hIMPDH2 mRNA, as well as uninjected controls, were assigned a somite boundary quality score by binning tails stained for skeletal muscle into 3 categories: well defined (normal appearance of somites), poorly defined (presence of abnormally-shaped somites or some lack of boundaries), and indistinguishable (no apparent somite boundaries).

LC-MS sample preparation

For each aggregate tissue sample, 10 whole tadpoles were euthanized with a lethal dose of MS-222 at stage 41 and transferred into tubes. Media was removed, and samples were immediately flash frozen in liquid nitrogen. Five aggregate tissue samples were collected per group. Aqueous metabolites for targeted LC-MS profiling of 15 aggregate tissue samples were extracted using a protein precipitation method similar to the one previously described (107, 108) by the Northwest Metabolomics Research Center. Samples were first homogenized in 200 µL purified deionized water at 4 ˚C, and then 800 µL of cold methanol containing 124 µM 6C13-glucose and 25.9 µM 2C13-glutamate was added (reference internal standards were added to the samples in order to monitor sample prep). Afterwards samples were vortexed, stored for 30 minutes at -20 ˚C, sonicated in an ice bath for 10 minutes, centrifuged for 15 min at 14,000 rpm and 4 ˚C, and then 600 µL of supernatant was collected from each sample (left-over protein pallet was used for BCA assay). Lastly, recovered supernatants were dried on a SpeedVac and reconstituted in 0.5 mL of LC-matching solvent containing 17.8 µM 2C13-tyrosine and 39.2 3C13-lactate (reference internal standards were added to the reconstituting solvent in order to monitor LC-MS performance). Samples were transferred into LC vials and placed into a temperature controlled autosampler kept at 4 °C for LC-MS analysis.

Targeted LC-MS Assay

Targeted LC-MS metabolite analysis was performed with a similar protocol as previously described by the Northwest Metabolomics Research Center on a duplex-LC-

MS system composed of two Shimadzu UPLC pumps, CTC Analytics PAL HTC-xt temperature-controlled auto-sampler and AB Sciex 6500+ Triple Quadrupole MS equipped with ESI ionization source (107). UPLC pumps were connected to the auto-sampler in parallel and were able to perform two chromatography separations independently from each other. Each sample was injected twice on two identical analytical columns (Waters XBridge Premier BEH Amide column, Part # 186009930) performing separations in hydrophilic interaction liquid chromatography (HILIC) mode. While one column was performing separation and MS data acquisition in ESI+ ionization mode, the other column was getting equilibrated for sample injection, chromatography separation and MS data acquisition in ESI- mode. Each chromatography separation was 16 minutes (total analysis time per sample was 32 minutes). MS data acquisition was performed in multiple-reaction-monitoring (MRM) mode. LC-MS system was controlled using AB Sciex Analyst 1.6.3 software. Measured MS peaks were integrated using AB Sciex MultiQuant 3.0.3 software. The LC-MS assay was targeting 373 metabolites (plus 4 spiked reference internal standards). Up to 175 metabolites (plus 4 spiked standards) were measured across the study set, and over 95% of measured metabolites were measured across all the samples. In addition to the study samples, two sets of quality control (QC) samples were used to monitor the assay performance as well as data reproducibility. One QC [QC(I)] was a pooled human serum sample used to monitor system performance. The other QC [QC(S)] was pooled study samples, and this QC was used to monitor data reproducibility. Each QC sample was injected per every 10 study samples. The data were highly reproducible with a median CV of 3.9 %. The data were normalized using the total protein count in each sample established with a BCA assay. Analysis of normalized data was done in MetaboAnalyst 6.0 and GraphPad Prism 10.

MPA treatment of tadpoles

At two days post fertilization, tadpoles were transferred into 1/9x MR embryo rearing media supplemented with either 1 µM MPA or DMSO vehicle control and treated for 24 hours before fixation for immunostaining. Tadpoles were fixed in 1x MEM with 3.7% formaldehyde for 50 minutes at room temperature.

Statistical analysis

For behavioral assays, percentages of tadpoles that swam and percentages of tadpoles that twitched were calculated, and a 95% confidence interval of each percentage was calculated using the Wilson/Brown method. Chi-square analysis indicated significant variation among groups, and the Marasculio procedure was used to compare WT and S160del, at P=0.05. Tail curve measurements were compared using one-way ANOVA and post hoc Tukey test for multiple comparisons. For metabolomics data, one-way ANOVA and post hoc Tukey test for multiple comparisons were used to compare metabolite abundances between groups. For neurofilament bundle quantification, one-way ANOVA and post hoc Tukey test for multiple comparisons were used to compare groups. For somitic boundary scoring, Fisher’s exact test was used to determine statistical significance. Analysis and graphing were done in GraphPad Prism 10.

Data availability

Coordinates for cryo-EM structures and maps are deposited in the Protein Data Bank and Electron Microscopy Data Bank, respectively, with the following accession IDs: **9MUC** and **EMD-48628** (hIMPDH2-S160del interfacial octamer); **9MUB** and **EMD-48627** (hIMPDH2-S160del tetramer); **8FOZ** and **EMD-29357** (interface-centered extended hIMPDH2-L245P), **8G8F** and **EMD-29848** (octamer-centered extended hIMPDH2-L245P), **8FUZ** and **EMD-29482** (interface-centered compressed hIMPDH2-L245P); **8G9B** and **EMD-29863** (octamer-centered compressed hIMPDH2-L245P); **EMD-29870** (octamer-centered bent hIMPDH2-L245P).

The metabolomics dataset was deposited at metabolomicsworkbench.org under the Study ID **ST003858**.

References

1. R. C. Jackson, H. P. Morris, G. Weber, Enzymes of the Purine Ribonucleotide Cycle in Rat Hepatomas and Kidney Tumors. *Cancer Research* **37**, 3057–3065 (1977).

2. D. Mayer, *et al.*, Expression of key enzymes of purine and pyrimidine metabolism in a hepatocyte-derived cell line at different phases of the growth cycle. *J Cancer Res Clin Oncol* **116**, 251–258 (1990).

3. R. C. Jackson, G. Weber, H. P. Morris, IMP dehydrogenase, an enzyme linked with proliferation and malignancy. *Nature* **256**, 331–333 (1975).

4. Y. Natsumeda, T. Ikegami, K. Murayama, G. Weber, De Novo Guanylate Synthesis in the Commitment to Replication in Hepatoma 3924A Cells1. *Cancer Research* **48**, 507–511 (1988).

5. J. J. Gu, *et al.*, Targeted Disruption of the Inosine 5′-Monophosphate Dehydrogenase Type I Gene in Mice. *Mol Cell Biol* **23**, 6702–6712 (2003).

6. D. A. Glesne, F. R. Collart, E. Huberman, Regulation of IMP dehydrogenase gene expression by its end products, guanine nucleotides. *Mol Cell Biol* **11**, 5417–5425 (1991).

7. J. S. Dayton, T. Lindsten, C. B. Thompson, B. S. Mitchell, Effects of human T lymphocyte activation on inosine monophosphate dehydrogenase expression. *The Journal of Immunology* **152**, 984–991 (1994).

8. Y. Natsumeda, *et al.*, Two distinct cDNAs for human IMP dehydrogenase. *Journal of Biological Chemistry* **265**, 5292–5295 (1990).

9. M. Peng, *et al.*, Proteomics reveals changes in hepatic proteins during chicken embryonic development: an alternative model to study human obesity. *BMC Genomics* **19**, 29 (2018).

10. M. Senda, Y. Natsumeda, Tissue-differential expression of two distinct genes for human IMP dehydrogenase (E.C.1.1.1.205). *Life Sciences* **54**, 1917–1926 (1994).

11. S. Kofuji, A. T. Sasaki, GTP metabolic reprogramming by IMPDH2: unlocking cancer cells' fuelling mechanism. *The Journal of Biochemistry* **168**, 319–328 (2020).

12. L. Hedstrom, IMP Dehydrogenase: Structure, Mechanism, and Inhibition. *Chem. Rev.* **109**, 2903–2928 (2009).

13. J. H. Gunter, *et al.*, Characterisation of inosine monophosphate dehydrogenase expression during retinal development: Differences between variants and

isoforms. *The International Journal of Biochemistry & Cell Biology* **40**, 1716–1728 (2008).

14. Y. Konno, *et al.*, Expression of human IMP dehydrogenase types I and II in Escherichia coli and distribution in human normal lymphocytes and leukemic cell lines. *Journal of Biological Chemistry* **266**, 506–509 (1991).

15. M. Nagai, *et al.*, Selective Up-Regulation of Type II Inosine 5′-Monophosphate Dehydrogenase Messenger RNA Expression in Human Leukemias1. *Cancer Research* **51**, 3886–3890 (1991).

16. F. R. Collart, C. B. Chubb, B. L. Mirkin, E. Huberman, “Increased IMP dehydrogenase gene expression in solid tumor tissues and tumor cell lines” (1992).

17. J. J. Gu, *et al.*, Inhibition of T lymphocyte activation in mice heterozygous for loss of the IMPDH II gene. *J. Clin. Invest.* **106**, 599–606 (2000).

18. J. I. Lake, M. Avetisyan, A. G. Zimmermann, R. O. Heuckeroth, Neural crest requires Impdh 2 for development of the enteric nervous system, great vessels, and craniofacial skeleton. *Developmental Biology* **409**, 152–165 (2016).

19. T. Mizukoshi, S. Yamada, S. Sakakibara, Spatiotemporal Regulation of *De Novo* and Salvage Purine Synthesis during Brain Development. *eNeuro* **10**, ENEURO.0159-23.2023 (2023).

20. X. Wu, *et al.*, Mycophenolic Acid Is a Potent Inhibitor of Angiogenesis. *ATVB* **26**, 2414–2416 (2006).

21. R. M. Buey, *et al.*, Guanine nucleotide binding to the Bateman domain mediates the allosteric inhibition of eukaryotic IMP dehydrogenases. *Nat Commun* **6**, 8923 (2015).

22. J. W. Scott, *et al.*, CBS domains form energy-sensing modules whose binding of adenosine ligands is disrupted by disease mutations. *J. Clin. Invest.* **113**, 274–284 (2004).

23. G. Labesse, *et al.*, MgATP Regulates Allostery and Fiber Formation in IMPDHs. *Structure* **21**, 975–985 (2013).

24. R. M. Buey, *et al.*, A nucleotide-controlled conformational switch modulates the activity of eukaryotic IMP dehydrogenases. *Sci Rep* **7**, 2648 (2017).

25. S. A. Anthony, *et al.*, Reconstituted IMPDH polymers accommodate both catalytically active and inactive conformations. *MBoC* **28**, 2600–2608 (2017).

26. M. C. Johnson, J. M. Kollman, Cryo-EM structures demonstrate human IMPDH2 filament assembly tunes allosteric regulation. *eLife* **9**, e53243 (2020).

27. A. L. Burrell, *et al.*, IMPDH1 retinal variants control filament architecture to tune allosteric regulation. *Nat Struct Mol Biol* **29**, 47–58 (2022).

28. R. M. Buey, D. Fernández-Justel, A. Jiménez, J. L. Revuelta, The gateway to guanine nucleotides: Allosteric regulation of IMP dehydrogenases. *Protein Science* **31** (2022).

29. O. Bulvas, *et al.*, Deciphering the allosteric regulation of mycobacterial inosine-5′-monophosphate dehydrogenase. *Nat Commun* **15**, 6673 (2024).

30. D. Fernández-Justel, *et al.*, A Nucleotide-Dependent Conformational Switch Controls the Polymerization of Human IMP Dehydrogenases to Modulate their Catalytic Activity. *Journal of Molecular Biology* **431**, 956–969 (2019).

31. E. M. Lynch, J. M. Kollman, B. A. Webb, Filament formation by metabolic enzymes—A new twist on regulation. *Current Opinion in Cell Biology* **66**, 28–33 (2020).

32. J. Peterson, N. Akizu, J. Simonet, M. Foster, A. O'Reilly, Enzyme polymerization in nucleotide biosynthesis. *The FASEB Journal* **34**, 1–1 (2020).

33. J. C. Simonet, A. L. Burrell, J. M. Kollman, J. R. Peterson, Freedom of assembly: metabolic enzymes come together. *MBoC* **31**, 1201–1205 (2020).

34. K. L. Hvorecny, J. M. Kollman, Greater than the sum of parts: Mechanisms of metabolic regulation by enzyme filaments. *Current Opinion in Structural Biology* **79**, 102530 (2023).

35. K. L. Hvorecny, K. Hargett, J. D. Quispe, J. M. Kollman, Human PRPS1 filaments stabilize allosteric sites to regulate activity. *Nat Struct Mol Biol* **30**, 391–402 (2023).

36. Y. Ji, J. Gu, A. M. Makhov, J. D. Griffith, B. S. Mitchell, Regulation of the Interaction of Inosine Monophosphate Dehydrogenase with Mycophenolic Acid by GTP. *Journal of Biological Chemistry* **281**, 206–212 (2006).

37. E. C. Thomas, *et al.*, Different Characteristics and Nucleotide Binding Properties of Inosine Monophosphate Dehydrogenase (IMPDH) Isoforms. *PLoS ONE* **7**, e51096 (2012).

38. W. C. Carcamo, S. J. Calise, C. A. von Mühlen, M. Satoh, E. K. L. Chan, "Molecular Cell Biology and Immunobiology of Mammalian Rod/Ring Structures" in *International Review of Cell and Molecular Biology*, (Elsevier, 2014), pp. 35–74.

39. S. J. Calise, *et al.*, Glutamine deprivation initiates reversible assembly of mammalian rods and rings. *Cell. Mol. Life Sci.* **71**, 2963–2973 (2014).

40. K. C. Duong-Ly, *et al.*, T cell activation triggers reversible inosine-5′-monophosphate dehydrogenase assembly. *Journal of Cell Science* jcs.223289 (2018). https://doi.org/10.1242/jcs.223289.

41. N. Ahangari, *et al.*, Nuclear IMPDH Filaments in Human Gliomas. *Journal of Neuropathology & Experimental Neurology* **80**, 944–954 (2021).

42. S. Toyoda, T. Handa, H. Yong, H. Takahashi, H. Shiwaku, IMPDH2 forms spots at branching sites and distal ends of astrocyte stem processes. *Genes to Cells* **29**, 150–158 (2024).

43. P. Juda, J. Šmigová, L. Kováčik, E. Bártová, I. Raška, Ultrastructure of Cytoplasmic and Nuclear Inosine-5'-Monophosphate Dehydrogenase 2 “Rods and Rings” Inclusions. *J Histochem Cytochem.* **62**, 739–750 (2014).

44. M. Zech, *et al.*, Monogenic variants in dystonia: an exome-wide sequencing study. *The Lancet Neurology* **19**, 908–918 (2020).

45. A. G. O’Neill, *et al.*, Neurodevelopmental disorder mutations in the purine biosynthetic enzyme IMPDH2 disrupt its allosteric regulation. *Journal of Biological Chemistry* **299**, 105012 (2023).

46. S. J. Bowne, Mutations in the inosine monophosphate dehydrogenase 1 gene (IMPDH1) cause the RP10 form of autosomal dominant retinitis pigmentosa. *Human Molecular Genetics* **11**, 559–568 (2002).

47. A. Kennan, Identification of an IMPDH1 mutation in autosomal dominant retinitis pigmentosa (RP10) revealed following comparative microarray analysis of transcripts derived from retinas of wild-type and Rho-/- mice. *Human Molecular Genetics* **11**, 547–558 (2002).

48. Y. Wada, *et al.*, Screen of the *IMPDH1* Gene among Patients with Dominant Retinitis Pigmentosa and Clinical Features Associated with the Most Common Mutation, Asp226Asn. *Invest. Ophthalmol. Vis. Sci.* **46**, 1735 (2005).

49. S. Grover, G. A. Fishman, E. M. Stone, A novel IMPDH1 mutation (Arg231Pro) in a family with a severe form of autosomal dominant retinitis pigmentosa. *Ophthalmology* **111**, 1910–1916 (2004).

50. S. J. Bowne, *et al.*, Spectrum and Frequency of Mutations in IMPDH1 Associated with Autosomal Dominant Retinitis Pigmentosa and Leber Congenital Amaurosis. *Invest. Ophthalmol. Vis. Sci.* **47**, 34 (2006).

51. J. Lin, *et al.*, Rare variants in IMPDH2 cause autosomal dominant dystonia in Chinese population. *J Neurol* (2023). https://doi.org/10.1007/s00415-023-11564-x.

52. A. Kuukasjärvi, *et al.*, IMPDH2: a new gene associated with dominant juvenile-onset dystonia-tremor disorder. *Eur J Hum Genet* **29**, 1833–1837 (2021).

53. S. I. Deutsch, K. D. Long, R. B. Rosse, J. Mastropaolo, J. Eller, Hypothesized Deficiency of Guanine-Based Purines May Contribute to Abnormalities of Neurodevelopment, Neuromodulation, and Neurotransmission in Lesch-Nyhan Syndrome. *Clinical Neuropharmacology* **28**, 28–37 (2005).

54. F. M. Rosenbloom, Inherited Disorder of Purine Metabolism: Correlation Between Central Nervous System Dysfunction and Biochemical Defects. *JAMA* **202**, 175 (1967).

55. J. E. Seegmiller, F. M. Rosenbloom, W. N. Kelley, Enzyme Defect Associated with a Sex-Linked Human Neurological Disorder and Excessive Purine Synthesis. *Science* **155**, 1682–1684 (1967).

56. M. Lesch, W. L. Nyhan, A familial disorder of uric acid metabolism and central nervous system function. *The American Journal of Medicine* **36**, 561–570 (1964).

57. F. M. Rosenbloom, J. F. Henderson, I. C. Caldwell, W. N. Kelley, J. E. Seegmiller, Biochemical Bases of Accelerated Purine Biosynthesis de Novo in Human Fibroblasts Lacking Hypoxanthine-Guanine Phosphoribosyltransferase. *Journal of Biological Chemistry* **243**, 1166–1173 (1968).

58. A. W. Wood, M. A. Becker, J. D. Minna, J. E. Seegmiller, Purine Metabolism in Normal and Thioguanine-Resistant Neuroblastoma. *Proc. Natl. Acad. Sci. U.S.A.* **70**, 3880–3883 (1973).

59. T. W. Traut, Physiological concentrations of purines and pyrimidines. *Mol Cell Biochem* **140**, 1–22 (1994).

60. M. D. Sintchak, *et al.*, Structure and Mechanism of Inosine Monophosphate Dehydrogenase in Complex with the Immunosuppressant Mycophenolic Acid. *Cell* **85**, 921–930 (1996).

61. T. J. Franklin, J. M. Cook, The inhibition of nucleic acid synthesis by mycophenolic acid. *Biochemical Journal* **113**, 515–524 (1969).

62. L.-X. Liao, *et al.*, Highly selective inhibition of IMPDH2 provides the basis of antineuroinflammation therapy. *Proc. Natl. Acad. Sci. U.S.A.* **114** (2017).

63. M. W. Country, Retinal metabolism: A comparative look at energetics in the retina. *Brain Research* **1672**, 50–57 (2017).

64. M. Wong-Riley, Energy metabolism of the visual system. *EB* 99 (2010). https://doi.org/10.2147/EB.S9078.

65. V. Y. Arshavsky, M. E. Burns, Photoreceptor Signaling: Supporting Vision across a Wide Range of Light Intensities. *Journal of Biological Chemistry* **287**, 1620–1626 (2012).

66. D.-G. Luo, T. Xue, K.-W. Yau, How vision begins: An odyssey. *Proc. Natl. Acad. Sci. U.S.A.* **105**, 9855–9862 (2008).

67. K. Palczewski, Chemistry and Biology of the Initial Steps in Vision: The Friedenwald Lecture. *Invest. Ophthalmol. Vis. Sci.* **55**, 6651 (2014).

68. A. K. Sharma, B. Rohrer, Sustained Elevation of Intracellular cGMP Causes Oxidative Stress Triggering Calpain-Mediated Apoptosis in Photoreceptor Degeneration. *Current Eye Research* **32**, 259–269 (2007).

69. J. Du, J. An, J. D. Linton, Y. Wang, J. B. Hurley, "How Excessive cGMP Impacts Metabolic Proteins in Retinas at the Onset of Degeneration" in *Retinal Degenerative Diseases*, Advances in Experimental Medicine and Biology., J. D. Ash, *et al.*, Eds. (Springer International Publishing, 2018), pp. 289–295.

70. J. Charish, "cAMP and Photoreceptor Cell Death in Retinal Degeneration" in *Retinal Degenerative Diseases*, Advances in Experimental Medicine and Biology., C. Bowes Rickman, *et al.*, Eds. (Springer International Publishing, 2019), pp. 301–304.

71. A. C. Allison, E. M. Eugui, Immunosuppressive and other Effects of Mycophenolic Acid and an Ester Prodrug, Mycophenolate Mofetil. *Immunol Rev* **136**, 5–28 (1993).

72. L. M. Shaw, *et al.*, Mycophenolate Mofetil: A Report of the Consensus Panel: *Therapeutic Drug Monitoring* **17**, 690–699 (1995).

73. W. Wang, *et al.*, Shikonin is a novel and selective IMPDH2 inhibitor that target triple-negative breast cancer. *Phytotherapy Research* **35**, 463–476 (2021).

74. D. Fernández-Justel, R. Peláez, J. L. Revuelta, R. M. Buey, The Bateman domain of IMP dehydrogenase is a binding target for dinucleoside polyphosphates. *Journal of Biological Chemistry* **294**, 14768–14775 (2019).

75. M. Duperray, *et al.*, Purine Biosynthesis Pathways Are Required for Myogenesis in Xenopus laevis. *Cells* **12**, 2379 (2023).

76. M. Breuer, H. Berger, A. Borchers, Caveolin 1 is required for axonal outgrowth of motor neurons and affects Xenopus neuromuscular development. *Sci Rep* **10**, 16446 (2020).

77. K. G. Sullivan, M. Levin, Neurotransmitter signaling pathways required for normal development in *Xenopus laevis* embryos: a pharmacological survey screen. *J. Anat.* **229**, 483–502 (2016).

78. M. E. McCartney, *et al.*, Appendage regeneration requires IMPDH2 and creates a sensitized environment for enzyme filament formation. [Preprint] (2024). Available

at: http://biorxiv.org/lookup/doi/10.1101/2024.07.29.605679 [Accessed 5 May 2025].

79. G. D. Keppeke, *et al.*, IMP/GTP balance modulates cytoophidium assembly and IMPDH activity. *Cell Div* **13**, 5 (2018).

80. G. D. Keppeke, C.-C. Chang, Z. Zhang, J.-L. Liu, Effect on cell survival and cytoophidium assembly of the adRP-10-related IMPDH1 missense mutation Asp226Asn. *Front. Cell Dev. Biol.* **11**, 1234592 (2023).

81. U. Sorrentino, A. G. O'Neill, J. M. Kollman, H. A. Jinnah, M. Zech, Purine Metabolism and Dystonia: Perspectives of a Long-Promised Relationship. *Annals of Neurology* **97**, 809–825 (2025).

82. M.-C. Nassogne, S. Marie, J. P. Dewulf, Neurological presentations of inborn errors of purine and pyrimidine metabolism. *European Journal of Paediatric Neurology* **48**, 69–77 (2024).

83. J. Maiuolo, F. Oppedisano, S. Gratteri, C. Muscoli, V. Mollace, Regulation of uric acid metabolism and excretion. *International Journal of Cardiology* **213**, 8–14 (2016).

84. W. L. Nyhan, Clinical Features of the Lesch-Nyhan Syndrome. *Arch Intern Med* **130**, 186 (1972).

85. R. J. Torres, J. G. Puig, H. A. Jinnah, Update on the phenotypic spectrum of Lesch-Nyhan disease and its attenuated variants. *Curr Rheumatol Rep* **14**, 189–194 (2012).

86. C. Kalcheim, Epithelial–Mesenchymal Transitions during Neural Crest and Somite Development. *JCM* **5**, 1 (2015).

87. B. A. Bryan, P. A. D'Amore, What tangled webs they weave: Rho-GTPase control of angiogenesis. *Cell. Mol. Life Sci.* **64**, 2053–2065 (2007).

88. J. Ng, *et al.*, Rac GTPases control axon growth, guidance and branching. *Nature* **416**, 442–447 (2002).

89. Y. Nakaya, S. Kuroda, Y. T. Katagiri, K. Kaibuchi, Y. Takahashi, Mesenchymal-Epithelial Transition during Somitic Segmentation Is Regulated by Differential Roles of Cdc42 and Rac1. *Developmental Cell* **7**, 425–438 (2004).

90. H. Long, S. Cameron, L. Yu, Y. Rao, *De Novo* GMP Synthesis Is Required for Axon Guidance in Drosophila. *Genetics* **172**, 1633–1642 (2006).

91. E. P. De Lima, *et al.*, Vascular Impairment, Muscle Atrophy, and Cognitive Decline: Critical Age-Related Conditions. *Biomedicines* **12**, 2096 (2024).

92. A. Bianchi-Smiraglia, *et al.*, Regulation of local GTP availability controls RAC1 activity and cell invasion. *Nat Commun* **12**, 6091 (2021).

93. E. Mossessova, C. D. Lima, Ulp1-SUMO Crystal Structure and Genetic Analysis Reveal Conserved Interactions and a Regulatory Element Essential for Cell Growth in Yeast. *Molecular Cell* **5**, 865–876 (2000).

94. D. A. Volpe, S. S. Hamed, L. K. Zhang, Use of Different Parameters and Equations for Calculation of IC50 Values in Efflux Assays: Potential Sources of Variability in IC50 Determination. *AAPS J* **16**, 172–180 (2014).

95. B. Carragher, *et al.*, Leginon: An Automated System for Acquisition of Images from Vitreous Ice Specimens. *Journal of Structural Biology* **132**, 33–45 (2000).

96. D. N. Mastronarde, Automated electron microscope tomography using robust prediction of specimen movements. *Journal of Structural Biology* **152**, 36–51 (2005).

97. P. V. Afonine, *et al.*, Real-space refinement in *PHENIX* for cryo-EM and crystallography. *Acta Crystallogr D Struct Biol* **74**, 531–544 (2018).

98. T. I. Croll, *ISOLDE* : a physically realistic environment for model building into low-resolution electron-density maps. *Acta Crystallogr D Struct Biol* **74**, 519–530 (2018).

99. P. Emsley, K. Cowtan, *Coot* : model-building tools for molecular graphics. *Acta Crystallogr D Biol Crystallogr* **60**, 2126–2132 (2004).

100. P. Emsley, B. Lohkamp, W. G. Scott, K. Cowtan, Features and development of *Coot*. *Acta Crystallogr D Biol Crystallogr* **66**, 486–501 (2010).

101. E. F. Pettersen, *et al.*, UCSF Chimera?A visualization system for exploratory research and analysis. *J. Comput. Chem.* **25**, 1605–1612 (2004).

102. T. D. Goddard, *et al.*, UCSF ChimeraX: Meeting modern challenges in visualization and analysis. *Protein Science* **27**, 14–25 (2018).

103. D. Liebschner, *et al.*, Macromolecular structure determination using X-rays, neutrons and electrons: recent developments in *Phenix*. *Acta Crystallogr D Struct Biol* **75**, 861–877 (2019).

104. M. K. Khokha, *et al.*, Techniques and probes for the study of *Xenopus tropicalis* development. *Developmental Dynamics* **225**, 499–510 (2002).

105. H. L. Sive, R. M. Grainger, R. M. Harland, Isolation of *Xenopus* Oocytes. *Cold Spring Harb Protoc* **2010**, pdb.prot5534 (2010).

106. T. Gökirmak, *et al.*, Localization and Substrate Selectivity of Sea Urchin Multidrug (MDR) Efflux Transporters. *Journal of Biological Chemistry* **287**, 43876–43883 (2012).

107. J. H. Patel, D. J. Ong, C. R. Williams, L. K. Callies, A. E. Wills, Elevated pentose phosphate pathway flux supports appendage regeneration. *Cell Reports* **41**, 111552 (2022).

108. K. Kurup, *et al.*, Calorie restriction prevents age-related changes in the intestinal microbiota. *Aging* **13**, 6298–6329 (2021).